Hazards at the production of titanium alloys in the electric arc furnace

Slokar Benić, Ljerka; Ivec, Ivan; Čačić, Katarina

Source / Izvornik: **Proceedings of the XXVII International Scientific and Technical Conference Foundry 2023, 2023, 5 - 8**

Conference paper / Rad u zborniku

Publication status / Verzija rada: **Published version / Objavljena verzija rada (izdavačev PDF)**

Permanent link / Trajna poveznica: https://urn.nsk.hr/urn:nbn:hr:115:658734

XX JUBILEE INTERNATIONAL SCIENTIFIC CONGRESS

WINTER SESSION

08 - 11.03.2023, BOROVETS, BULGARIA

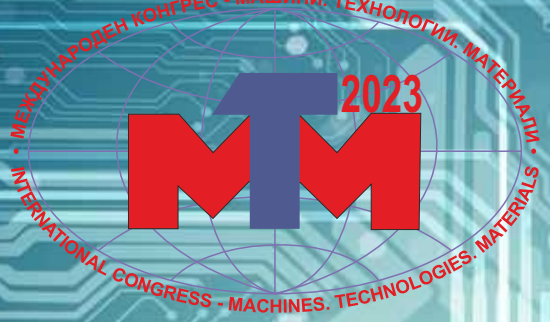

MACHINES. TECHNOLOGIES. MATERIALS 2023

PROCEEDINGS

VOLUME I
MACHINES
MATERIALS

ISSN 2535-0021 (PRINT)
ISSN 2535-003X (ONLINE)

SCIENTIFIC-TECHNICAL UNION OF MECHANICAL ENGINEERING - INDUSTRY 4.0
BULGARIA

XX JUBILEE INTERNATIONAL CONGRESS
WINTER SESSION
"MACHINES.TECHNOLOGIES.MATERIALS"
08–11.03.2023 BOROVETS, BULGARIA

PROCEEDINGS

YEAR VI, ISSUE 1 (25), BOROVETS, BULGARIA 2023

VOLUME I
MACHINES. MATERIALS.

ISSN 2535-0021 (PRINT)
ISSN 2535-003X (ONLINE)

PUBLISHER:

SCIENTIFIC TECHNICAL UNION OF MECHANICAL ENGINEERING INDUSTRY-4.0

108, Rakovski Str., 1000 Sofia, Bulgaria
tel. (+359 2) 987 72 90,
tel./fax (+359 2) 986 22 40**,**
office@mtmcongress.com
www.mtmcongress.com

INTERNATIONAL EDITORIAL BOARD

C O N T E N T S

MACHINES

MATERIALS

The influence of steam extractions operation dynamics on the turbine efficiencies and losses

Mrzljak Vedran[1], Prpić-Oršić Jasna[1], Glučina Matko[2], Poljak Igor[3]
[1]Faculty of Engineering, University of Rijeka, Vukovarska 58, 51000 Rijeka, Croatia
[2]University of Rijeka, Trg braće Mažuranića 10, 51000 Rijeka, Croatia
[3]Department of maritime sciences, University of Zadar, Mihovila Pavlinovića 1, 23000 Zadar, Croatia
E-mail: vedran.mrzljak@riteh.hr, jasna.prpic-orsic@riteh.hr, matko.glucina@uniri.hr, ipoljak1@unizd.hr

Abstract: *In this paper are presented results of a low-pressure steam turbine energy and exergy analysis during turbine extractions opening/closing. All possible combinations of extractions opening/closing are observed. The highest mechanical power which can be produced by this turbine (when all steam extractions are closed) is 28017.48 kW in real and 31988.20 kW in an ideal situation. For all observed steam extractions opening/closing combinations is obtained that energy efficiency and energy losses range is relatively small (from 87.56% to 87.94% for energy efficiency and from 3360.46 kW to 3970.72 kW for energy losses). Trends in energy and exergy losses (destructions) are identical for all observed extractions opening/closing combinations. Analyzed turbine efficiencies (both energy and exergy) will decrease for a maximum 1% during the steam extractions closing. Turbine steam extractions closing decrease turbine efficiencies and increases turbine losses (destructions), what is valid from both energy and exergy aspects.*

KEYWORDS: STEAM TURBINE, STEAM EXTRACTIONS, OPERATION DYNAMICS, EFFICIENCY, LOSSES

1. Introduction

A variety of steam turbines can be found in the power plants worldwide. Main steam turbines are usually complex steam turbines which consist of several cylinders connected to the same shaft [1, 2]. Auxiliary steam turbines are usually used for the additional mechanical power producing or for a direct drive of various mechanical power consumers [3, 4].

It should be highlighted that nowadays, steam turbine is not the mechanical power producer only, it is also a machine for steam delivery (heat energy delivery) to various heaters inside the power plant [5, 6]. Steam delivery to the heaters is performed through steam turbine extractions. Complex multi-cylinder steam turbines usually have few steam extractions from each cylinder [7, 8], while auxiliary steam turbines usually did not have any steam extraction [9]. Therefore, steam extractions are essential part of recent steam turbines and they can notably influence steam turbine performance.

Steam turbine performance during various extractions operation dynamics can be investigated by using several possible techniques – two of such techniques are energy and exergy analyses [10, 11], which are applied in this paper.

In this paper is performed analysis of low-pressure steam turbine developed power, energy and exergy efficiencies as well as losses for each possible steam extractions opening/closing combination. Steam extractions closing will surely increase turbine developed power, but it is interesting to observe what will happen with turbine efficiencies and losses in such operating regimes.

2. Description of the analyzed steam turbine

Scheme of the analyzed low-pressure steam turbine along with operating points required for the analyses, is presented in Fig. 1.

Low-pressure turbine analyzed in this paper is the last cylinder of a complex, two cylinder steam turbine. Both cylinders (high-pressure and low-pressure cylinder) are connected to the same shaft which drives an electric generator. Between mentioned cylinders is mounted re-heater. Details related to the whole described turbine and power plant in which it operates can be found in [12].

Steam re-heater delivers superheated steam to the analyzed low-pressure turbine. The turbine has four steam extractions (operating points 2, 3, 4 and 5) which are used for steam delivery to the components of low-pressure feed water heating system (deaerator and low-pressure feed water heaters) [13]. The remaining steam mass flow rate, which expand through all the stages of the observed turbine, is finally delivered to steam condenser for condensation [14].

The observed steam turbine is analyzed as an independent component (the influences of steam extractions opening/closing on other power plant components or on the entire steam power plant are not considered). Due to simplicity, it is considered that each steam turbine extraction can be fully opened or fully closed (partially opened extractions are not observed).

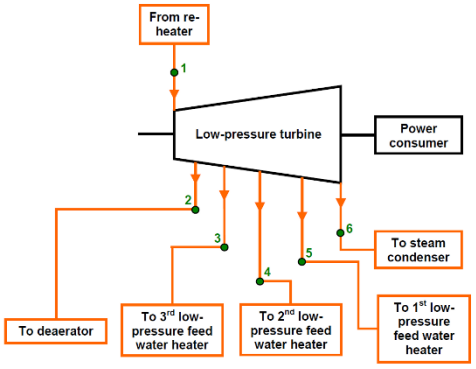

Fig. 1. *Scheme and marked operating points of the analyzed low-pressure steam turbine*

Ideal (isentropic) and real (polytropic) steam expansion processes through the analyzed turbine are shown in Fig. 2 (operating points are in accordance to Fig. 1). Real (polytropic) steam expansion process is marked with numbers from 1 to 6, while ideal (isentropic) expansion is marked with numbers from 1 to 6i. Ideal (isentropic) process assumes that steam specific entropy remains constant during expansion [15]. Steam extractions are marked with red arrows (operating points 2, 3, 4 and 5).

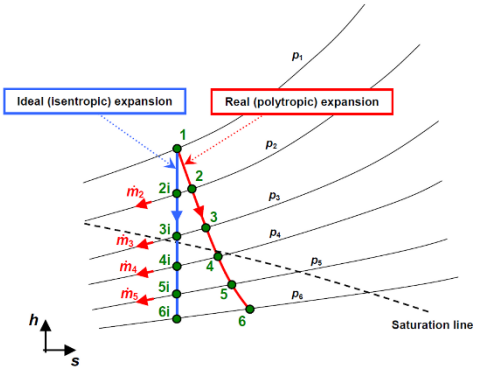

Fig. 2. *Steam real (polytropic) and ideal (isentropic) expansion processes through the analyzed turbine in h-s diagram*

3. Equations for the low-pressure steam turbine energy and exergy analysis

3.1. General energy and exergy equations and balances

The main energy and exergy balance equations are [16]:

$$\dot{Q}_{\text{in}} + P_{\text{in}} + \sum \dot{E}n_{\text{in}} = \dot{Q}_{\text{out}} + P_{\text{out}} + \sum \dot{E}n_{\text{out}} + \dot{E}n_{\text{L}}, \quad (1)$$

$$\dot{X}_{\text{in}} + P_{\text{in}} + \sum \dot{E}x_{\text{in}} = \dot{X}_{\text{out}} + P_{\text{out}} + \sum \dot{E}x_{\text{out}} + \dot{E}x_{L}, \quad (2)$$

where $\dot{Q}$ and $\dot{X}$ are heat energy and exergy transfer, P is mechanical power, index in is related to the inlet (input), index out is related to outlet (output) and index L is related to the loss (energy or exergy). $\dot{E}n$ and $\dot{E}x$ are total energy and exergy flow of any fluid stream which can be calculated as [17]:

$$\dot{E}n = \dot{m} \cdot h, \tag{3}$$
$$\dot{E}x = \dot{m} \cdot \varepsilon, \tag{4}$$

where $\dot{m}$ is mass flow rate, h is specific enthalpy and ε is specific exergy. Always valid mass flow rate balance is:

$$\sum \dot{m}_{\text{in}} = \sum \dot{m}_{\text{out}}, \tag{5}$$

while overall energy and exergy efficiency equation can be presented as [18]:

$$\eta_{\text{en(ex)}} = \frac{\text{cumulative energy (exergy) output}}{\text{cumulative energy (exergy) input}}. \tag{6}$$

3.2. Equations for the energy and exergy analysis of the observed low-pressure steam turbine

Equations for the energy and exergy analyses of the investigated low-pressure steam turbine are presented in this subsection for a situation when all of the steam extractions are open. Equations for the turbine energy and exergy analyses when one or more steam extractions are closed will be defined by using the same equations (mass flow rate through closed extraction is equal to zero).

Equations for the low-pressure steam turbine energy analysis (all steam extractions open), according to Fig. 1 and Fig. 2, are:

- Turbine real (polytropic) mechanical power:

$$P_{\text{re}} = \dot{m}_1 \cdot (h_1 - h_2) + (\dot{m}_1 - \dot{m}_2) \cdot (h_2 - h_3) + (\dot{m}_1 - \dot{m}_2 - \dot{m}_3) \cdot (h_3 - h_4) + (\dot{m}_1 - \dot{m}_2 - \dot{m}_3 - \dot{m}_4) \cdot (h_4 - h_5) + (\dot{m}_1 - \dot{m}_2 - \dot{m}_3 - \dot{m}_4 - \dot{m}_5) \cdot (h_5 - h_6). \tag{7}$$

- Turbine ideal (isentropic) mechanical power:

$$P_{\text{id}} = \dot{m}_1 \cdot (h_1 - h_{2\text{i}}) + (\dot{m}_1 - \dot{m}_2) \cdot (h_{2\text{i}} - h_{3\text{i}}) + (\dot{m}_1 - \dot{m}_2 - \dot{m}_3) \cdot (h_{3\text{i}} - h_{4\text{i}}) + (\dot{m}_1 - \dot{m}_2 - \dot{m}_3 - \dot{m}_4) \cdot (h_{4\text{i}} - h_{5\text{i}}) + (\dot{m}_1 - \dot{m}_2 - \dot{m}_3 - \dot{m}_4 - \dot{m}_5) \cdot (h_{5\text{i}} - h_{6\text{i}}). \tag{8}$$

- Turbine energy loss (energy destruction):

$$\dot{E}n_{\text{L}} = P_{\text{id}} - P_{\text{re}}. \tag{9}$$

- Turbine energy efficiency:

$$\eta_{\text{en}} = \frac{P_{\text{re}}}{P_{\text{id}}}. \tag{10}$$

Exergy analysis depends on the ambient conditions. The ambient conditions (dead state conditions) in this analysis are: pressure of 1 bar and a temperature of 25 °C. For the steam turbine exergy analysis, the relevant turbine mechanical power is real (polytropic) power, calculated by Eq. 7 for the situation when all steam extractions are open. Equations for the exergy analysis of investigated low-pressure steam turbine with all steam extractions open, Fig. 1, are:

- Turbine exergy inlet (input):

$$\dot{E}x_{\text{in}} = \dot{m}_1 \cdot \varepsilon_1. \tag{11}$$

- Turbine exergy outlet (output):

$$\dot{E}x_{\text{out}} = \dot{m}_2 \cdot \varepsilon_2 + \dot{m}_3 \cdot \varepsilon_3 + \dot{m}_4 \cdot \varepsilon_4 + \dot{m}_5 \cdot \varepsilon_5 + \dot{m}_6 \cdot \varepsilon_6 + P_{\text{re}}. \tag{12}$$

- Turbine exergy loss (exergy destruction):

$$\dot{E}x_{\text{L}} = \dot{E}x_{\text{in}} - \dot{E}x_{\text{out}}. \tag{13}$$

- Turbine exergy efficiency:

$$\eta_{\text{ex}} = \frac{P_{\text{re}}}{\dot{E}x_{\text{in}} - \dot{E}x_{\text{out}} + P_{\text{re}}}. \tag{14}$$

All equations for the analyzed turbine during one or more steam extractions closing remains the same as presented above, from Eq. 7 to Eq. 14. The closing of one or more steam turbine extractions means that steam mass flow rate through closed steam extraction is equal to zero. All other steam operating parameters remain the same as in the situation when all steam turbine extractions are open. The calculation principle is always the same, regardless of observed steam turbine extractions opening/closing combination.

4. Steam operating parameters required for low-pressure steam turbine energy and exergy analysis

Each fluid flow stream operating parameters (in each operating point from Fig. 1) measured in the power plant are found in [12]. Using measured operating parameters, all the others, required for the energy and exergy analyses are calculated with NIST-Refprop 9.0 software [19]. Steam operating parameters in each operating point from Fig. 1 and Fig. 2 are presented in Table 1 for real (polytropic) expansion process and in Table 2 for ideal (isentropic) process. It should be highlighted that ideal expansion process is a process between the same pressures and it uses the same mass flow rates as the real (polytropic) process, but in ideal process steam specific entropy remains always constant, as at the turbine inlet.

Table 1. *Steam operating parameters in each operating point of the analyzed turbine – real (polytropic) steam expansion*

O.P.	Temperature (°C)	Pressure (bar)	Mass flow rate (kg/s)	Specific enthalpy (kJ/kg)	Specific entropy (kJ/kg·K)	Specific exergy (kJ/kg)
1	371.000	17.090	33.200	3187.0	7.1065	1072.8
2	279.153	7.980	3.170	3012.8	7.1574	883.4
3	165.472	2.730	1.790	2796.0	7.2027	653.1
4	98.456	0.960	1.570	2625.4	7.2442	470.1
5	68.301	0.290	1.240	2455.8	7.2892	287.1
6	41.490	0.080	25.430	2343.1	7.4868	115.4

O.P. = Operating point (refers to Fig. 1.)

Table 2. *Steam operating parameters in each operating point of the analyzed turbine – ideal (isentropic) steam expansion*

O.P.	Pressure (bar)	Mass flow rate (kg/s)	Isentropic specific enthalpy (kJ/kg)	Isentropic specific entropy (kJ/kg·K)
1	17.090	33.200	3187.0	7.1065
2i	7.980	3.170	2985.1	7.1065
3i	2.730	1.790	2754.8	7.1065
4i	0.960	1.570	2574.3	7.1065
5i	0.290	1.240	2393.5	7.1065
6i	0.080	25.430	2223.5	7.1065

O.P. = Operating point (refers to Fig. 2.)

Steam operating parameters in each analyzed turbine operating point found in [12] were presented in a situation when all steam extractions are open. Steam extractions closing do not affect steam operating parameters, they remain the same as presented in Table 1 and Table 2 (only the steam mass flow rate is set to zero for any closed extraction).

The analyzed low-pressure steam turbine has four steam extractions (operating points 2, 3, 4 and 5, Fig. 1). All possible combinations of the steam extractions opening/closing are presented in Table 3. Turbine operating parameters were investigated for each possible combination.

From Table 3 can be seen that the first combination is when all steam turbine extractions are open while the last combination is when all steam turbine extractions are closed. There are four possible combinations when one turbine extraction is closed and all the others are open (combinations from 2 to 5, Table 3) and six possible combinations when two turbine extractions are open and two are closed (combinations from 6 to 11, Table 3). Finally, there are four possible combinations when three steam extractions are closed with only one open (combinations from 12 to 15, Table 3).

Table 3. *Steam extractions opening/closing combinations*

Steam extractions combination number	Steam extractions* (2-3-4-5)
1	o-o-o-o
2	c-o-o-o
3	o-c-o-o
4	o-o-c-o
5	o-o-o-c
6	c-c-o-o
7	o-c-c-o
8	o-o-c-c
9	c-o-c-o
10	c-o-o-c
11	o-c-o-c
12	c-c-c-o
13	o-c-c-c
14	c-o-c-c
15	c-c-o-c
16	c-c-c-c

* o = extraction open; c = extraction closed

5. The results of the low-pressure steam turbine energy and exergy analysis during steam extractions opening/closing

The change in real (polytropic) and ideal (isentropic) turbine mechanical power during steam extractions opening/closing is presented in Fig. 3. It is evident that trends in both ideal and real power are identical and that ideal power is higher than the real one, regardless of the observed combination (because the ideal power did not consider losses which occur during steam expansion).

As can be expected, combination 1 when all steam extractions are open resulted with the lowest mechanical power, while combination 16 which represents all closed steam extractions resulted with the highest produced mechanical power (both ideal and real). The highest mechanical power which can be produced by this turbine (all steam extractions closed) is 28017.48 kW in real and 31988.20 kW in an ideal situation. If only one steam extraction is closed (combinations from 2 to 5), the highest produced mechanical power is observed when the first steam extraction is closed (combination 2). In the situation of two closed extractions (combinations from 6 to 11), the highest power is obtained when first two extractions are closed (combination 6). Finally, the highest power in the situation when three steam extractions are closed is obtained in combination 12 when first three extractions are closed.

From Fig. 3 can be concluded that closing the steam extractions which are the closest to the turbine inlet has a notable effect on the increase in turbine power because more steam will expand through the turbine and more mechanical power will be produced.

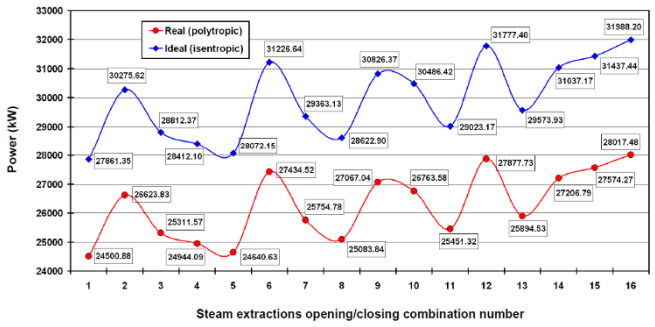

Fig. 3. *Change in real (polytropic) and ideal (isentropic) power during turbine extractions opening/closing*

The influence of steam extractions opening/closing on the observed low-pressure turbine energy efficiencies and energy losses is presented in Fig. 4. The highest energy efficiency and the lowest turbine energy loss can be seen when all steam extractions are open (combination 1), while one of the lowest turbine energy efficiency and the highest energy loss is observed in a situation when all steam extractions are closed (Combination 16). For all observed steam extractions opening/closing combinations, it can be concluded that energy efficiency and energy loss range is relatively small (from 87.56% to 87.94% for energy efficiency and from 3360.46 kW to 3970.72 kW for energy loss).

Final conclusion which can be derived from Fig. 3 and Fig. 4 is that steam extractions closing increases produced mechanical power and energy losses, while simultaneously decreases turbine energy efficiency.

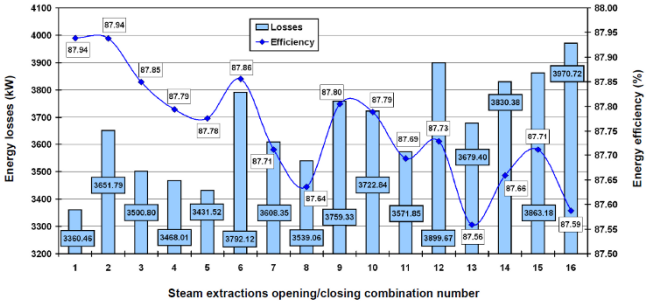

Fig. 4. *Change in energy losses and energy efficiencies during turbine extractions opening/closing*

Exergy input of the observed turbine is always the same (equal to 35616.96 kW), regardless of the observed extractions opening/closing combination. However, turbine exergy output is changing for the observed extractions opening/closing combinations, as presented in Fig. 5. The highest turbine exergy output equal to 32498.99 kW can be observed in combination 1 (all extractions opened), while the lowest turbine exergy output equal to 31848.76 kW is obtained in combination 16 (all extractions closed). From Fig. 5 can also be observed that steam extractions closing from the turbine inlet to the turbine outlet reduce exergy output.

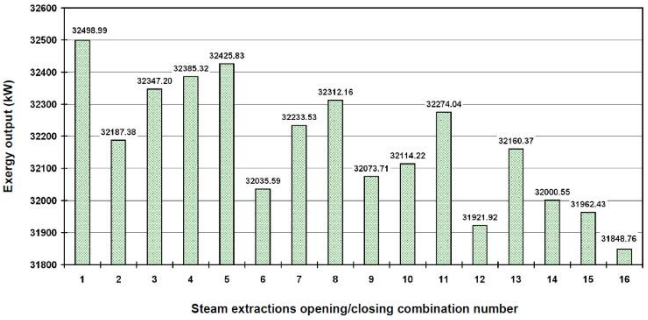

Fig. 5. *Change in exergy output during turbine extractions opening/closing*

Change in exergy loss (exergy destruction) and exergy efficiency of the observed low-pressure steam turbine during extractions opening/closing is presented in Fig. 6.

Comparison of turbine energy losses (energy destructions), Fig. 4, and turbine exergy losses (exergy destructions), Fig. 6, shows that the trends in losses are identical for all observed extractions opening/closing combinations. Exergy efficiencies show slightly different trends in comparison to energy efficiencies. However, the dominant conclusion is valid regardless of the observed analysis – steam extractions closing decreases turbine efficiencies and increases turbine losses (destructions).

For the observed extractions opening/closing combinations, turbine exergy efficiency range is between 88.71% and 88.14%. It can be concluded that observed turbine efficiencies (both energy and exergy) will decrease for a maximum 1% during the steam extractions closing.

Further analysis related to the observed low-pressure steam turbine and steam extractions opening/closing combinations will be based on various Artificial Intelligence (AI) methods and processes [20-22]. The aim will be to find optimal steam extractions opening/closing combination (along with partially opened extractions) to perform the complete optimization of the observed steam turbine.

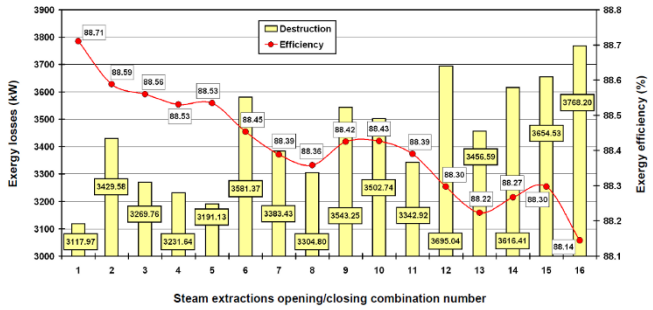

Fig. 6. *Change in exergy losses and exergy efficiencies during turbine extractions opening/closing*

6. Conclusions

This paper presents energy and exergy analysis results of a low-pressure steam turbine during its extractions opening/closing. It is observed all possible combinations of extractions opening/closing, with whole mass flow rates (partial mass flow rates were not observed). The most important obtained conclusions are:

- The highest mechanical power which can be produced by this turbine (when all steam extractions are closed) is 28017.48 kW in real and 31988.20 kW in an ideal situation.
- Closing the steam extractions which are the closest to the turbine inlet has a notable effect on the increase in turbine power because more steam will expand through the turbine and more mechanical power will be produced.
- For all observed steam extractions opening/closing combinations is obtained that energy efficiency and energy losses range is relatively small (from 87.56% to 87.94% for energy efficiency and from 3360.46 kW to 3970.72 kW for energy losses).
- Trends in energy and exergy losses (destructions) are identical for all observed extractions opening/closing combinations.
- Observed turbine efficiencies (both energy and exergy) will decrease for a maximum 1% during the steam extractions closing.
- Steam extractions closing decreases turbine efficiencies and increases turbine losses (destructions), what is valid from both energy and exergy aspects.

7. Acknowledgment

This research has been supported by the Croatian Science Foundation under the project IP-2018-01-3739, University of Rijeka scientific grant uniri-tehnic-18-18-1146 and University of Rijeka scientific grant uniri-tehnic-18-14.

8. References

[1] Guo, J. Q., Li, M. J., Xu, J. L., Yan, J. J., & Ma, T. (2020). Energy, exergy and economic (3E) evaluation and conceptual design of the 1000 MW coal-fired power plants integrated with S-CO2 Brayton cycles. Energy Conversion and Management, 211, 112713. (doi:10.1016/j.enconman.2020.112713)

[2] Bolatturk, A., Coskun, A., & Geredelioglu, C. (2015). Thermodynamic and exergoeconomic analysis of Çayırhan thermal power plant. Energy conversion and management, 101, 371-378. (doi:10.1016/j.enconman.2015.05.072)

[3] Mrzljak, V., Senčić, T., & Žarković, B. (2018). Turbogenerator steam turbine variation in developed power: Analysis of exergy efficiency and exergy destruction change. Modelling and Simulation in Engineering, 2018. (doi:10.1155/2018/2945325)

[4] Mrzljak, V., Poljak, I., & Mrakovčić, T. (2017). Energy and exergy analysis of the turbo-generators and steam turbine for the main feed water pump drive on LNG carrier. Energy conversion and management, 140, 307-323. (doi:10.1016/j.enconman.2017.03.007)

[5] Nikam, K. C., Kumar, R., & Jilte, R. (2020). Exergy and exergo-environmental analysis of a 660 MW supercritical coal-fired power plant. Journal of Thermal Analysis and Calorimetry, 1-14. (doi:10.1007/s10973-020-10268-y)

[6] Naserbegi, A., Aghaie, M., Minuchehr, A., & Alahyarizadeh, G. (2018). A novel exergy optimization of Bushehr nuclear power plant by gravitational search algorithm (GSA). Energy, 148, 373-385. (doi:10.1016/j.energy.2018.01.119)

[7] Nikam, K. C., Kumar, R., & Jilte, R. (2020). Economic and exergoeconomic investigation of 660 MW coal-fired power plant. Journal of Thermal Analysis and Calorimetry, 1-15. (doi:10.1007/s10973-020-10213-z)

[8] Kopac, M., & Hilalci, A. (2007). Effect of ambient temperature on the efficiency of the regenerative and reheat Çatalağzı power plant in Turkey. Applied Thermal Engineering, 27(8-9), 1377-1385. (doi:10.1016/j.applthermaleng.2006.10.029)

[9] Mrzljak, V., Prpić-Oršić, J., & Poljak, I. (2018). Energy power losses and efficiency of low power steam turbine for the main feed water pump drive in the marine steam propulsion system. Pomorski zbornik, 54(1), 37-51. (doi:10.18048/2018.54.03)

[10] Mrzljak, V., & Poljak, I. (2019). Energy analysis of main propulsion steam turbine from conventional LNG carrier at three different loads. NAŠE MORE: znanstveni časopis za more i pomorstvo, 66(1), 10-18. (doi:10.17818/NM/2019/1.2)

[11] Anđelić, N., Mrzljak, V., Lorencin, I., & Baressi Šegota, S. (2020). Comparison of Exergy and Various Energy Analysis Methods for a Main Marine Steam Turbine at Different Loads. Pomorski zbornik, 59(1), 9-34. (doi:10.18048/2020.59.01)

[12] Vakilabadi, M. A., Bidi, M., & Najafi, A. F. (2018). Energy, Exergy analysis and optimization of solar thermal power plant with adding heat and water recovery system. Energy conversion and management, 171, 1639-1650. (doi:10.1016/j.enconman.2018.06.094)

[13] Mrzljak, V., Poljak, I., & Medica-Viola, V. (2016). Efficiency and losses analysis of low-pressure feed water heater in steam propulsion system during ship maneuvering period. Pomorstvo, 30(2), 133-140. (doi:10.31217/p.30.2.6)

[14] Medica-Viola, V., Pavković, B., & Mrzljak, V. (2018). Numerical model for on-condition monitoring of condenser in coal-fired power plants. International Journal of Heat and Mass Transfer, 117, 912-923. (doi:10.1016/j.ijheatmasstransfer.2017.10.047)

[15] Medica-Viola, V., Baressi Šegota, S., Mrzljak, V., & Štifanić, D. (2020). Comparison of conventional and heat balance based energy analyses of steam turbine. Pomorstvo, 34(1), 74-85. (doi:10.31217/p.34.1.9)

[16] Aljundi, I. H. (2009). Energy and exergy analysis of a steam power plant in Jordan. Applied thermal engineering, 29(2-3), 324-328. (doi:10.1016/j.applthermaleng.2008.02.029)

[17] Mrzljak, V., Poljak, I., & Medica-Viola, V. (2017). Dual fuel consumption and efficiency of marine steam generators for the propulsion of LNG carrier. Applied Thermal Engineering, 119, 331-346. (doi:10.1016/j.applthermaleng.2017.03.078)

[18] Kanoğlu, M., Çengel, Y. A., & Dinçer, İ. (2012). Efficiency evaluation of energy systems. Springer Science & Business Media.

[19] Lemmon, E. W., Huber, M. L., & McLinden, M. O. (2010). NIST Standard Reference Database 23, Reference Fluid Thermodynamic and Transport Properties (REFPROP), version 9.0, National Institute of Standards and Technology. R1234yf. fld file dated December, 22, 2010.

[20] Lorencin, I., Anđelić, N., Mrzljak, V., & Car, Z. (2019). Genetic algorithm approach to design of multi-layer perceptron for combined cycle power plant electrical power output estimation. Energies, 12(22), 4352. (doi:10.3390/en12224352)

[21] Mrzljak, V., Anđelić, N., Lorencin, I., & Sandi Baressi Šegota, S. (2021). The influence of various optimization algorithms on nuclear power plant steam turbine exergy efficiency and destruction. Pomorstvo, 35(1), 69-86. (doi:10.31217/p.35.1.8)

[22] Anđelić, N., Baressi Šegota, S., Lorencin, I., Poljak, I., Mrzljak, V., & Car, Z. (2021). Use of Genetic Programming for the Estimation of CODLAG Propulsion System Parameters. Journal of Marine Science and Engineering, 9(6), 612. (doi:10.3390/jmse9060612)

Visualization and analysis of worm gear drives efficiency and load capacity

Svetlin Stoyanov, Gergana Mollova
University of Ruse "Angel Kanchev", 8 Studentska str., POB 7017, Ruse, Bulgaria
SStoyanov@Uni-Ruse.BG, Gergana_Mollova@yahoo.co.uk

Abstract: *Scientific methodologies have been created and applied during the analysis upon worm gear drives. Important parameters have been selected in order to make significant investigations in the area of worm gear efficiency and load capacity. The efficiency coefficient and maximal torque values have been studied for several combinations of modules, ratios, center distances, etc. The results have been presented and analysed through three-dimensional graphics. Conclusions are made.*
Keywords*: WORM GEAR DRIVES, GEAR EFFICIENCY, LOAD CAPACITY, SCIENTIFIC METHODOLOGIES, EFFICIENCY COEFFICIENT, MAXIMAL TORQUE, SOFTWARE SYSTEMS, COMPUTER-AIDED MATHEMATICS, THREE-DIMENSIONAL GRAPHICS.*

1. Introduction

A worm drive is a power transmission device in which a worm meshes with a worm gear to transmit power between two non-intersecting shafts that are oriented at a right angle. Worm gear drives are quite suitable for transmitting large gear ratios in one stage.

Some important features of worm gears are:

- ⇨ A probability to achieve self-locking when reversing the direction of the power flow;
- ⇨ Quiet operation capacity;
- ⇨ Suitable when the space is limited;
- ⇨ Absorption of shock loading;
- ⇨ Minimum maintenance.

Small changes in parameters of worm gear drives can lead to the significant savings which is not the case in other drives [8]. This makes the selection of parameters of these drives to be a very important topic, which product development engineers are often not aware.

The main criterion for worm gear load capacity is the output torque of the worm gear shaft, which is directly connected to the driven machine. Output torque values could be limited certain conditions during transmission operation. Some significant boundary conditions are [1, 2, 3, 14]:

- ⇨ pitting, which can appear on the active flanks of the worm gear teeth;
- ⇨ wear, which usually on the flanks of the bronze worm gear;
- ⇨ heating of transmission and scuffing, which depends on the load and sliding velocity values.

The friction coefficient in the meshing represents a complex characteristic regarding the quality of the worm gear train. Several different approaches and models have been presented in previous research by the authors' team. The German standard DIN 3996: 2012-09 describes a short and clear approach [12]. On the other hand, the approach described in [16] and [17] presents a more complex and detailed method.

Besides, the investigations described in [16] and [17] treat other important problems for worm gear drives. The authors of these publications analyze the temperature and temperature variations in the contact meshing area. They emphasize that these variations could have relative great influence upon the wear of the worm gears. In other previous publications of the authors' team, the calculations for various parameters of worm gears have been analyzed. Some main calculation approaches are standardized in [10, 9, 11, 13].

The authors' team and other scientists from the ***University of Ruse*** have successfully completed some investigation tasks in the field of energy efficiency of drive systems and transmissions. The results of these studies are presented in detail in the following publications: [1-7].

2. A historical overview of this research

In [14], a new methodology was been created including several stages. The methodology involves the application of the scientific approach described in [15].

The new methodology from [14], starts with calculating the tangential frequency, the sliding speed, the efficiency coefficient, and the important tribology parameters. The calculations are carried out for a worm made of case-hardened steel 16 MnCr5 and for a worm made of GZ-CuSn12Ni. The necessary parameters are defined, trough which it becomes possible to determine the maximal actual contact stresses. Upon these calculations, the maximal output torque T_2 is determined. A database is generated and a graphical presentation is created.

Also, an optimization procedure has been created aiming to improve the load capacity parameters of worm gear trains [14]. Different functional parameters and certain geometry parameters have been taken into account such as rotating frequency of the worm shaft, gear ratio, module and geometry dimensions of the worm gear set.

Based upon the methodology described, in [14, 15] a substantial investigation has been carried out. The object of analysis and discussion of the paper presented will be the results concerning the center distance a = 50 mm. The calculation results for the efficiency coefficients ηz and maximal output torques T_2 in Nm depending on gear ratios i and modules m (in mm) at center distance a = 50 mm and n_1 = 1500 min^{-1} are summarized in Table 1 [14]. The calculations are carried out with 9 different values of the gear ratios i and 3 different values of the module m.

Table 1: *Results for center distance* a *= 50 mm and* n_1 *= 1500 min*$^{-1}$

	i	***m***	***ni***	***T2***
1	4.83	2.5	0.9314	14.97
2	7.25	2.5	0,9120	24,79
3	9,5	2	0,8994	30,91
4	14,5	2,5	0,8478	58,43
5	19	2	0,8289	72,67
6	29	2,5	0,7445	136,61

On this stage of the research, a question haw to present and analyze the data obtained raising.

In [1, 2, 14, 15] this is solved with the help of the software system ***MS Excel***. A plain 2-D graphs are created to visualize the relations obtained.

In [18] is analyzed an idea to use the flexibility and power of the contemporary computer-aided mathematics software systems.

For example, Fig. 1 and Fig. 2 [14] shows the variation of coefficient of efficiency and output torque in a graphical way depending on the values of the gear ratio and the module.

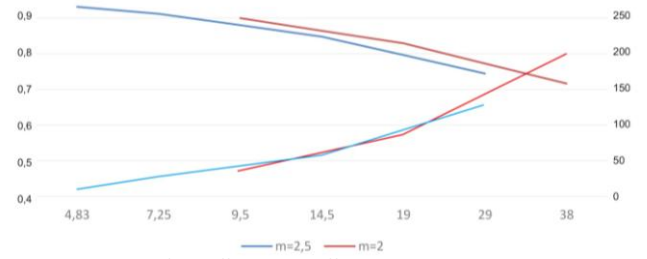

***Fig. 1**. Variation of the efficiency coefficients and maximal output torques for a center distance a = 50 mm and rotation speed of worm gear shaft n_1 = 1500 min^{-1}.*

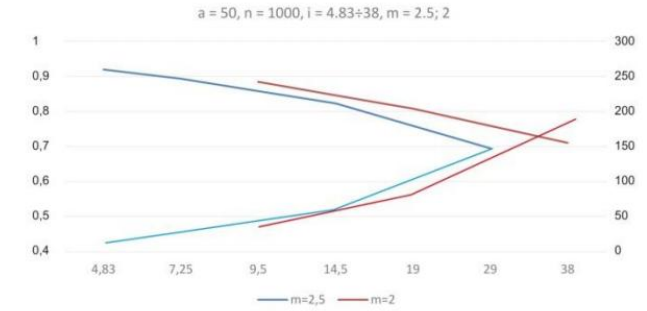

***Fig. 2**. Variation of the efficiency coefficients and maximal output torques for a center distance a = 50 mm and rotation speed of worm gear shaft n_1 = 1000 min^{-1}.*

In [14], a conclusion has been made that the area of maximal values of efficiency efficient and output torques is located in the gear ratio interval between 20 and 29 with modulus equal to 2 mm and 2.5 mm.

3. A new methodology – data interpolation and three-dimensional visualisation

The contemporaly growth of software systems provides powerfull new opportunities in all areas of engineering and science. This also applies to the field of mathematics. The systems ***MATLAB, Wolfram Mathematica*** and ***Maple*** can be cited as leading systems for computer-aided mathematics [18].

With the help of software system ***MATLAB***, the calculated in [14, 15] data has been interpolated and visualized [18]. This gives two new abilities, as follows:

- ⇨ An ability to directly signify the relations between three parameters (or even between four parameters, if the color in set as independent indicator);
- ⇨ An ability to render relations in uninterrupted three-dimensional space (or even in four-dimensional space, if the color in set as independent indicator).

It follows some three-dimensional visualisation created and the conclusions obtained from them.

3.1. Efficiency coefficient in relation from ratio and module

Colored three-dimensional graphs are created for the all combinations of:

- ⇨ **center distances:** a = 50 mm, a = 63 mm, a = 80 mm, and a = 125 mm

and

- ⇨ **input rotation speeds**: n_1 = 750 min^{-1}, n_1 = 1000 min^{-1}, n_1 = 1500 min^{-1}.

In this paper are presented some of the characteristic plots. On Fig 3 is shown a graph composed of two planes. The second plane is located in the left down corner on Fig. 3a, but for this to be visible, the graph must be rotated as it is shown on Fig. 3b. The black straight line is the border between the planes.

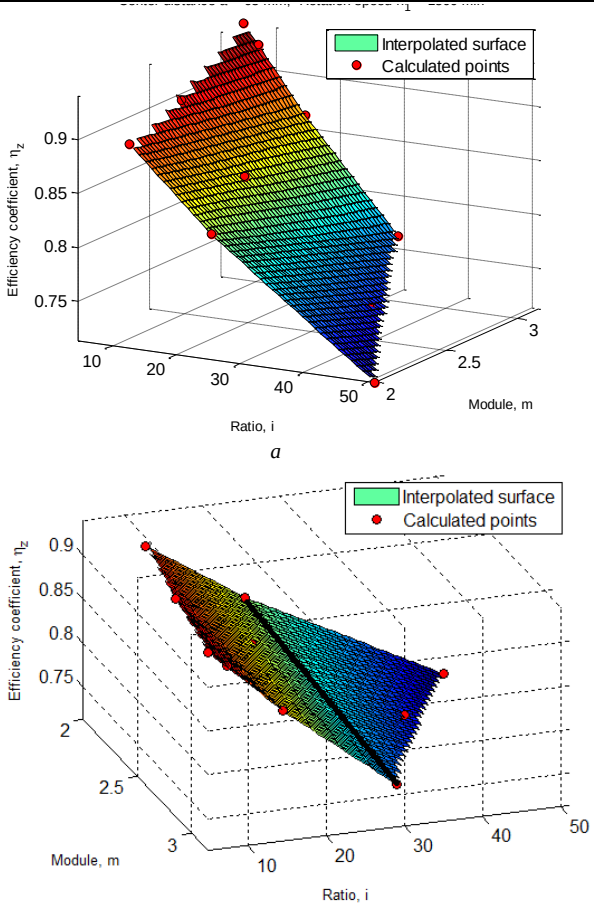

***Fig. 3.** Efficiency coefficient in relation from ratio and module for center distance a = 63 mm and rotation speed n_1 = 1500 min^{-1}.*

From Fig. 3, it can be observed that the efficiency coefficient increases with the increase of the module and the decrease of the ratio.

On Fig 4 is presented an analogical case, i.e., a surface that interpolates data points, one of which is higher than others. The relations of the efficiency coefficient from the ratio and module remains the same as on Fig 3.

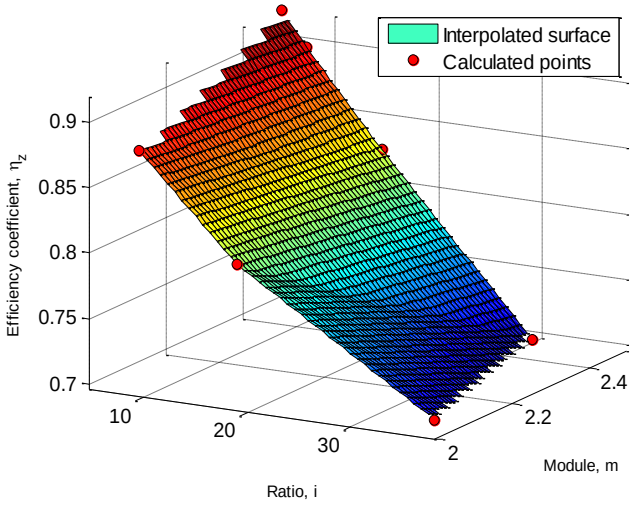

***Fig. 4.** Efficiency coefficient in relation from ratio and module for center distance a = 50 mm and rotation n_1 = speed 1000 min^{-1}.*

The next plot is example for two data points located about the middle of the interpolated surface, which are out of the plane – Fig. 5. It can be observed that in these points the efficiency coefficient has a higher value, than in the other points of the interpolated plane surface.

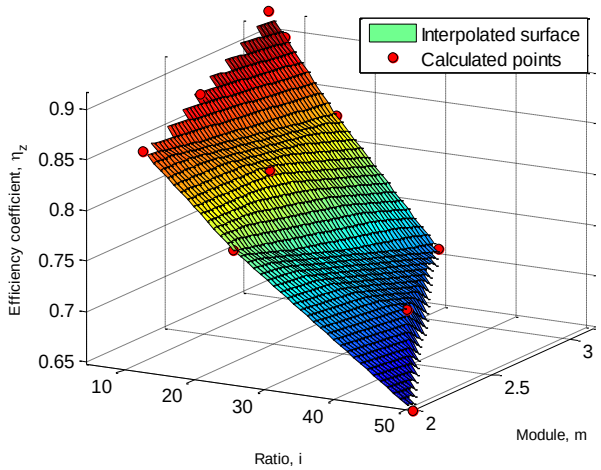

Fig. 5. *Efficiency coefficient in relation from ratio and module for center distance a = 63 mm and rotation speed n_1 = 750 min^{-1}.*

And, as the end of this section, Fig. 6 shows a different picture. There is a data point with lower value of the efficiency coefficient than other points in the plane interpolated surface. That is in the top left corner, i.e., in the area with higher values of the efficiency coefficient.

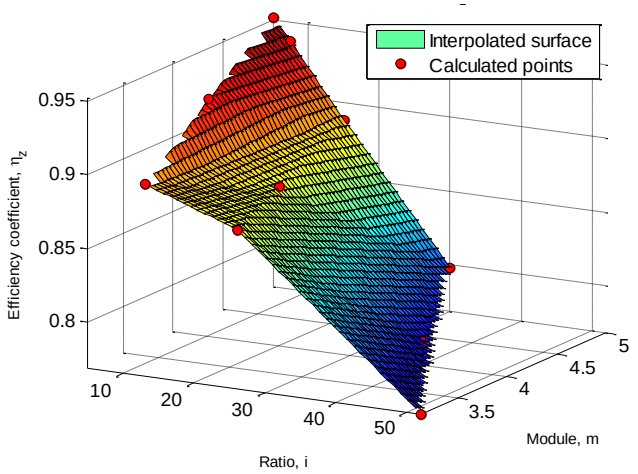

Fig. 6. *Efficiency coefficient in relation from ratio and module for center distance a = 100 mm and rotation speed n_1 = 1500 min^{-1}.*

The trend of the dependence of the efficiency coefficient from the ratio and module permanently becomes unchanged and is confirmed in all four figures from Fig. 3 to Fig. 6.

3.2. Efficiency coefficient in relation from ratio and output torque

On Fig. 7 is shown a relation of the efficiency coefficient from the ratio and the output torque T_2. **It can be concluded that, the efficiency coefficient grows with decreasing the output torque and the ratio.**

The software system ***MATLAB*** gives the ability multiple three-dimensional surfaces to be superimposed. On Fig. 8b are presented two three-dimensional relations together for center distance a = 63 mm and rotation speed n_1 = 1500 min^{-1}, as follows:

- ⇨ the dependence of the efficiency coefficient from the ratio and module;
- ⇨ the dependence of the efficiency coefficient from the ratio and **output torque.**

The relations for efficiency coefficient ant the output torque for other center distances and input rotation speeds are also investigated. Some of them are shown oh Fig. 9, Fig. 10, and Fig. 11. From these graphs, it can be concluded that **the trend of the dependence of the efficiency coefficient from the ratio and the output torque becomes unchanged, i.e., the efficiency coefficient grows with decreasing the output torque and the ratio.**

The presented results can be used for performing an optimization process with ***MATLAB Optimization Toolbox*** [18]. It provides functions for finding parameters that minimize or maximize objectives while satisfying constraints. The toolbox includes solvers for linear programming (LP), mixed-integer linear programming (MILP), quadratic programming (QP), second-order cone programming (SOCP), nonlinear programming (NLP), constrained linear least squares, nonlinear least squares, and nonlinear equations.

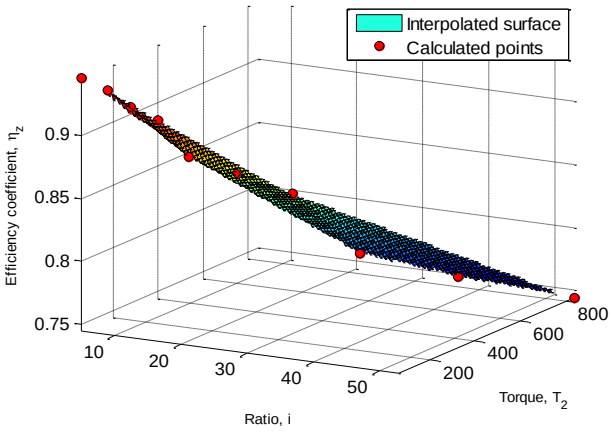

Fig. 7. *Efficiency coefficient for center distance a = 80 mm and rotation speed n_1 = 1500 min^{-1}.*

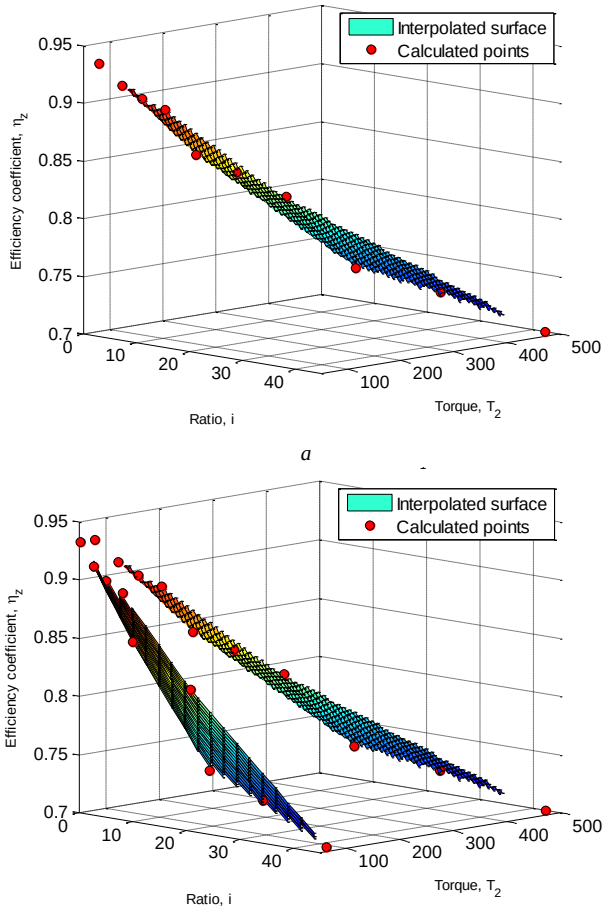

Fig. 8. *Efficiency coefficient for center distance a = 63 mm and rotation speed n_1 = 1500 min^{-1}: a – efficiency coefficient in function of ratio and torque; b – with superimposed surface of efficiency coefficient in function of ratio and module.*

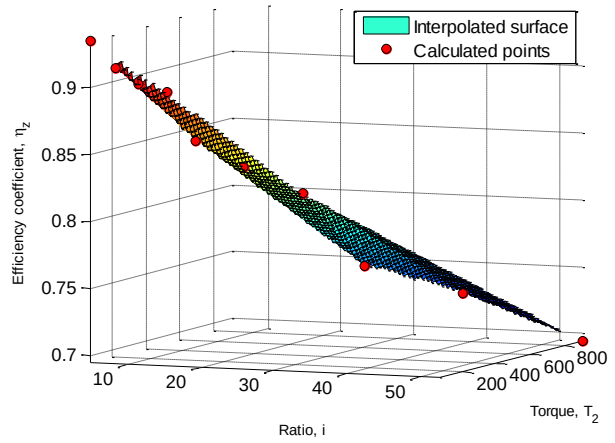

Fig. 9. *Efficiency coefficient and output torque for center distance a = 80 mm and rotation speed n_1 = 1000 min^{-1}.*

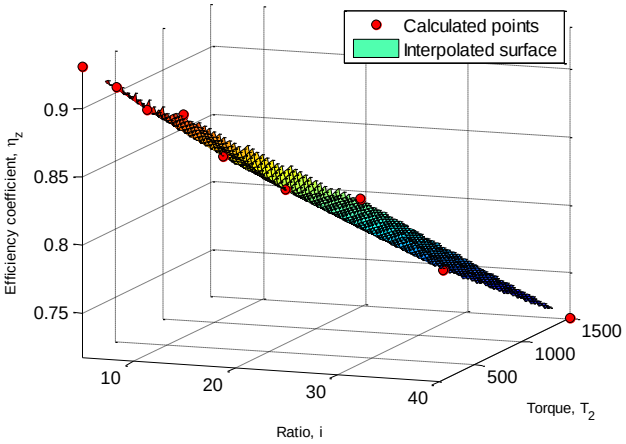

Fig. 10. *Efficiency coefficient and output torque for center distance a = 100 mm and rotation speed n_1 = 750 min^{-1}.*

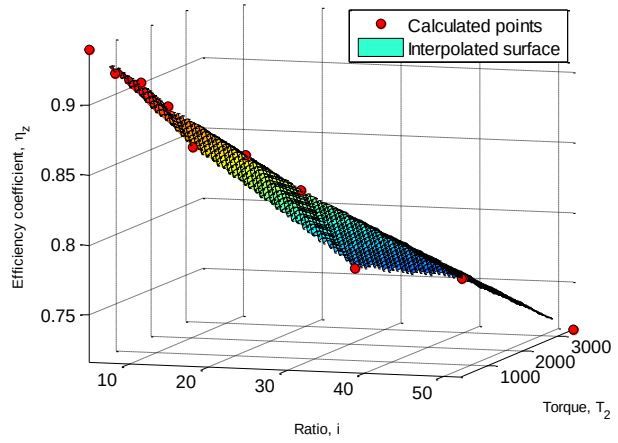

Fig. 11. *Efficiency coefficient and output torque for center distance a = 125 mm and rotation speed n_1 = 750 min^{-1}.*

4. Conclusions

The efficiency coefficient and maximal torque values have been investigated for several combinations of modules, ratios, center distances, etc. The results have been presented and analyzed through three-dimensional graphics. For the aim of this, a new methodology based on data interpolation and three-dimensional visualization are developed and applied.

From the results obtained, it can be concluded that the efficiency coefficient increases with the increase of the module and the decrease of the ratio. This trend remains for all the cases studied. Although this trend, there is some exceptions for local points as it is noted specifically when the graphs were discussed.

It is established that the efficiency coefficient grows with decreasing the output torque and the ratio. This trend is also stable for all cases studied.

MATLAB Optimization Toolbox™ lets design optimization tasks to be conducted. It includes parameter estimation, component selection, and parameter tuning. In combination with computer-aided design software (CAD), this gives an ability the above presented research to be continued with development and investigation of an automatized optimization and design system. This can be done in the integrated working environment of the software systems ***MATLAB*** and ***SolidWorks***.

5. References

1. A. Dobreva, P. Pavlov. Energy Efficiency of Worm Gear Drives, Proceedings of the 32nd DAAAM International Symposium, pp.0110-0116 (2021)

2. A. Dobreva, V. Dobrev, G. Mollova. Research of gear drives. IOP Conf. Ser.: Mater. Sci. Eng. 1220-012025 (2022)

3. A. Dobreva. Methods for Improving the Geometry Parameters and the Energy Efficiency of Gear Trains with Internal Meshing. VDI – Berichte, No 2199. 2, pp. 1291 – 1302, (2013)

4. A. Dobreva & V. Dobrev. Improving the Tribological Characteristics of Heavy Loaded Gear Boxes. Proceedings of the First Balkan Conference on Tribology “Balkantrib’93”, Vol 2.3, Sofia, pp. 166-170, (1993)

5. A. Dobreva & V. Dobrev. Innovative Methodology for Decreasing Mechanical Losses in Vehicles. Proceedings of the 4th International Congress of Automotive and Transport Engineering (AMMA 2018), Springer Verlag, pp. 234 – 242, (2018)

6. A. Dobreva & S. Stoyanov. Optimization Research of Gear Trains with Internal Meshing. Ruse, University Publishing Centre, pp 144, (2012

7. A. Dobreva. Theoretical Investigation of the Energy Efficiency of Planetary Gear Trains. Mechanisms and Machine Science, No 13, pp. 289-298, (2013)

8. A. Miltenovic, M. Banic, D. Miltenović. Load capacity of worm gear transmission from aspect of maximal use of available resources. MATEC Web of Conferences (2017)

9. AGMA 6034-B92. Practice for Enclosed Cylindrical Wormgear Speed Reducers and Gearmotors. Alexandria, VA: American Gear Manufacturers Association, (2010)

10. Bulgarian National Standard 12256-78. Worm-gears cylindrical. Output worm and output production worm, (1978)

11. DIN 3976. Cylindrical worms; dimensions, coordination of centre distances and gear ratios of worm drives. Berlin, (1980)

12. DIN 3996. 2012-09. Load capacity calculation of cylindrical worm gears with axes crossing at 90 degree angles, Berlin, (2012)

13. DIN 3996. 2012-09. Load capacity calculation of cylindrical worm gears with axes crossing at 90 degree angles, Berlin, (2012).

14. G. Mollova, A. Dobreva. Improving load capacity parameters of worm gears. MATEC Web of Conferences 366, 02002 (2022)

15. G. Mollova, V. Dobrev. Design methodology for investigating worm gear transmissions with significant dimensions. IN: Proceedings of University of Ruse, Vol 60, ISSN: 1311-3321, pp. 41-47, (2021)

16. M. Oehler, B. Magyar, B. Sauer Coupled thermal and tribological analysis of worm gear. Tribol. Lubrication technology 65 (1), pp. 54–60, (2018)

17. M. Oehler, B. Magyar, B. Sauer. Worm gear efficiency – worm gear efficiency. Final report, Frankfurt am Main, (2016)

18. S. Stoyanov. Visualization and analysis of gear drives parameters with the help of computer-aided mathematics systems. XX Jubilee International Congress – Machines, Technologies, Materials, winter session, Borovets, Bulgaria (2023) (to be published)

Analysis of planetary gear trains applied in vehicles

Dimitar Bonev[1], Antoaneta Dobreva[1*]
University of Ruse, 8 "Studentska str., 7017 Ruse, Bulgaria[1]
adobreva@uni-ruse.bg

Abstract: *The paper presents a theoretical analysis in the field of the application of planetary gear trains in vehicles. The following main areas have been considered: design features of planetary gear trains, specific aspects of the application use of planetary gears in vehicles and possibilities of increasing the efficiency coefficient of these drives. An analysis of the option for investigating these gear sets has been implemented as well. Special attention is dedicated to the options of minimizing energy consumption, taking into account the relevant limitations and operating conditions of planetary gear trains. Conclusions have been deduces. Ideas for future scientific work are presented.*
Keywords*: PLANETARY GEAR TRAINS, APPLICATIONS IN VEHICLES, DESIGN, EFFICIENCY, FUNCTIONAL CHARACTERISTICS*

1. Introduction

Global warming issues and the demand for alternative sustainable transport make the issue of vehicle's selection an important and topical problem.

Fuel economy is one of the main technical parameters of vehicle efficiency. This indicator depends not only on the performance of the engine and the suspension, but also on the selection of the appropriate transmission. One of the most important environmental criteria in recent years is the reduction of harmful emissions released into the atmosphere. Almost 30% of total CO_2 emissions in the EU are due to the transport issues, with land, ground transport accounting for around 72% of these emissions, [1].

According to the EU's official website, automobiles account for around 15% of CO_2 emissions. Trucks and buses account for a quarter of road transport CO_2 emissions and for around 6% of total EU emissions. In 2021, the European Commission proposes to reduce the emission limits for new cars and vans by further 15% from 2025. Later on, a 55% reduction in emissions concerning new cars and a 50% reduction in emissions concerning new vans by 2030 is envisaged, i.e. reaching zero emissions by 2035, Fig.1, [2].

Fig.1. *EU transport emissions, [2]*

One of the priorities for reducing emissions is directly related to decreasing the fuel consumption of vehicles with internal combustion engines or to the development and production of electric and/or hybrid cars. One of the solutions for automatic transmission cars and heavy-duty vehicles can be found in the elaboration of high-efficiency power transmissions and gear drives.

Such transmissions and gear trains should be able to optimize energy consumption and at the same time: to provide the necessary power and to ensure the relevant precision when transmitting motion and torque.

Due to this reason, the author's team considers that the research problem regarding the selection of a suitable transmission and the improvement of its dynamic and functional characteristics is significant and topical matter.

The objective of the research presented is to determine the boundaries of application of gear trains in vehicle transmissions and the possibilities for improving the existing methods for creating theoretical models and applying modern approaches and tools.

2. Specific design features of planetary gear trains

Planetary gear trains are extremely often applied in automobiles and trucks because of their high gear ratio related to the overall dimensions of these gear drives. They are characterized by great compactness, i.e. relative small dimensions and small mass values: from 2 to 5 times less compared to spur and helical involute gear trains.

This advantage is due to the principle of multi-flow and to the application of several satellites which divide the power flow, [3]. Planetary gear trains are considered to be particularly suitable for hybrid vehicles and especially for: power split hybrids and plug-in hybrids, which are characterized by greater power values for certain time intervals.

Due to the advantages listed, planetary gear trains are used extremely often in the automotive industry. In [4], a systematic study of the various possible design schemes of planetary gear drives with two carriers and four external shafts has been made in order to indicate the most suitable deign options for the relevant specific application.

Considering planetary gear trains with two carriers, the design schemes with three external shafts according to [3] are most often used. Regarding gear drives with a variable transmission ratio, planetary gear sets with three, four and (recently) even five carriers, which can ensure large values of transmission ratios, have a significant application, [5].

Particularly interesting is the summary of the application of planetary gear trains with two carriers and four external shafts, which are quite suitable for changing the transmission ratio as two-speed or reversing mechanisms, [3].

Very important aspects of the application of planetary gear trains in vehicles are their kinematic capabilities. In [6], a comprehensive analysis of kinematic relationships in planetary gear sets has been made. It outlines the features of the design schemes, some characteristic limitations and conditions under which these gear drives are to be used.

In addition, the authors of [6] make an analysis of different automobile brands. They also highlight the differences in the configuration of the components and the relationship of the planetary gear design scheme with the operation modes of different automobiles.

Designing planetary gear trains for automobiles is a complex process that requires careful analysis of the vehicle's drive system.

The designers have to take into account the dimensions and weight of the vehicles, the type of drives, the necessary gear ratios and the torques values. In order to obtain better control systems and better efficiency, it is necessary to apply specific computational procedures to make solutions for these problems.

A suitable solution for designing a vehicle transmission through creating separate modules is suggested in [7], as shown in Fig. 2.

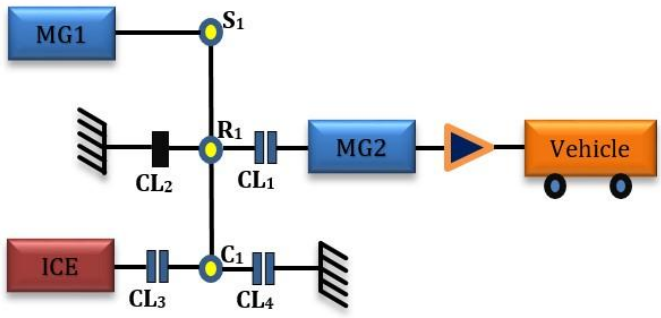

Fig.2. *Power flow in a transmission with one stage planetary gear train, [7]*

The design diagram of one stage planetary gear train includes: a motor (MG1) connected to the sun gear of the planetary gear set; a motor-generator (MG2) which is in contact with the ring gear and the engine which is assembled to the carrier gear.

This design scheme contains four clutches, Fig. 2. Depending on the type of their engagement, four modes can be generated. These options have been described in details in [7].

3. Applied aspects of the usage of planetary gear trains in vehicles

A significant aspect of the application of planetary gear trains in vehicles is their dynamic behavior. In [8], innovative theoretical models have been described. They can be considered useful tools for simulation studies of the dynamic behavior of planetary gear drives.

In [9] and [10], studies of natural frequencies and modes of vibration of planetary gear trains have been presented. The results of these studies are aimed at determining the resonance zone and setting up the resonances in areas that are far from the operating rotational frequencies. These specific features make the results obtained suitable for an optimization procedure when designing automotive transmissions.

The authors of [11] conducted a research study of the vibration characteristics of a single-stage planetary gearbox. They assume that the gearbox and the sensor rotate against the carrier and divide the problem into two parts: an investigation of the signal model of the gearbox with a fixed shaft and a test of the influence of the rotation of the sensor.

Based upon this assumption, a vibration signal model of a planetary gearbox has been obtained. The experimental results obtained have been used to validate the theoretical model. It can be considered that the results of this study are significant for practical applications.

Another group of important applied aspects of the usage of planetary gear trains in vehicles are the possibilities to achieve a significant improvement conserving the functional and operational parameters of these gear drive components.

According to these indicators, original theoretical models of planetary gear trains have been presented in [12-14]. The main purpose of the research in this area is to determine the conditions for noise and vibration reduction.

In [15, 16], an author's optimization study of vehicle drive systems based upon the frequency analysis of the components of these systems has been presented. The described results of these studies can be used in designing of automotive transmissions.

4. Options for increasing the efficiency of planetary gear trains

Modern researchers are presenting new solutions and models of planetary gear trains and reducers. For example, in [17] a method has been proposed that provides maximum power transmission efficiency for a 3K planetary gearbox. The authors of the study claim that the solution suggested has the following main advantages: a compact design structure and high values of the gear ratio.

As the efficiency increases, the ability to increase the gear ratio decreases according to [17]. The authors derive a relationship between the gear ratio and the control efficiency in single-stage high-reduction gearboxes. Their model approaches gearboxes involving a combination of a pair of spur involute gears.

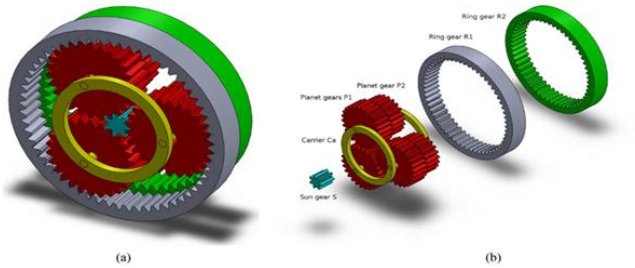

Fig.3. *Model of a 3K compound planetary gear train: (a) Assembled model. (b) Disassembled model, [17]*

Contemporary publications emphasize the importance of the application of planetary gear trains in Hybrid Electric Vehicles (HEVs). Their gearboxes are equipped with one or more planetary gears, characterized by high load capacity, compact design structure, high efficiency [18] and the capability to work as a two-stage transmission [19].

An innovative and interesting method for evaluating the efficiency coefficient in a planetary gear train has been presented in [20]. It can be assumed that the research mentioned has a practical application.

The research activities described in [17] also include a scientific analysis of the influence of the number of planetary gears used on the energy consumption concerning the optimal operation of the power transmission components.

Power transmissions with one and two planetary gear trains have been considered. A strategy for optimal simultaneous distribution of the torque and the selection of the operating mode has been proposed. The approach for energy management strategy (EMS) ensures distributes in optimal way the torque requirements between the power transmissions components, [17].

Besides, the role of clutch control has been emphasized, i.e. creating a mode selection option. The results show that when switching from one to two planetary gear trains, the energy consumption decreases by almost 4%, [17].

Another innovative methodology is the approach for improving the tribology performance of planetary gears with internal meshing and a small difference between the teeth number. The research mentioned is described in details in [21].

The evaluation of friction losses in meshing is closely related to the determination of specific slippage losses in gears with internal meshing.

In this investigation, the power losses in the meshing are based upon a factor that depends only on the geometrical parameters of the gear set and it affects in a significant way the efficiency coefficient in the meshing.

The values of power losses in planetary gear meshing are reported in some literature sources to be: from 0.2% to 1.5%. Although these losses have relatively low values, the power loss in the meshing is particularly important for the overall efficiency of the planetary gear train, which has been validated in details in [22].

5. Analysis of research possibilities for planetary gear trains

The possibilities of theoretical and experimental research of planetary gear trains have been presented in a considerable number of publications. The most widely used experimental methods [23, 24] are based upon vibration diagnosis.

Modal analysis is an approach which is based on vibration theory. Its main objective is to obtain the inherent characteristics of the structural system, such as natural frequencies and natural modes.

Quite often the mode analysis is done applying ANSYS, [25 - 28]. A significant group of scientists investigates the modal properties of planetary gear trains, emphasizing the relationship between the natural frequencies and the parameters of the technical systems investigated.

Interesting experimental studies of planetary gear trains have been done by several groups of world-renowned scientists. The authors of [29] mainly focus on the modal frequencies of gears. The vibration modes of complex planetary gear drives have been studied by the authors of [30] and [31].

In [32], the elasticity effect of a ring with internal teeth of a planetary gear drive has been investigated. In [33], experimental modal analysis procedures have been applied in order to refine the dynamic behavior of planetary gear trains.

The most commonly used experimental instruments for investigating power transmission are accelerometers. The location of these devices in the planetary gear train is particularly important because the satellite gears create similar vibrations passing through the sensor assembled, [34].

6. Conclusion and future work

The theoretical research presented has been carried out in several main areas: design features of planetary gear trains, applied aspects of the usage of planetary gear drives in vehicles, possibilities of increasing the efficiency of planetary gear sets and analysis of option for researching the gear drives considered.

Based upon the theoretical research, the following conclusions can be drawn:

Significant scientific publications in the field of the application of planetary gears in vehicles, including hybrid and electric automobiles, have been reviewed.

Special attention is dedicated to the layout and application of new, specific design schemes of power transmission using planetary gear trains which allow minimizing the energy consumption. They can be useful for manufacturers and engineers by applying the appropriate design schemes and taking into account the relevant limitations and operating conditions of planetary gear drives.

It becomes clear that new possibilities for increasing the efficiency of planetary gear trains can still be found. This circumstance will also lead to decreasing the energy consumption in vehicles.

Analyzing the main options for research in the field of planetary gear drives, the author team considers that the future scientific work of the PhD student will be focused on improving the energy efficiency of planetary gear drives and determining methods to reduce vibration and noise in these gear trains.

Acknowledgements

This research was supported by the Fund of Scientific research at the University of Ruse, Bulgaria. The authors would like to express their acknowledgments to the University and Faculty management members.

References

1. EU transport in figures. Statistical pocketbook, https://data.europa.eu/doi/10.2832/27610, (2021)
2. G. Erbach. EPRS | European Parliamentary Research Service, Members' Research Service PE 698.920, (2022)
3. K. Arnaudov and D. Karaivanov. Planetary gear trains. CRC Press, *Boka Raton*, FL, USA, (2019)
4. M. Peneva, K. Radkova, S. Troha and D. Karaivanov. On the using of two-carrier planetary gear trains with two compound and four external shafts as change-gears. MATEC Web of Conferences **366**, 01007, doi.org/10.1051/matecconf/202236601007, (2022)
5. S. Milev. Kinematic and geometric synthesis of planetary gearboxes. Dissertation, University of Ruse "A. Kanchev", Bulgaria, (2019)
6. C. Rocha, L. Silva, J. Eckert, F. Dedini, M. Lourenço and F. Silva. Kinematic Analysis for planetary gearbox applied in Hybrid Electric Vehicles, Brazilian Society of Automotive Engineering - SIMEA 2021, pp 1-10, (2021)
7. D. Rajput, J. Herreros, M. Innocente, J. Schaub and A. Dizqah. Electrified Powertrain with Multiple Planetary Gears and Corresponding Energy Management Strategy. *Vehicles 2021*, **3**, 341–356,https://doi.org/10.3390/vehicles3030021, (2021)
8. S. Stoyanov, V. Dobrev and A. Dobreva. Finite Element Contact Modelling of Planetary Gear Trains. *Material Science and Engineering, IOP Publishing*, **252**, pp. 012034 - 38, doi: 10.1088/1757-899X/252/1/012034, (2017)
9. S. Stoyanov and A. Dobreva. Development, Design and Optimization of Planetary Gear Trains for Vehicles – Computer Aided Frequency Analysis of Planetary Gears. *VDI – Berichte* 2108.2, VDI Verlag GmbH – Duesseldorf, pp. 1423 – 1426, (2010)
10. A. Dobreva and V. Dobrev. Innovative Methodology for Decreasing Mechanical Losses in Vehicles. Proceedings of the 4th *International Congress of Automotive and Transport Engineering (AMMA 2018), Springer Verlag*, pp.234 – 242, doi:10.1007/978-3-319-94409-8_28, (2019)
11. M. Qiang and Z. Qinghua. Planetary Gear Box Vibration Signal Characteristics and Fault Diagnosis. *Hindawi Publishing* Corporation Shock and Vibration, Vol. 2015, Article ID 126489, pp. 1-8, http://dx.doi.org/10.1155/2015/126489, (2015)
12. V. Dobrev, S. Stoyanov and A. Dobreva. Numerical Investigation of Planetary Gear Trains and Transmissions. *Mech. and Machine Science/ 5th Int. Conf. on Power Transmission BAPT in Ohrid*, CIRKO dooel Skopje, pp. 155 - 162, (2016)
13. S. Stoyanov, V. Dobrev and A. Dobreva. Investigating Dynamic Behavior of Planetary Gear Trains through the Systematic Approach, *VDI Berichte*, 2, pp. 127 - 132, (2017)
14. S. Stoyanov, V. Dobrev and A. Dobreva. Investigation of the Opportunities for Experimental Research of Gear Trains Vibrations. MATEC Web of Conferences, No 287, pp. 1-5, doi:10.1051/matecconf/201928703001, (2019)
15. V. Dobrev, S. Stoyanov and A. Dobreva. Design, Simulation and Modal Dynamics of Gears and Transmissions, *VDI-Berichte* 2255, (**3**), pp 695 - 707, (2015)
16. S. Stoyanov. Explicit Dynamics of Gear Pair Using Finite Element Model, *Scient. Proc. of UoR*, **54**, pp 67-71, (2015)
17. D. Rajput, J. Herreros, M. Innocente, J. Schaub and A. Dizqah. Electrified Powertrain with Multiple Planetary Gears and Corresponding Energy Management Strategy. *Vehicles 2021*, **3**, 341–356,https://doi.org/10.3390/vehicles3030021, (2021)

18. H. Matsuki, K. Nagano and Y. Fujimoto. Bilateral Drive Gear - A Highly Backdrivable Reduction Gearbox for Robotic Actuators. *IEEE/ASME Transactions on Mechatronics*, Vol. 24, **6**, pp. 2661 - 2673, (2019)
19. M. Du and L. Yang. A basis for the computer-aided design of the topological structure of planetary gear trains. *Mechanism and Machine Theory*, **145** (2020) 103690.
20. C. Liu, X. Yin, Y. Liao, Y. Yi and D. Qin, D. Hybrid dynamic modeling and analysis of the electric vehicle planetary gear system. *Mechanism and Machine Theory*, **150** (2020) 103860.
21. V. Petrescu, R. Aversa, A. Apicella and T. Petrescu. About the gear efficiency to a simple planetary train. *American Journal of Applied Sciences*, 13 (**12**), pp. 1428–1436, (2016)
22. A. Dobreva and S. Stoyanov. Optimization Research of Gear Trains with Internal Meshing. *University Publishing Centre*, Ruse, pp. 144, (2012)
23. T. Lin, Z. He, F. Geng. Prediction and Experimental study on Structure and Radiation Noise of Subway Gearbox, *J. of Vibroeng*., 15 (**4**), pp. 1838 -1846, (2013)
24. Z. He, T. Lin, J. Song. Analytical Computational Method of Structure-borne Noise and Shock Resistance of Gear System, *J. of Measurement in Eng.*, 2 (**4**), pp. 215 - 224, (2014)
25. Z. Wang, T. Lin, Z. He, X. Yang. Vibration Characteristics Analysis of Vertical Mill Reducer. *In. Conf. on Automation, Mechanical Control and Computational Engineering, AMCCE*, (2015)
26. C. Korka, C. O. Miclosina, Shape Improvement of a Gearbox Housing Using Modal Analysis, *RJAV*, 15 (**1**), (2018)
27. S. Stoyanov. An experimental setup for determination of the resonant frequencies of a mechanical frame structure. *Fund. Sciences and Applications, Journal of the TU – Sofia*, Bulgaria, **24**, pp.67-71, (2018).
28. S. Stoyanov. Software tools for mechanical structures resonant frequencies determination: Vibration signal processing for modal analysis. *CompSysTech'18: Proceedings of the 19th International Conference on Computer Systems and Technologies*, pp. 120–123, https://doi.org/10.1145/3274005.3274037, (2018)
29. R. Tanna and T. Lim, Modal Frequency Deviations in Stimating Ring Gear Modes Using Smooth Ring Solutions, *J. of Sound and Vib*., **269**, pp. 1099-1110, (2004)
30. D. Kiracofe and R. Parker, Structured Vibration Modes of General Compound Planetary Gear Systems, *J. of Vib. and Acous*., **129**, pp 1-16, (2007)
31. Y. Guo and R. Parker. Purely Rotational Model and Vibration Modes of Compound Planetary Gears, *Mech. and Mach. Theory*, **45**, pp 365-377, (2010)
32. A. Kahraman and S. Vijayakar. Effect of Internal Gear Flexibility on the Quasi-static Behavior of a Planetary Gear Set, *J. of Mech. Design*, **123**, pp. 408-415, (2001)
33. T. Ericson and R. Parker. Planetary Gear Modal Vibration Experiments and Correlation against Lumped-parameter and Finite Element Models, J. *of Sound and Vib*., **332**, pp. 2350-2375, (2013)
34. N. Feki, M. Karray, M. Khabou, F. Chaari and M. Haddar. Frequency Analysis of a Two-stage Planetary Gearbox Using Two Different Methodologies. *Comptes Rendus - Mecanique*, 345 (**12**), pp. 832–843, (2017)

CFD simulation of airflow through the throttle body of the air intake system applied to the Formula Student vehicle

Marko Lučić
Faculty of Mechanical Engineering, University of Montenegro, Podgorica, Montenegro
E-mail: markol@ucg.ac.me

Abstract: *In this paper, a simulation of their flow through the throttle valve on the Formula Student vehicle was performed throttle valve is an element that, according to the regulations of the Formula Student competition, must be present in the intake installation of the vehicle's power unit if it is a competition in class IC. The correct design of the throttle is of great importance anchor or the power unit to work properly, but also to extract the maximum performance of the power unit itself, and thus of the competition vehicle as a whole. One of the main tasks of the throttle is to allow air to flow with as little resistance to flow as possible. For the CFD simulation in this work, ANSYS Fluent was used, which proved to be a very powerful tool in the CFD simulation of the throttle body.*
Keywords*: CFD, THROTTLE BODY, VEHICLE, IC ENGINES, FORMULA STUDENT*

1. Introduction

The Formula Student competition is getting more and more popular. This competition is very attractive because it provides students with a good springboard for employment in the automotive industry after graduation. The number of Formula Student teams is growing year by year. Students from universities around the world compete to design a small racing vehicle. The design of the air intake system together with the throttle body applied to Formula Student vehicles is a very current topic, as evidenced by a large number of articles on the mentioned topic [1-8]. This work is structured into six chapters. The first chapter is an introduction and this chapter outlines what is covered in each of the six chapters. The second chapter is related to the design of the throttle body and the limitations prescribed by the organizers of the Formula Student competition. The CFD analysis of the throttle body was performed in chapter three, while the results of the CFD analysis were presented in chapter four. Chapter 5 is the conclusion on the topic of the work itself, and chapter six lists the references used in the work.

2. Formula Student throttle body

2.1. Throttle body

In the Formula Student competition, the big challenge is designing the intake system for the engine. As the Formula Student competition uses engines that are installed on motorcycles, it is necessary to modify them. The main modifications relate to the adjustment of the intake and exhaust installation, the engine map, as well as the cooling system itself, and the fuel system. The possibility of changing some structural parts of the engine, such as modification of the engine pistons, and crankshaft, should also be considered. To consider the possibility of modifying the crankshaft, it is necessary to perform a dynamic analysis of the forces acting in the engine, which is preceded by a kinematic analysis. An example of kinematic analysis is given in Ref. [9] in which this analysis can be done very easily using CATIA software.

Electronic Fuel Injection (EFI) is an active system that adjusts fuel delivery for the internal combustion engine, and the carburetor is a passive system that controls the intake of the fuel and air mixture. Fuel delivery to the engine is managed by the engine control unit (ECU), which precisely controls the duration and time of fuel delivery through fuel injectors. It can be said that the throttle body is an air valve. The throttle body has the task of allowing air to enter the engine. The more air delivered in combination with the appropriate amount of fuel, the more power is obtained from the engine, theoretically. This would mean that the use of a larger diameter throttle body also means a larger amount of airflow, which is not always the best move. The diameter of the throttle body must be of the appropriate size according to the volume of the engine. If the throttle body diameter is too large, the air velocity is slow, but more air is sucked into the engine, while if the diameter is too small, the air velocity is faster, but not enough air can pass. If a forced-induction system is used, the diameter of the throttle body becomes less critical because the turbocharger or supercharger pushes air into the engine. A smaller throttle body can be used in a turbo setup because the air pressure and air density are approximately twice as high as in a naturally aspirated engine [10]. Figure 1 shows the barrel throttle body concept, which is very often used on Formula Student vehicles.

Fig. 1 *Barrel Throttle Valve [11]*

2.2. Throttle body restriction

Restrictions for the throttle body are given in the Formula Student Rulebook [12]. This regulation defines that the vehicle must be equipped with a throttle body, which can be of any size or design. The throttle must be activated by a mechanical foot pedal or rod system. Throttle position is defined as the percentage of time from fully closed 0% to open 100%. The mechanism of the throttle system must be protected from debris penetration to prevent jamming. Rulebook [12] defines two intake system configurations for naturally aspirated engines (Figure 2) and turbocharged or supercharged engines (Figure 3). Depending on which type of configuration is chosen, the position of the throttle body in the air intake system will also be defined. It is important to emphasize that in the case of using a turbocharged or supercharged configuration, a throttle body with a smaller diameter can be used compared to a configuration with naturally aspirated engines.

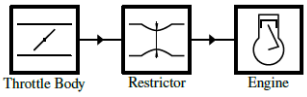

Fig 2. *Configuration for naturally aspirated engines [12]*

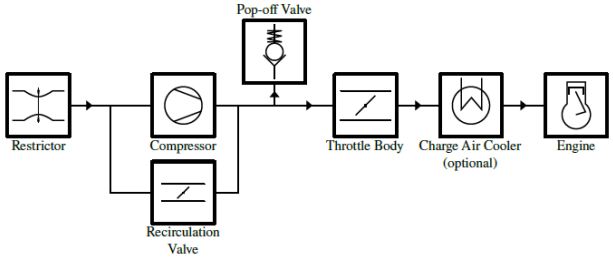

Fig 3. *Configuration for turbocharged or supercharged engines [12]*

3. CFD simulations of the throttle body

In this chapter, a CFD simulation of two throttle bodies was performed to see how the small geometrical difference between them affects the airflow. Figures 4 and 5 show two throttle bodies that were considered during the CFD simulation. Throttle body 2D geometries are shown in Figures 4 and 5. CFD simulation was performed for both throttle bodies at three characteristic positions, i.e. for positions of 50%, 75%, and 100% open throttle body. In Ansys Design Modeler

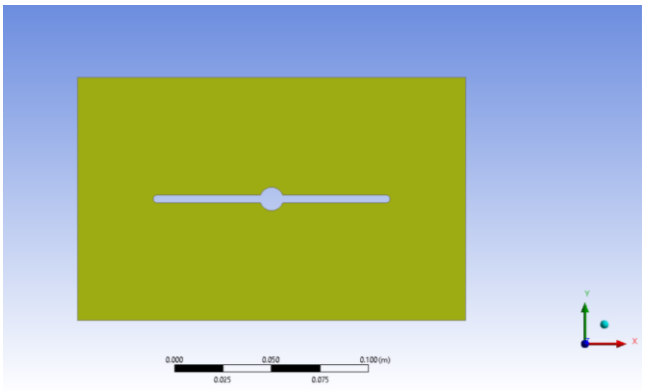

Fig 4. *Throttle body (concept) A*

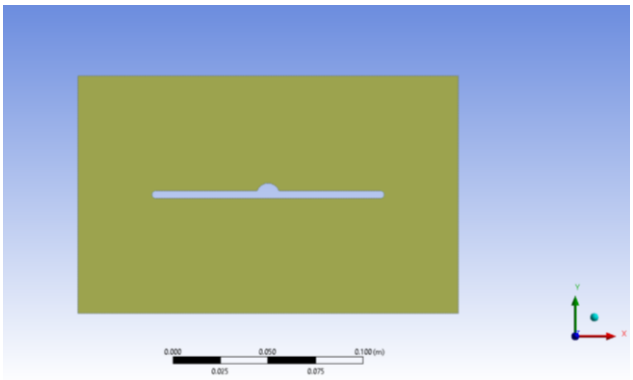

Fig. 5 *Throttle (body concept) B*

After generating the 2D geometry of the fluid domain, a mesh was generated for both types of the throttle body, which is shown in Figures 6 to 11. The first throttle body concept is labeled A and the numbers on the label indicate the position over the opening percentage, so we have A(100%), A(75%), and A(50%), where the percentages represent the position of 100%, 75%, 50% opening of the throttle body. It should be noted that 100% is a fully open throttle body and 0% is a fully closed throttle body. The same applies to concept B, so numerous values indicate the percentage of throttle body openness.

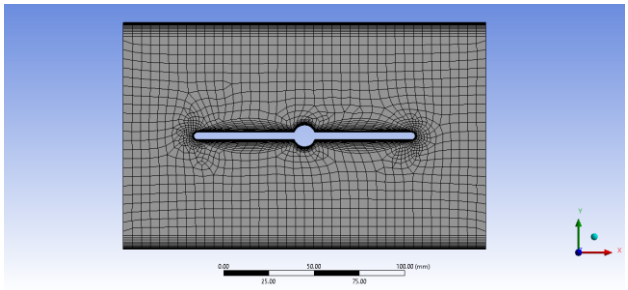

Fig. 6 *Mesh for Throttle body A(100%)*

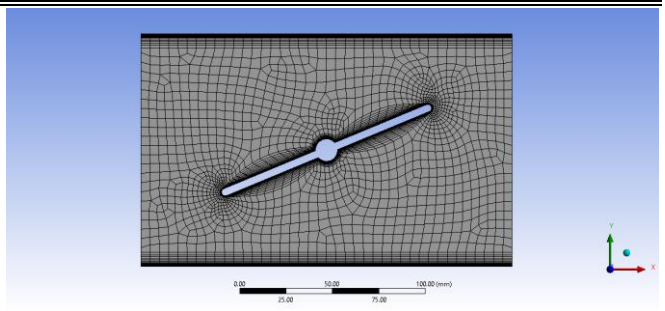

Fig. 7 *Mesh for Throttle body A(75%)*

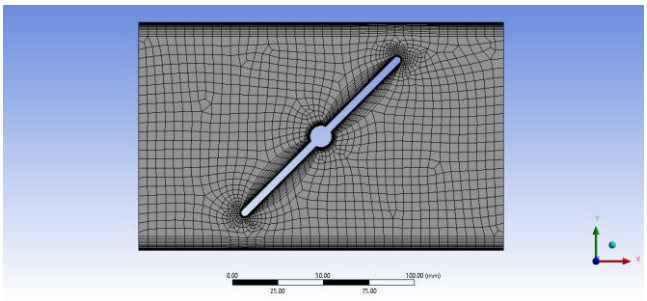

Fig. 8 *Mesh for Throttle body A(50%)*

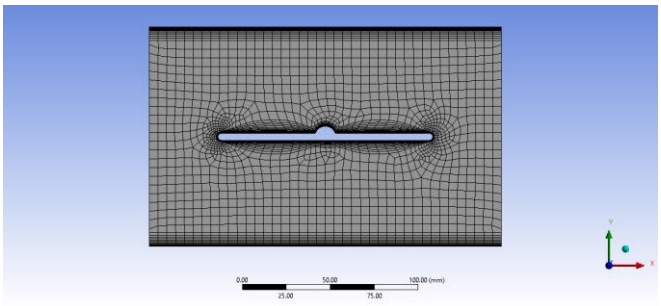

Fig. 9 *Mesh for Throttle body B(100%)*

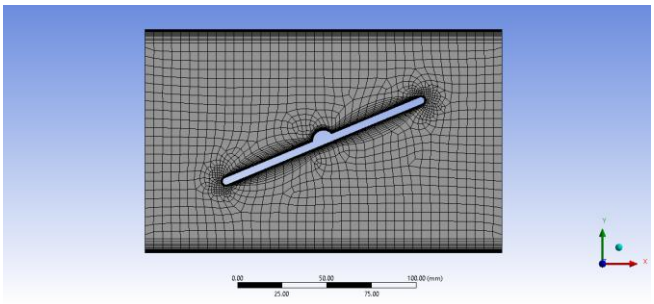

Fig. 10 *Mesh for Throttle body (B75%)*

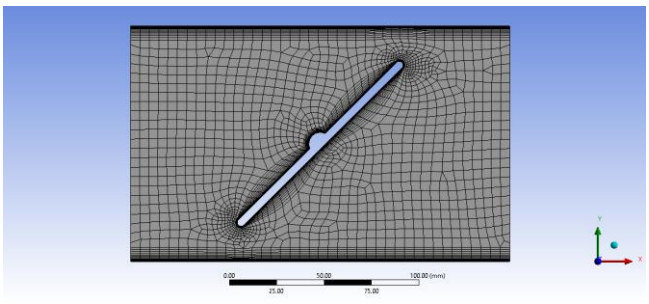

Fig. 11 *Mesh for Throttle body B(50%)*

Setting up the CFD simulation is what follows after generating the mesh. The standard k-epsilon turbulence model was used in the CFD simulation. After setting up the network, it is necessary to set

the boundary conditions. Air was used as the fluid, and the pressure drop at the outlet compared to the inlet was simulated by 0.1 bar. A pressure of 1 bar was set at the inlet and 0.9 bar at the outlet. For each throttle body out of the three possible cases, it is necessary to define the inlet and outlet of the working fluid, and this is shown only in the example of a 100% throttle body for concepts A and B, in Figures 12 and 13 with the network (inlet - blue arrows, outlet red arrows).

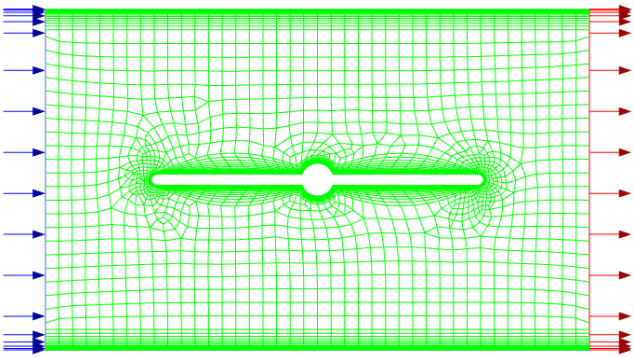

Fig. 12 *Inlet and outlet for 100% open Throttle body A*

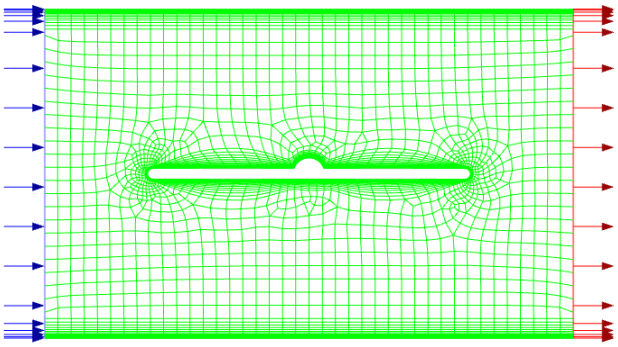

Fig. 13 *Inlet and outlet for 100% open Throttle body B*

4. Results

The results of CFD simulations of airflow through both throttle bodies A and B for three different opening positions are given in this chapter. Figures 14 to 19 show the contour of pressure for Throttle Body A and B for three positions.

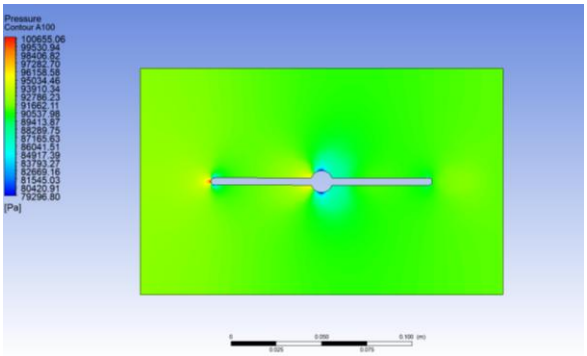

Fig. 14 *Pressure contour for Throttle body A(100%)*

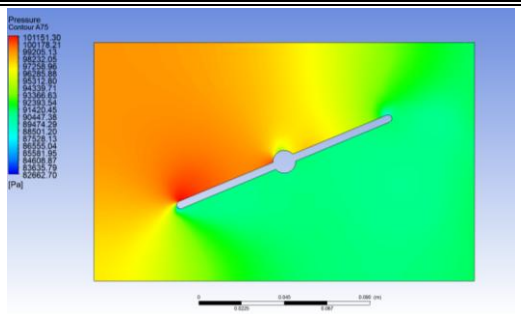

Fig. 15 *Pressure contour for Throttle body A(75%)*

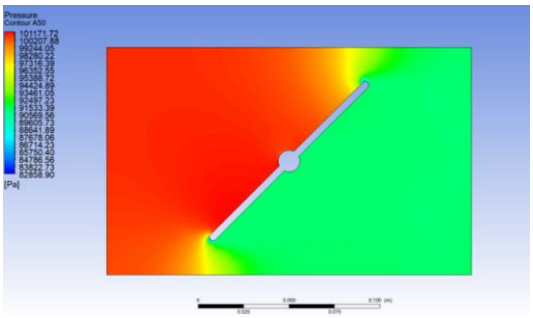

Fig. 16 *Pressure contour for Throttle body A(50%)*

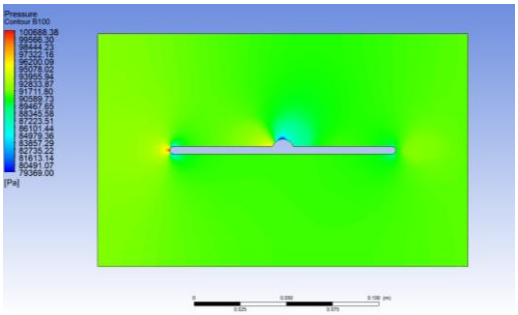

Fig. 17 *Pressure contour for Throttle body B(100%)*

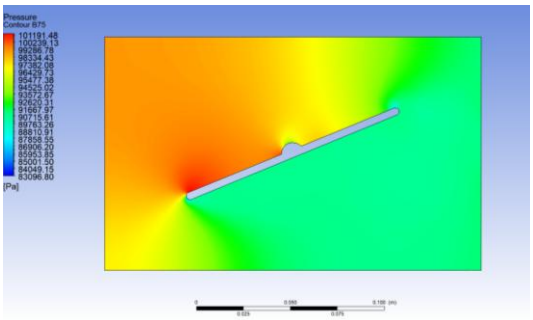

Fig. 18 *Pressure contour for Throttle body B(75%)*

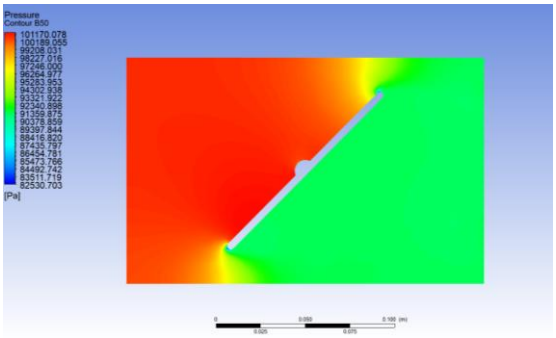

Fig. 19 *Pressure contour for Throttle body A(50%)*

Velocity contours for both throttle bodies and all three considered opening positions are also shown in this chapter. Figures 20 to 25 show velocity contours for the throttle body and opening positions.

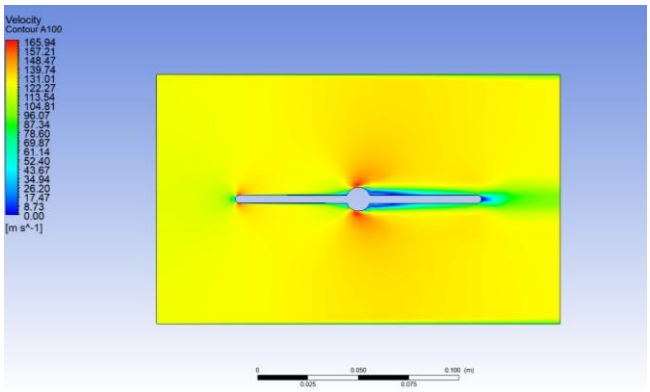

Fig. 20 *Velocity contour for Throttle body A(100%)*

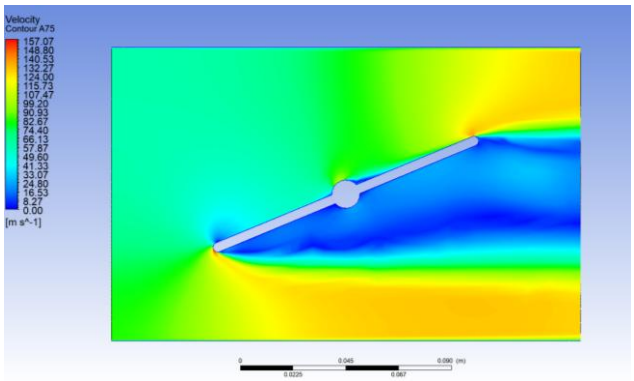

Fig. 21 *Velocity contour for Throttle body A(75%)*

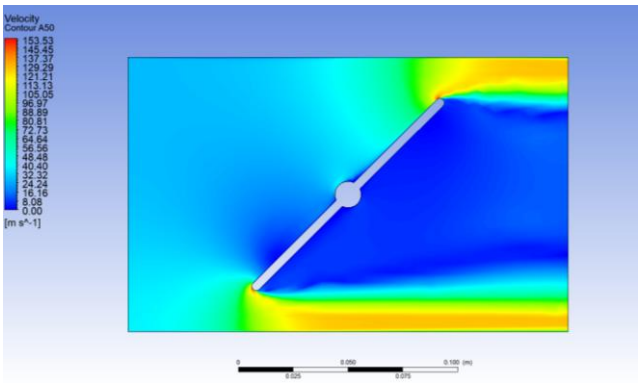

Fig. 22 *Velocity contour for Throttle body A(50%)*

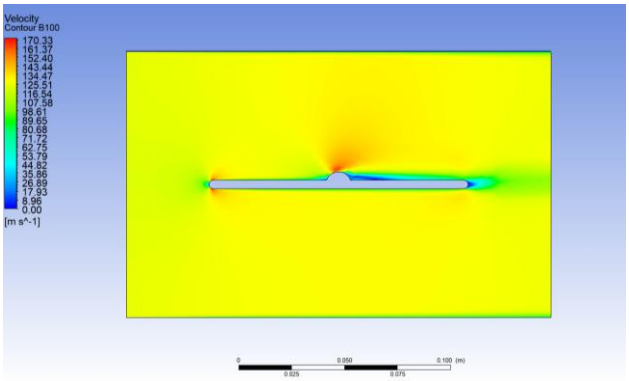

Fig. 23 *Velocity contour for Throttle body B(100%)*

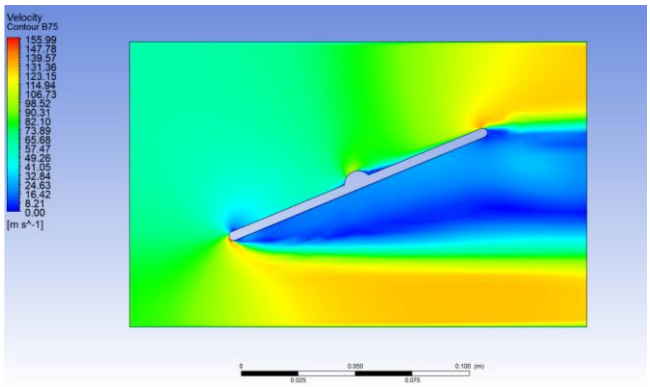

Fig. 24 *Velocity contour for Throttle body B(75%)*

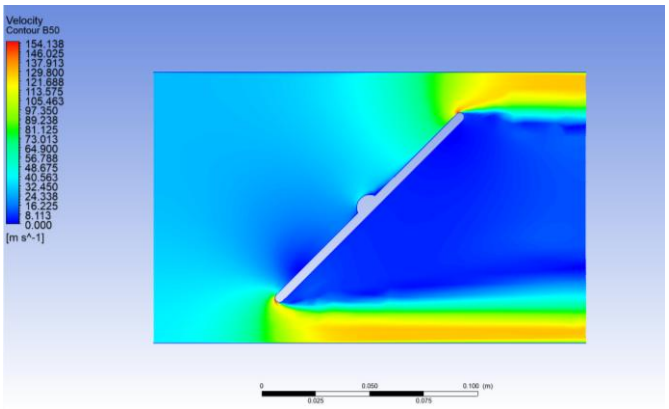

Fig. 25 *Velocity contour for Throttle body B(50%)*

For an easier overview of the results related to max velocity, a diagram is given in Figure 26.

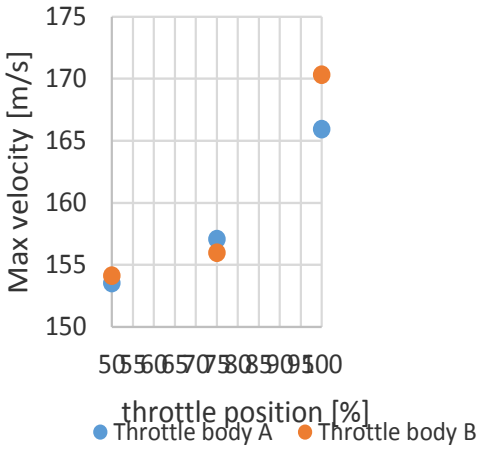

Fig. 26 *Maximum velocity in the throttle body*

From the previous analysis, it can be concluded that these two throttle bodies are very similar geometrically, and practically similar in results as well. Throttle body B has a higher maximum speed value at full opening (100%). which is logical because it has a smaller surface that creates an obstacle to airflow. A slightly higher maximum speed is achieved by throttle body B even at 50% opening, while at 75% opening the maximum speed is higher with throttle body A.

5. Conclusion

CFD simulation is a standard part of serious engineering practical analysis not only in the automotive industry but also in all other industries dealing with fluids. In the paper itself, it was shown that even if the design of the throttle body is slightly different, the results can differ to a great extent. In this case, it is shown in the example of velocity and pressure at the full opening of throttle body A and B. Investigating the fluid flow in the throttle body can be a very complex job, especially if the considered problem is examined in detail. It has been shown that very simple CFD simulations can simulate the real situation in the example of the throttle body. In the end, it should be emphasized that the biggest influence on the flow is the throttle body's diameter. Special attention should be paid to the correct dimensioning of the throttle body, but also to the shape itself, as well as to the choice of material from which it will be produced. As Formula Student teams are limited by budget, the vast majority decide to make their throttle body design, so CFD simulation can be of great help in choosing a better design.

6. References

1. Ranganathan, S., Thiyagarajan, A. S., Kuppuraj, S., & Chandrasakaran, P. (2019). *Design and Analysis of De-Lavel Restrictor with Throttle Body for Formula Vehicle* (No. 2019-28-0009).
2. Lindley, D. (2012). Design and Optimization of a Throttle and Restrictor for Formula SAE (Doctoral dissertation, University of Cincinnati).
3. Sharma, V., Dhauni, S., & Chawla, V. K. (2021). Design and manufacturing of air intake assembly for formula SAE vehicle. Materials Today: Proceedings, 43, 58-64.
4. Waghmare, S. N., Karekar, N. S., Karande, P. P., & Pandhare, S. B. (2016). Design & Analysis for Intake System of Formula SAE Car. International journal of Engineering technology, Management and applied sciences, 4(2), 2349-4476.
5. Jose, J., Shetty, N., Dhumal, A., Anthony, H., & Kushwaha, A. (2018). CFD Analysis of Air Intake Manifold System to Improve Efficiency of Formula SAE Car.
6. Mohamad, B., Karoly, J., & Zelentsov, A. (2020). CFD modelling of formula student car intake system. Facta Universitatis. Series: Mechanical Engineering, 18(1), 153-163.
7. Bhope, A., Huwale, S., Aher, V., Dahiwal, R., & Patil, M. N. (2020). DESIGN AND ANALYSIS OF INTAKE SYSTEM FOR FSAE VEHICLE.
8. Xu, C., & Cho, H. (2017). The Analysis of Influence of Throttle Body on Engine Intake System. International Journal of Engineering and Technology (IJET).
9. Lučić, M. (2022). Kinematic analysis of the slider-crank mechanism of an internal combustion (IC) engine using modern software. Mechanization in agriculture & Conserving of the resources, 68(1), 11-17.
10. Mike, Narvigia. (2014). Performance Exhaust Systems: How to Design, Fabricate, and Install. CarTech, ISBN 978-1-61325-207-9
11. Harty, R. T. (2017). The Design and Testing of a High Performance Formula SAE Powertrain.
12. Formula Student Rules. (2022). SAE

Design and CFD simulation of the exhaust manifold of the Formula Student vehicle

Marko Lučić
Faculty of Mechanical Engineering, University of Montenegro, Podgorica, Montenegro
E-mail: markol@ucg.ac.me

Abstract: *One of the biggest challenges in the FSAE competition is adapting the power unit to the strict regulations of the competition. The task of the exhaust manifold is to enable the best possible flow of exhaust gases from the engine to the environment. A properly designed vehicle exhaust manifold is of great importance for enabling better performance of the power unit. There are several different concepts for designing exhaust manifolds. Each concept has its advantages and disadvantages. One of the main guidelines when designing the exhaust manifold is to enable air flow with as little local resistance as possible so that the exhaust gases are released into the environment as soon as possible. In this work, a 3D model of three types of exhaust manifolds was created, and then a CFD simulation of airflow through exhaust manifolds was performed using ANSYS Fluent software. CFD simulations help to a great extent with a better design of the exhaust manifold.*
Keywords*: CFD, EXHAUST MANIFOLD, VEHICLE, IC ENGINES, FORMULA STUDENT*

1. Introduction

The design of the exhaust manifold is one of the biggest challenges when designing a Formula Student vehicle, as evidenced by a large number of scientific works on the mentioned topic [1-6]. Ref. [7] showed that with a proper design of the exhaust manifold, the exhaust emission can be reduced. In this paper, a CFD analysis of several different models of the exhaust manifold was performed. In the first chapter, what was done in the work itself was defined. The second chapter deals with the Formula Student rulebook with special reference to the part of the rulebook related to the driving system of the vehicle. The third chapter talks about exhaust manifolds in general. A CFD analysis of various Exhaust System concepts is presented in chapter four. In chapter five, the results of CFD analyzes of different concepts of exhaust branches are presented, while in chapter six, a conclusion related to the topic of the paper is given. Chapter seven lists the literature used in this paper.

2. Exhaust design limitations for a Formula Student vehicle

As the topic of this paper is the CFD analysis of the exhaust manifold of the engine used in the Formula Student competition, this chapter will talk about the competition itself. Formula Student or formerly "Formula SAE" (FSAE) is the most complex, demanding, and attractive student engineering competition in the world organized by the Society of Automotive Engineers (SAE). One of the biggest challenges of the Formula Student competition is the design of the exhaust system. The restrictions related to the internal combustion engine are shown in the Formula Student Rules [8]. By this regulation, the internal combustion engine that powers the FSAE vehicle is limited to a four-stroke, internal combustion piston engine with a volume of no more than 710 cm^3 per cycle. Given the previously mentioned limitation, the choice of internal combustion engines is limited to those that are usually installed in racing motorcycles. Another major limitation of the internal combustion engine that applies is related to the air intake. Rulebook [8] stipulates that all air sucked into the engine must pass through the restrictor. The maximum restrictor diameters which must be respected at all times during the competition are 20 mm for gasoline-fueled vehicles or 19 mm for E 85-fueled vehicles. The exhaust opening must be directed to the side or rear of the vehicle so that the driver is not exposed to the fumes at any speed given the vehicle's ground clearance. The exhaust port(s) must not extend more than 450 mm beyond the center line of the rear axle and must not be more than 600 mm above the ground. All exhaust components (headers, mufflers, etc.) protruding from the side of the body in front of the main hoop must be protected to prevent contact by persons approaching the vehicle or the driver exiting the vehicle. The temperature of the outer surface must not be harmful to the person touching it. The maximum sound level test speed for a given engine will be the engine speed that corresponds to an average piston speed of 15.25 m/s. The calculated speed will be rounded to the nearest 500 rpm. The maximum permitted sound level up to this calculated speed is 110 dB(C), fast weighing. The exhaust manifold used on racing motorcycle engines must be changed and another must be designed and manufactured that will be more suitable for use on a four-wheeled vehicle. When choosing an internal combustion engine to be used, it is necessary to carry out detailed analyses, primarily about the number of cylinders, but also other analyzes related to construction parameters. Analysis of the kinematics of a four-cylinder engine with internal combustion using CATIA software is presented in the paper [9].

3. Exhaust manifolds and exhaust headers

The exhaust manifold is somewhat similar to the intake manifold. The intake manifold receives incoming air from a central point, be it the throttle body or carburetor. Using the intake manifold, the air is distributed to the individual cylinders. The exhaust manifold allows the exhaust gases of individual cylinders to exit the cylinder head immediately into a single collection path or chamber. An exhaust manifold is not the most efficient design solution, but it is the simplest, most direct, and cheapest solution for ejecting exhaust gases from the engine. In the automotive industry, exhaust manifolds were made of cast iron for decades because they were cheaper to produce, but also because of their compact size compared to steel tubular exhaust manifolds. The major disadvantages of cast-iron exhaust manifolds are almost no tuning potential for internal combustion engines. Tubular structures that required assembly and welding have been avoided for years. There were rare cases where exhaust manifolds were made from steel pipes that were joined into a single outlet pipe. Tubular exhaust manifolds offer the possibility of better engine customization and have great potential for extracting additional power and torque, while cast-iron exhaust manifolds have significant design limitations. The positive side of cast-iron exhaust manifolds is that they are made from one piece, require less proctor in the vehicle, and are usually significantly thicker, so they better insulate the noise and temperatures of the exhaust gases of internal combustion engines. Cast-iron exhaust manifolds due to very sharp curves can cause a bottleneck effect which can have a very unfavorable effect on the engine. Tubular headers have a weight advantage over cast-iron manifolds. The single most important advantage is that tubular exhaust headers can increase the power and torque of the engine. Tubular headers are available in several configurations. Tubular headers with different tube lengths are used for simpler and easier installation. Tubular headers with the same pipe lengths provide a significant advantage in terms of more efficient balancing of exhaust flow and pressure. Tubular headers are made with significantly less sharp corners of the pipes in contrast to cast-iron manifolds and thus allow better flows. The big disadvantage of tubular headers is the very high price, especially if they are made of stainless steel. This cost can be very justified if you consider the performance advantage over manifolds. Depending on the specific vehicle, the installation of tubular headers represents an additional challenge due to the space limitations of where it should be placed. Also, the disadvantage of tubular headers about manifolds is the tendency to create more noise due to the wear of smaller pipes [10].

4. CFD simulation

In this paper, CFD analysis of several different models of the exhaust system for the internal combustion engine used to drive the Formula Student vehicle was performed. The geometry of the exhaust systems analyzed in this paper corresponds to the engine that is installed in the motorcycle of the Japanese manufacturer Yamaha, trademark YZF-R6. Figures 1 to 3 show the models analyzed in this paper. 3D models of exhaust systems were created in Solid Works software. CFD analysis of exhaust systems was done in ANSYS Fluent software. Exhaust manifolds analyzed in this paper are marked with the marks A, B, and C. Manifold A has equal lengths of cylindrical pipes that connect to the main pipe under the same radius (Figure 1). Exhaust manifold B has different lengths of cylinder pipes that join the main pipe at the same radius (Figure 2). Manifold C represents a classic exhaust manifold design (Figure 3).

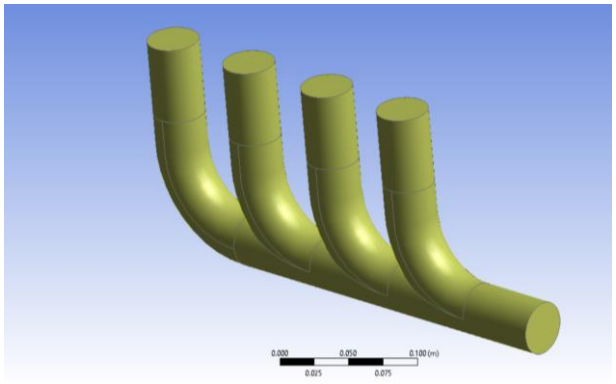

Fig. 1 *Exhaust manifold A*

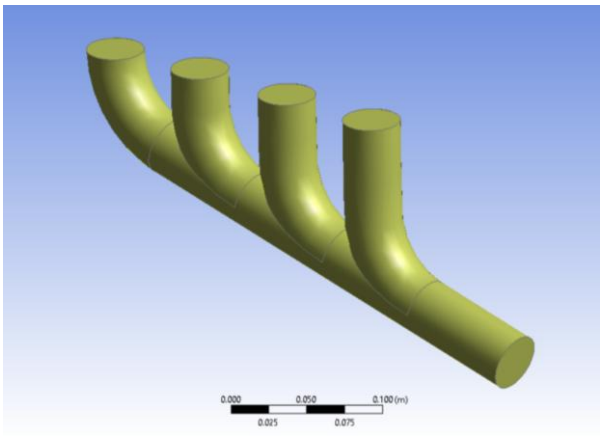

Fig. 2 *Exhaust manifold B*

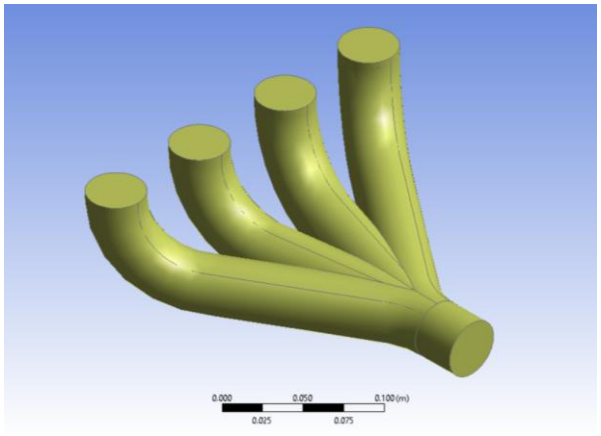

Fig. 3 *Exhaust manifold C*

After generating the fluid domain, a mesh was created for each of the models. The appearance of the created network is shown in Figures 4 to 6. Setting up the network for models during CFD simulation is a very demanding and complex job.

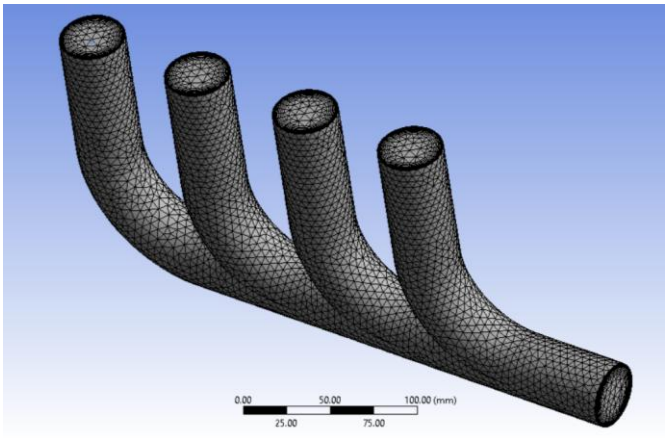

Fig. 4 *Mesh for Exhaust Manifold A*

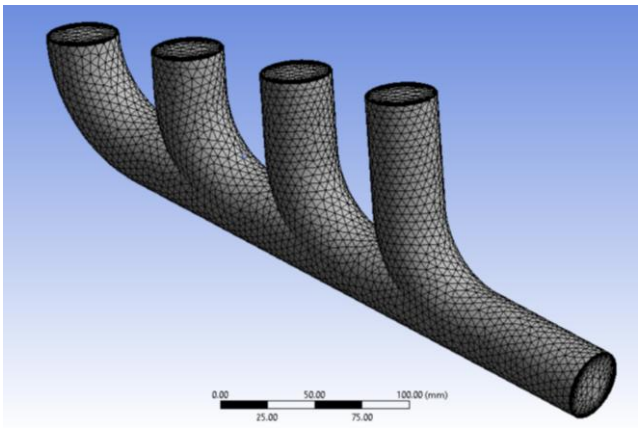

Fig. 5 *Mesh for Exhaust Manifold B*

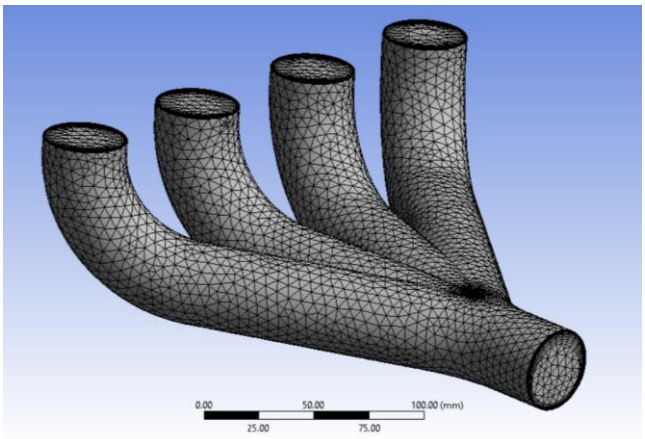

Fig. 6 *Mesh for Exhaust Manifold C*

After creating the network for the generated models of exhaust manifolds, it is necessary to set up the CFD simulation. For the CFD simulation, the standard k-epsilon turbulence model with standard constants was used: Cmu=0.09, C1-Epsilon=1.44, C2-epsilon=1.92, TKE Prandtl Number=,1 and TDE Prandtl Number=1.3. Enhanced wall treatment with pressure gradient effects was also used. Material fluid properties are shown in Table 1.

Table 1: *Material fluid properties*

Material	Gasoline-vapor C8H18
Density [kg/m^3]	1.0
Viscosity [kg/m s]	1.72 x 10^{-5}
Thermal Conductivity [W/m K]	0.0454

After defining the material, boundary conditions were defined. Boundary conditions are set so that at the entrance to the exhaust manifolds we have a velocity magnitude of 30 m/s and that the temperature at the inlet is 700 K. As it is a four-cylinder engine, each of the considered exhaust manifolds has 4 inlets and one outlet. The inlets and outlets for each of the exhaust manifolds are shown in Figures 7, 8, and 9.

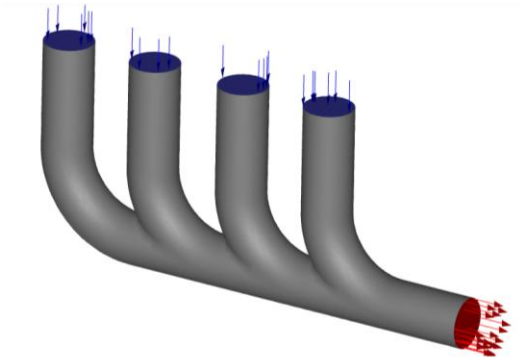

Fig. 7 *Inlets and outlet for Exhaust manifold A*

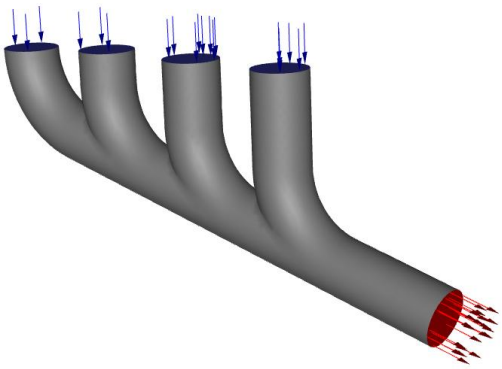

Fig. 8 *Inlets and outlet for Exhaust manifold B*

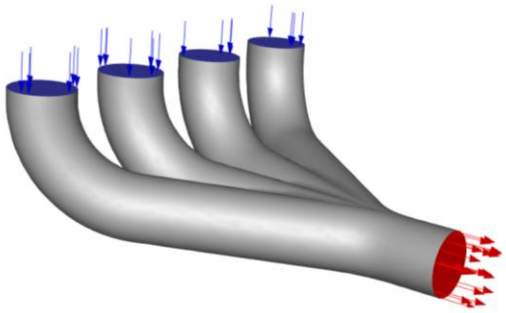

Fig. 9 *Inlets and outlet for Exhaust manifold C*

5. CFD simulation results

In this chapter, the results of the CFD analysis of the three types of exhaust manifolds that were considered (Exhaustmanifoldsd A, B, and C) are given. Figures 10 to 12 show pressure contours for the considered exhaust manifolds in this paper.

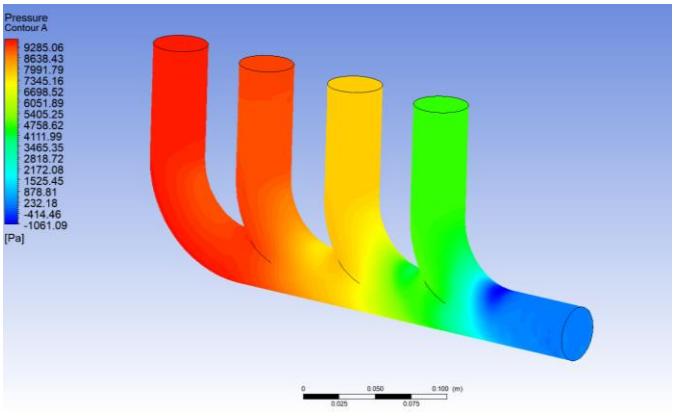

Fig. 10 *Pressure contour for Exhaust manifold A*

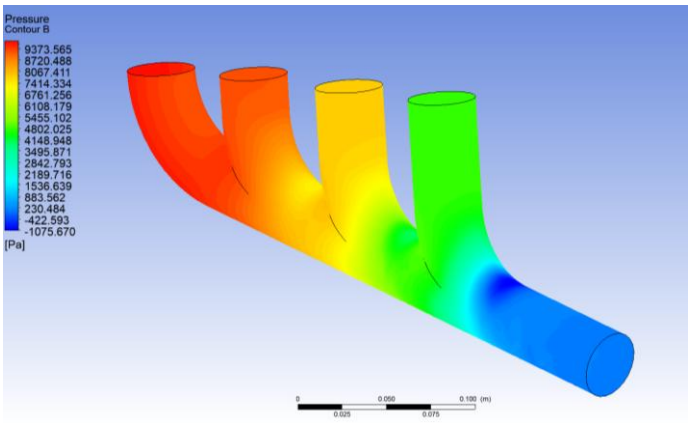

Fig. 11 *Pressure contour for Exhaust manifold B*

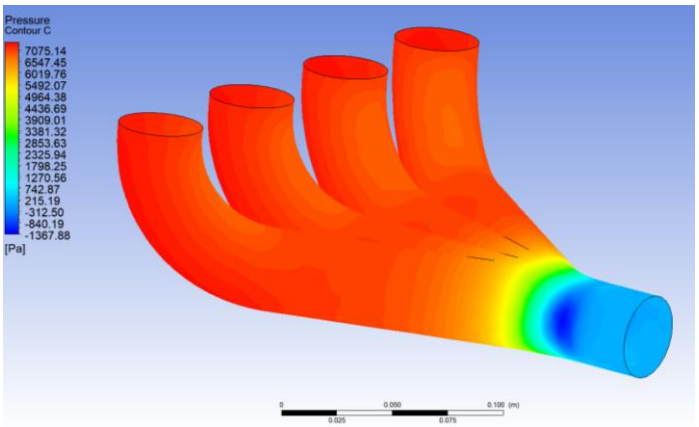

Fig. 12 *Pressure contour for Exhaust manifold C*

Figures 13 to 15 show the velocity streamlines for the considered exhaust manifolds.

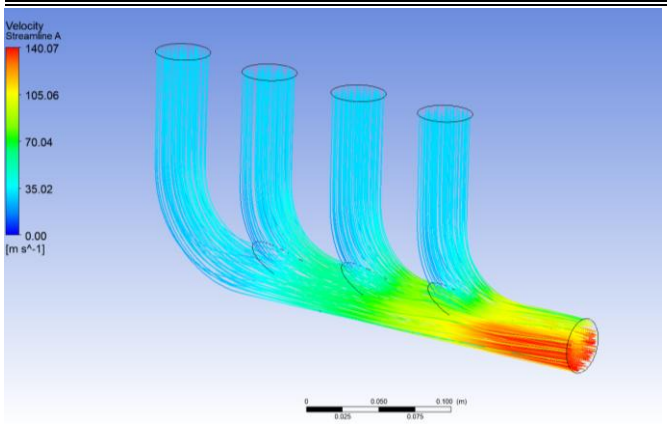

Fig. 13 *Velocity streamlines for Exhaust manifold A*

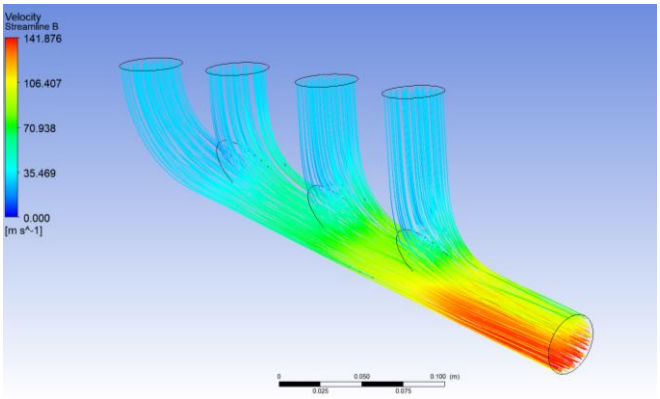

Fig. 14 *Velocity streamlines for Exhaust Manifold B*

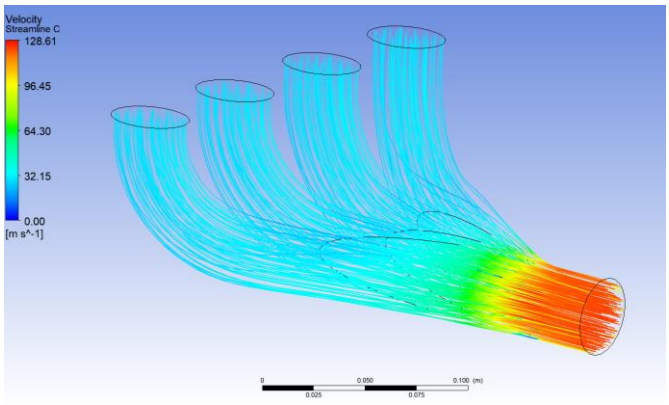

Fig. 15 *Velocity streamlines for Exhaust Manifold C*

From the previous pictures it can be seen that the results for exhaust manifolds A and B are very similar. Otherwise, these two exhaust manifolds are similar in terms of geometry, with the difference that Exhaust manifold B has pipes of different lengths that connect to the main pipe. Exhaust manifold A has a geometrically simpler construction, that is, the pipes used to distribute exhaust gas from the cylinders to the main pipe are of the same length. For these two exhaust manifolds, the pressure and flow velocity differ very little. Exhaust manifold C has significantly different results compared to the previous two. To better understand the results of the CFD analysis, the values of maximum pressure and maximum velocity for all exhaust manifolds that were considered are shown in Table 2.

Table 2: *Max values of pressure and velocity for Exhaust manifolds A, B, and C*

	Max pressure [Pa]	Max velocity [m/s]
Manifold A	9285.06	140.07
Manifold B	9373.58	141.87
Manifold C	7075.14	128.61

6. Conclusion

CFD simulations of airflow through the Exhaust manifold are of great importance because they make huge savings during the development of the system itself. CFD simulations have proven to be a very powerful tool when simulating the most realistic conditions in which the corresponding element or system being analyzed can work. These simulations can provide very important information related to the development of the exhaust manifold itself. CFD simulations of three types of exhaust manifolds were performed in the paper as a potential design solution for exhaust manifolds of Formula Student vehicles. When choosing the appropriate exhaust manifold concept, it is necessary to take into account some other parameters. One very important parameter is the production of the exhaust manifold itself, as well as the production costs. Exhaust manifold C is much more complex to manufacture compared to Exhaust manifolds A and B because it requires much more precise pipe-cutting and welding technology. Almost negligible differences in the CFD analysis results occur with Exhaust manifolds A and B because they are geometrically very similar.

7. References

1. Mohamad, B., Ali, M. Q., Neamah, H. A., Zelentsov, A., & Amroune, S. (2020). Fluid dynamic and acoustic optimization methodology of a formula-student race car engine exhaust system using multilevel numerical CFD models. *Diagnostyka*, *21*.
2. Yamamoto, S., Matsumoto, S., Ueda, T., Kodama, T., Honda, Y., & Wakabayashi, K. (2007). *A Study on Intake and Exhaust System of Turbocharged Engine under the Regulations of Formula SAE* (No. 2007-32-0113). SAE Technical Paper. 36-39.
3. Narang, H., Sharma, K., Mehta, D., Sheth, S., Bhanderi, S., & Patel, A. Design and Fabrication of Exhaust System of Formula Student Car
4. Mohamad, B. A. (2021). *Modelling and testing of advanced intake and exhaust system components for race car engines* (Doctoral dissertation, University of Miskolc).
5. Teja, M. A., Ayyappa, K., Katam, S., & Anusha, P. (2016). Analysis of exhaust manifold using computational fluid dynamics. *Fluid Mech Open Acc*, *3*(1), 1000129.
6. Umesh, K. S., & Rajagopal, V. P. K. (2013). CFD Analysis of Exhaust Manifold of Multi-Cylinder Si Engine Todetermine Optimal Geometry for Reducing Emissions. *International Journal of Automobile Engineering Research and Development*, 45-56.
7. Formula Student Rules. (2022). *SAE*
8. Lučić, M. (2022). Kinematic analysis of the slider-crank mechanism of an internal combustion (IC) engine using modern software. *Mechanization in agriculture & Conserving of the resources*, *68*(1), 11-17.
9. Mike, Narvigia. (2014). Performance Exhaust Systems: How to Design, Fabricate, and Install. *CarTech*, ISBN 978-1-61325-207-9

Assessment of machines in reliability test

Miho. Mihov[1], Davchev[2], G. Tasev[3]
Institute of Soil Science, Agro-Technology and Plant Protection "Nikola Pushkarov", Sofia, Bulgaria[1]
University of St. Cyril and Methodius "- Skopje, Northern Macedonia[2]
PhD - University of Forestry, Sofia, Bulgaria[3]
m.mihov@abv.bg; *gtassev* @abv.bg ; davcevz@gmail.com

Summary: *The necessity of using the apparatus of mathematical statistics to obtain high reliability of the results of the evaluation of the reliability indicators of agricultural machinery in comparative tests is justified.*
Two models of plant protection machines have been tested and the main numerical characteristics of the indicator production till failure of the failure-free feature have been obtained.
The application of the Student's criterion for proving the statistical significance of the difference in the tested reliability indicator is justified.
Keywords*: machines, testing methodology, agricultural machinery, parameters, criteria, test plan, numerical characteristics, reliability, refusal*

When testing agricultural machinery for reliability, as well as for determining all quantitative and qualitative parameters, it is necessary to use the mathematical statistics apparatus. It is best suited for making science-based decisions when determining the best machine or machine model for a given parameter. For a reliable estimate, it is not sufficient to use only the estimate of the average value of the test parameter, since the parameter is a random variable. Statistical criteria should be used to determine the significance of the difference in the mean scores. There are two sets of criteria for proving the statistical significance of the difference: parametric and non-parametric criteria. The most applicable of the group of parametric criteria is the Student's criterion, and the group of nonparametric criteria is the Man-Whitney criterion, [2-5].

The purpose of the study is to compare two models of plant protection machines against the failure free operation of reliability indicator.
The test is carried out in accordance with the experimental testing methodology [1] according to the plan [N =! RT], where R-means a plan in which the failed objects are replaced with new or repaired ones, and the T-test is carried out until the moment T.
We choose this test plan because we cannot test a large number of sites. At one site / N = 1 / we perform the test up to the moment T / the determined number of hours or area / and when a failure is detected in the machine, it is removed and the test continues until the next failure and so until the moment T occurs.
Two models of plant protection machinery from different manufacturers are subject to testing, and the results of the reliability test are given in Table 1.

Table 1. *Numerical characteristics of the production-to-failure indicator of two models of plant protection machines*

Dependencies for determining numerical characteristics	plant protection machines	
	Brand/ Model 1	Brand/ Model 2
$\vec{X} = \sum_{i=1}^{n} X_i$	$\vec{X}_1 =$ 45,1 h	$\vec{X}_2 =$ 62,8 h
$S = \sqrt{\sum_{i=1}^{n} (X_i - \vec{X}) \Big/ (n-1)}$	$S_1 =$ 19,8 h	$S_2 =$ 25,4 h
n	$n_1 =$ 36	$n_2 =$ 36

Означения*:* $\vec{X}$ *– estimation of the average value of the measured parameter of the machine;* X_i *– the* i *th value of the parameter;* S_i *– estimation of the root mean square deviation of the machine parameter values;* n *– the number of machines tested or the measured values of the measured parameter of the machine.*

As a result of the testing of the two models of plant protection machines, we find that the production up to failure of model 2 is higher than that of model 1. Only on this numerical characteristic of the measured indicator of the reliability of the machines / production up to failure / cannot to decide: which of the two models of plant protection machines has a higher level of trouble-free operation. Therefore, we also determine the numerical characteristic - standard deviation and apply the Student's criterion for proving the statistical significance of the differences in the values of the average production up to failure of the two models of plant protection machines. Therefore, we are in the situation shown in Figure 1.

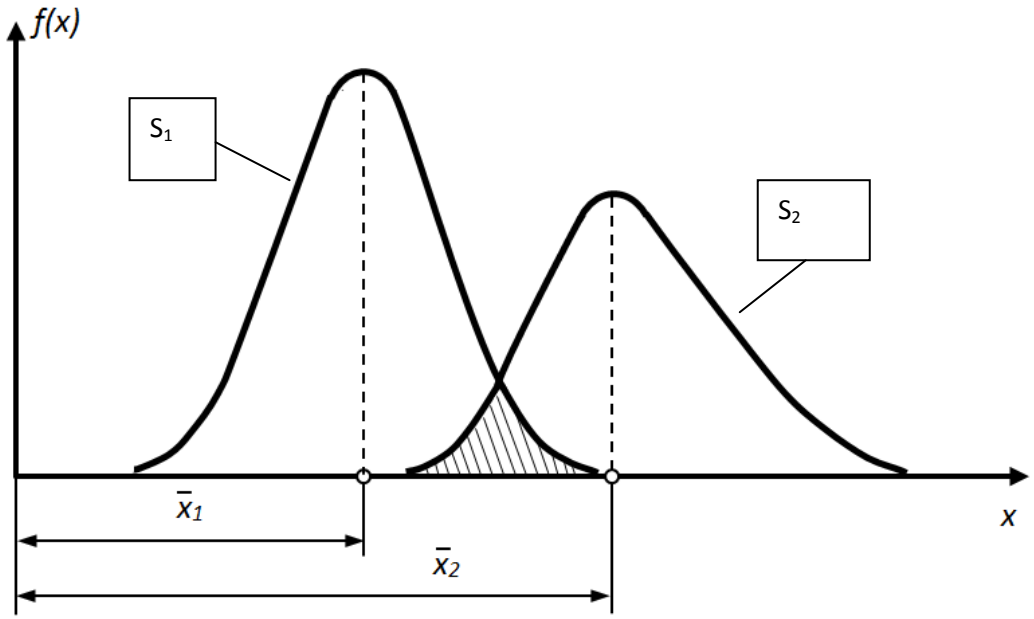

Figure 1: *Densities of the distribution of work until failure of the two models of plant protection machines tested*

In this situation / figure 1/, in order to decide which of the machines as a result of the reliability test has a better performance of the failure-to-build indicator, we have to apply the criterion for the statistical significance of the differences in the numerical characteristics of the performance-to-failure indicator.

The procedure for applying the Student test is as follows:

1.Determination of pooled dispersion:

$$D = \frac{1}{2}(S_1^2 + S_2^2) = 518{,}6$$

2. Determination of the calculated value of the Student's criterion for dependency:

$$t_{изч} = \frac{\left|\overline{X}_1 - \vec{X}_2\right|}{\sqrt{\frac{D}{n_1} + \frac{D}{n_2}}} = 3{,}297 \approx 3{,}30$$

3. Determining the degrees of freedom and choosing the confidence probability for deciding on the statistical significance of the differences in the estimates of the reliability-to-failure indicator characteristic:

$$t_{табл} = t_{a;\nu} = ?$$

The degrees of freedom are determined by the dependence of: $\nu = 2(n-1) = 70;$

and the confidence probability is assumed $\alpha = 0{,}01$ or $\alpha = 0{,}05$. We also accept 0.01 in the table of values of the Student's criterion for $\alpha = 0{,}01$ and $\nu = 2(n-1) = 70;$

we report. $t_{0{,}01;70} = 2{,}618$.

From here, comparing the calculated value of the Student's criterion / 3.30 / with its tabular value / 2.618 / we find that 3.30> 2.618, therefore the differences in the estimation of the average value of the two models' production are statistically significant, ie. the plant protection machine model 2 has a higher performance of the failure-to-failure indicator, / figure 2/.

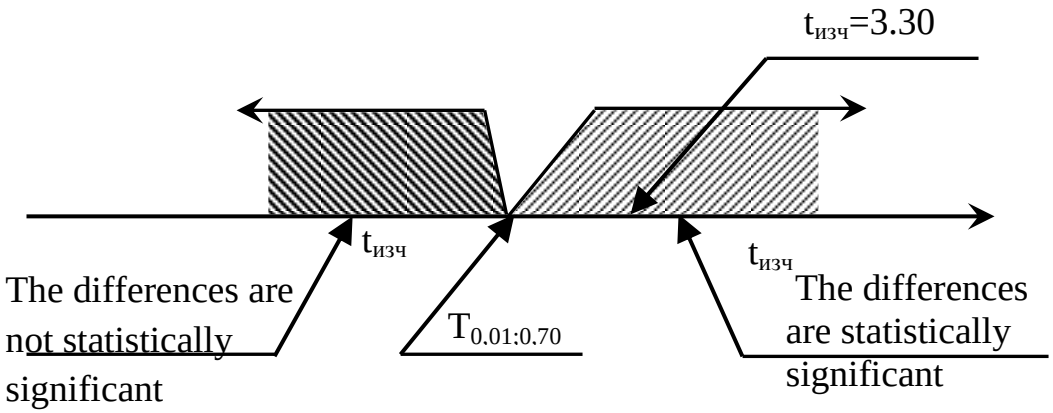

Figure 2: *Graphical representation of the essence of the Student's criterion for deciding the statistical significance of the tested machine parameters.*

Main conclusions:

1. Two models of plant protection machines have been tested and the main numerical characteristics of the indicator production till failure of the characteristic failure-free operation, have been determined .
2. The application of the Student's criterion for proving the statistical significance of the difference in the tested reliability indicator is justified.
3. It has been proven that the Model 2 machine is better in performance till failure than the Model 1 machine .

References:

1.Mihov M., Zh.Davchev, G. Tasev Methodology for the Experimental Study of the Reliability of Technical Objects - Report for the 2020 Ohrid Conference.
2. L.S. Ermolov, V.M. Kryazhkov, V.E. Cherkun, Fundamentals of reliability of agricultural machinery, M., 1982.
3. Skovorodin V., L. Tishkin, G. Tasev, Handbook of reliability of agricultural machinery, S., 1998.
4.Mihov M., Reliability of Machines in Agriculture, S., 2012.
5. Tasev G., Kr. Georgieva Introduction to Research.-S., 2014.

Trial model of a combined machine for inter-row tillage in perennial crops

Ivan Mortev -Institute of Soil Science, Agro-Technology and Plant Protection “Nikola Pushkarov", Sofia, Bulgaria

Summary:P *At the Institute of Soil Science, Agrotechnologies and Plant Protection - Sofia (IPAZR - Sofia) an experimental model of a machine for combined soil treatment in permanent plantations has been developed. The machine is designed to work using technology without turning the soil layer and at the same time at a sufficient depth for fruit plantations. Tests were conducted in laboratory and road conditions to verify the capabilities of the structure. Deficiencies have been identified, as a result of which the work must continue.*
KEY WORDS*: TILLAGE, COMBINED MACHINE, PILOT PLANT*

Introduction

The prototype of a combined machine for inter-row treatment of perennial crops is designed to investigate the capabilities of the structure to perform operations to maintain the soil surface in an optimal condition depending on the requirements of the crop. The trial sample of a combined inter-row tillage machine is made to check the technical characteristics in the subsequent examination of the sample so made.

The purpose of making and researching the experimental model of a combined machine for inter-row tillage is to determine the possibilities for its use in agriculture, and the quality of its work.

Technical characteristics

Description of the construction

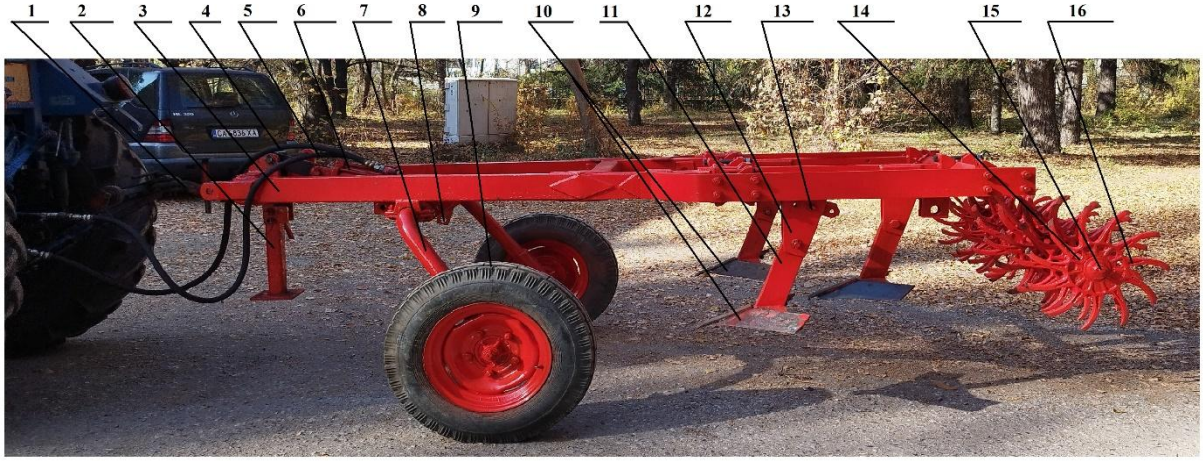

Fig. 1 Experimental model of a combined machine for inter-row treatment of perennial crops, side view

Fig.2. Trial model of combined machine for inter-row cultivation of perennial crops, rear view

The test specimen fig. 1 and fig.2. consists of the following main units: frame 3, chassis 7, towing device 1, working bodies for loosening the soil layer 10, working bodies for crushing lumps and plant residues 16, hydraulic elements 4,5,6, regulating mechanisms. The frame consists of steel profiles, a welding structure on which the fastening elements of the working bodies 12, the towing device 1, the running system 7, the adjustment mechanisms, the mechanisms for bringing them into transport and working position 4,5,6, the safety mechanisms to ensure safe movement are located through a fixed transport position 8. If necessary to move the machine on the republican road network, it must be equipped with light signaling and other devices ensuring safe road traffic in accordance with the law on road traffic and the regulations for its application. Each of the loosening working bodies is attached to the frame by means of a ladder 11, it is provided with safety mechanisms 13 when

overloading the working body to prevent its destruction. They are located in two rows to prevent jamming between the working bodies with soil and plant residues. The type and number of working bodies is determined depending on the required working width on which the machine will work. They can be unilateral or bilateral. Usually, the one-sided ones are placed at the end of the treated strip and provide the protective zone next to the treated plants.

The machine is equipped with second toothed - rotary working bodies 16. The toothed rotary working bodies for crushing the lumps are rotary hoes, they rotate during the progressive movement of the machine and therefore are mounted on consoles and bearing bodies to the frame of the machine 14. They consist of toothed discs arranged on a rotating axis and separated by spacer bushings. The axle 15 bears on the mounting brackets of the frame 16. For a visual representation, a rear view of the machine is given in fig. 2. If necessary, it can be equipped with drum working bodies consisting of grid drums on which the crushing rails are located. Drums can also be one or more. Each drum also bears in bearing brackets attached to the machine frame. It consists of

an axle, spokes, crushing rails. The drums can be mounted to the frame by means of parallelogram mechanisms for better work, copying of the terrain and better crushing of lumps.

Transport and transport position

Bringing the machine into working and transport position is carried out by means of a power cylinder 6 connected to the hydraulic system of the tractor by means of pipelines 4 and 5. The transport position of the machine is presented in fig. 3. After that, it must be secured against lowering by means of a safety mechanism 8, in case of a possible damage to the hydraulic system of the tractor, the machine will be secured against an arbitrary transition to another position. Before separating from the tractor, the machine must be lowered onto stand 2. Stand 2 can be retracted for transport and operation by turning 90 degrees back and fixing with a pin.

Over long distances, the machine is transported by means of a motor vehicle, and the loading and unloading activities are carried out with lifting mechanisms or on a ramp on which the tractor pulling the machine approaches in reverse and separates the machine when it is on the transport vehicle.

Technological process

The technological process takes place in the following sequence: When the unit moves, the machine pulled by the tractor gradually moves and different types of working bodies perform different work. The loosening working bodies are driven into the soil and cut, lift and partially move the soil layers, cut weeds and plant residues at the depth to which the machine is pre-set.

Fig. 3. Trial sample of a combined machine for inter-row processing of perennials in transport position

Crushing rotary hoes, due to the forward movement on one side and the friction in the soil and the forces of the earth's gravity, perform a complex movement, a rotary movement relative to the machine frame and a forward movement relative to the field. The trajectory of each of the teeth of the rotary hoe describes the trajectory of a complex tracheid. As a result, the teeth sink into the soil and crush the clods, bring the weeds to the surface of the soil and help to break their bonds with the soil and this leads to their destruction. The drum working units, like the toothed rotary working units, rotate around their axes and break up the lumps and plant residues and weeds through the working rails.

Technical specification

№ per lines	Parameters	Data, Values	Measuring units
1	Machine type	Attached	
2	Dimensions		mm
2.1	Length	4100	mm
2.2	Width	1900	mm
2.3	Height	900	mm
3	Mass	950	kg
4	Working width		mm
4.1	On the machine	1850	mm
4.2	On a working body	620	mm
5	Aggregation	1,4, 2, 3 Depending on the depth of cultivation and soil resistance.	Tractor class
6	Movement speed	2 - 20	km/h
6.1	Working	2-10 under the conditions as point 5	km/h
6.2	Transportation	until 20	km/h
7	Processing depth	up to 500 under the conditions as point 5	mm
8	Staff	1 mechanic	number
9	Storage area	8	m^2

10	Ground clearance	300	mm
11	Machine base	1600	mm
12	Transmission	Wheel running system	type
12.1	Wheel type	pneumatic	Type
12.2	Quantity of wheels	2	number
12.3	Tire size	170-406 600-16 ГОСТ 7463-80	tsol
12.4	Tire pressure	3	kg/sm^2
12.5	Track	1800	mm
13	Productivity	0,2-1,4 under the conditions as point 5	ha/h

The developed experimental model of a machine for soil treatment in permanent plantations should be improved and the problems discovered during the testing process should be eliminated.

Due to the heavy weight of the structure, bringing it into transport and working position through the hydraulic system of the tractor is accompanied by vibrations. When the running system of the machine is brought into the transport position, the weight reacts, which causes the safety valves in the hydraulic distributor of the tractor system to operate, and as a result, the hydraulic hinged system begins to lift. The two hydraulic cylinders of the machine and the tractor begin to affect each other and the lifting of the tractor hitch tilts the rear of the machine down, making it difficult to get into the transport position as well. This shortcoming can be solved in subsequent research by replacing the machine's hydraulic cylinder with a longer stroke.

Conclusions

1. A pilot model of a combined machine for tillage in permanent plantations has been developed and tested. The in-service inspection showed an acceptable quality of row spacing treatment. To increase it, optimization of the operating mode parameters is required.

2. The identified problems in the operation of the hydraulic system of the machine necessitate a partial change of the design, type and location of the hydraulic cylinders.

References

1. Braykov, Ivan, Optimizing the working speed during tillage during pepper growth period, Collection of scientific reports of the international scientific conference 50 years Forestry University, April 1-2, 2003. pp. 58-60.
2. Georgiev I., S. Stanev, S. Shishkov, Agricultural Machinery, Sofia 1975.
3. Irinchev, D., Power of an agricultural tractor during pulling operations, Agricultural University - Plovdiv, Agricultural Sciences, Year IV Issue 12, 2013, pp. 109-111.
4. Manushkov, Stiliyan, Georgi Mitev, Zhivko Demirev, Machines for tilling the soil without turning the layer, Scientific works of Ruse University - 2013, volume 52, series 1.1, 191 -197 Ruse University, Ruse, Bulgaria http://conf.uni-ruse.bg/bg/docs/cp13/1.1/1.1-34.pdf
5. Z. Kurdov, M. Mihov. Quantities and units according to BDS-ISO with application in research in the field of agricultural machinery – magazine "Agricultural machinery", 1997, N1., pp. 42-48
6. Machinery for viticulture https://agronica-karov.com/viticulture/disc-harrow-for-vineyards/
7. Mitev, Georgi, Innovative technology for protecting agricultural lands from degradation, INTERNATIONAL SCIENTIFIC JOURNAL "MECHANIZATION IN AGRICULTURE" WEB ISSN 2534-8450; PRINT ISSN 0861-9638, https://stumejournals.com/journals/am/2015/6/3.full.pdf
8. Mihov M., R. Dragneva, G. Tasev. Methodological foundations for rational aggregation of tractors. - magazine "Agricultural machinery", 1989, N5, p. 43-53.
9. Mihov M., M.Borisova, E.Vidinova - Factors determining the quality of the main and pre-sowing tillage of the soil, journal of agricultural technology, No. 2, 2004, pp. 3-6
10. Specialized machinery for perennial crops https://www.opticom-bg.com/products/cat_new/70/74
11. Tractor Bolgar MTZ-80, Operation and maintenance manual
12. Tasev G., ... , M. Mihov, Methodical foundations of research methodology, ed. Avangard prima, Sofia, 2022, 698 p.Harry L. Field and John B. Solie, Introduction to Agricultural Engineering Technology, A Problem Solving Approach, Third Edition, Oklahoma State University, Stillwater, OK, USA
13. Lal R., Tillage and agricultural sustainability, Soil and Tillage Research, Volume 20, Issues 2–4, June 1991, Pages 133-146 https://www.sciencedirect.com/science/article/pii/016719879190036W
14. Johan Arvidsson Inge Håkansson, A model for estimating crop yield losses caused by soil compaction Soil and Tillage Research Volume 20, Issues 2–4, June 1991, Pages 319-332 https://www.sciencedirect.com/science/article/pii/016719879190046Z?via%3Dihub

A new type of nail for wooden structures with increased resilience

Petar Bodurov[1], Pencho Sirakov[1], Raul Turmanidze[2], Giorgi Popkhadze[2]
[1]Relo-Nail Ltd., Oborishte Str. 1/A/17, 1504 Sofia, Bulgaria,
[2]Georgian Technical University (GTU), Faculty of Transportation and Mechanical Engineering, 0171 Tbilisi – Georgia
pbodurov@mgu.bg, inform@gtu.ge

ABSTRACT :*In the following work, we present the results from a research of a type of nail with a new form of section, in comparison to the round section that currently used nails have. This new form is similar to an equilateral triangle, the sides of which' are curves [Reuleaux Triangle]. The body section of this new type of nail has three curves and three edges; his surface SR is with 5.56% larger than the surface SC of a round nail with the same section area. From the experimental research that has been made so far, it was established: (i) because of the larger compaction of the wooden material in the ends of the edges, and of the larger surface, you get a bigger friction force, resulting in a pulling-out force Fto,R that is on average twice as bigger as the pulling-out force Fto,C; (ii) because that the new form of nail has edges, this leads to bigger resistance during the rotating of the joined wooden elements one against another – the moment Mr is on average 60% bigger than the one with elements, joined with a normal nail. These advantages, as well as the use of the existing technology and machines for the production of nails without having to effect any major changes, create the conditions for the application of the new type of nail in construction, furniture production and in the everyday life, for an output of products with larger resistance to external forces. This effect will be especially useful for increasing the residential buildings' resilience during earthquakes, hurricanes and other natural disasters.*
KEYWORDS *NAILS, REULEAUX TRIANGLE, WOODEN STRUCTURES*

I. INTRODUCTION

The production of nails worldwide is one of greatest in fabricated metal products: reinforcing bars – 400 million tons, sheet metal – 240 million tons, pipes – 60 million tons nails, and screws – 32 million tons in 2014 [1]. Nails are used for connecting elements of wooden constructions; the largest quantities are used for wooden-frame houses. The average wooden-frame house uses require between 20,000 and 30,000 nails of various types and sizes [2]. Earthquakes or hurricanes are considered as extreme conditions for those structures. A variety of nails is available for wooden structures, which are to be under heavy loading conditions – Fig. 1 [3], [4], [5].

Most of these nails have a number of advantages, compared to conventional nails, but they are difficult to be manufactured in the existing automatic machines for nails and have a higher price.

The new type of nail[10] has a section, known as the Reuleaux Triangle. This geometrical figure has a shape, formed from the intersection of three circles, each having its center at the vertex of a triangle

– Fig. 2. The radius R is equal to the length of the triangle's side. In Fig. 2 we see that the Reuleaux Triangle includes three curves and three edges.The Reuleaux Triangle can be seen as a closed convex curve of constant width. This is a type of curves which, when rotated in a square, make contact with all four sides [6]. The other definition is that of "curves of constant width that have the same "width" regardless of their orientation between the parallel lines" [7]. The surface – that is the curve with the largest area – also belongs to this type, while the Reuleaux Triangle is the closed curve with the smallest area, but with the same perimeter.

The more important qualities of the Triangle are:

- Its radius R = 2,112r, where r is the radius of a circle with the same area.
- With the same area, the perimeter of the Reuleaux Triangle PR is 5.56% larger than the perimeter PC of the given circle.
- The second moment of area I and the elastic section modulus S, when you have a circular section, are the same as regard to a coordinate system, passing through the center of gravity in the circle, therefore with a cicle Ix,c = Iy,c, Sx,c = Sy,c. With the Reuleaux Triangle Ix,R = Iy,R, Sx,R ≠ Sy,R as regards to a coordinate system, passing through the section's center of gravity.

In agreement with the definition for S [8], [9] from Fig. 2b we can see that with the Triangle there are two elastic section modulus SR,y (SR,y1, SR,y2) and one elastic section modulus SR,x:

$$S_{(R,y1)}=I_y/b;\quad S_{(R,y2)}=I_y/a\ ;\quad S_{(R,x)}=I_x/0.5R \qquad (1)$$

By looking at the geometric proportions in an equilateral triangle it can be determined that a = 0.577R , b = 0.423R and (1) becomes:

$$S_{(R,y1)}=I_y/0.423R;\quad S_{(R,y2)}=I_y/0.577R;\quad S_{(R,x)}=I_x/0.5R \qquad (2)$$

where [6]

$$I_x=I_y=1/48(10\pi-17\sqrt{3})R^4 \qquad (3)$$

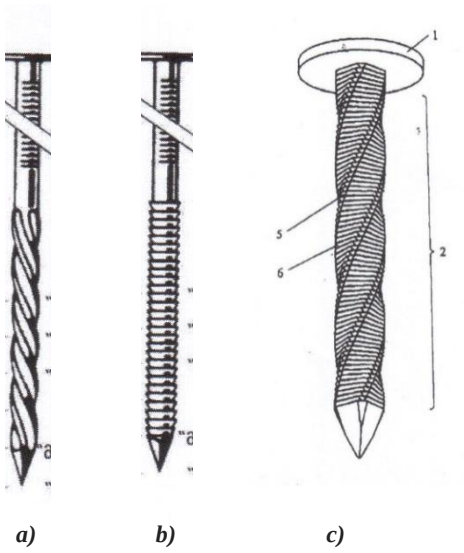

a) *b)* *c)*

Fig.1. *Design of nails for heavy loading wooden structures:a - with rolled rings; b – with rolled screw channels; c – with screw canals and rings: 1- nail heat, 2 – nail body, 5 – screw cylindrical surface, 6 – linear rings*

Here we present the results from our comparative experimental research for determining the maximal forces and moments, which impact wooden structures, the elements of which are to be joined with a nail with a round section, or a section of the Reuleaux Triangle type.

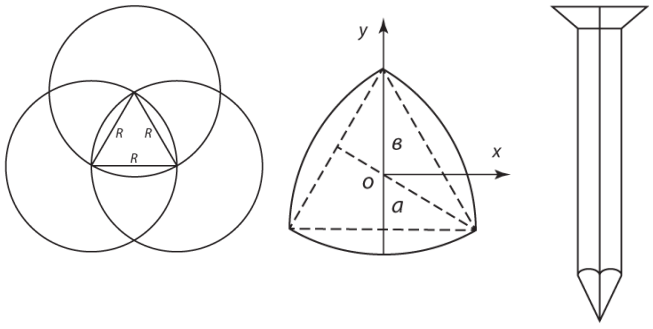

a) **b)** **c)**

***Fig. 2. a – a** Reuleaux Triangle; b – a scheme for determining the elastic section modulus S; c— a nail with a Reuleaux Triangle section*

II. METHODICS

A round section nail with the following characteristics: radius RC = 3.5 mm, length LC = 190 mm, area of the counter-section A = 38.46 mm2, perimeter PC = 21.98 mm, was used in the experiments. The nail with the Reuleaux Triangle section, was with the same area A, radius RR = 7.392 mm, length of the section portion LR = 85 mm (the length of the entire round section nail is 145 mm), perimeter PR = 23.2 mm – Fig. 3; his edges were rounded with radius R = 0.5 mm. There have been made 10 such nails, with the Reuleaux Triangle section portion been made on a filament erosion machine.

In Table 1. are given the values of the second moment of area I and the elastic section modulus S for the two types of nails.

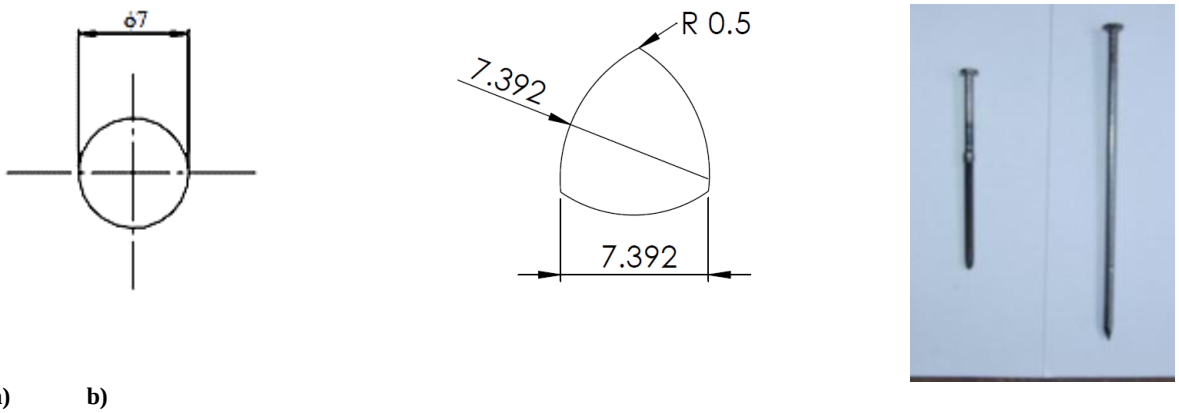

a) **b)**

***Fig. 3.** Comparison of the ordinary and the new nails: a – comparison of the cross-section dimensions; b - view of the used nails with the new shape and ϕ7*

***Table 1.** Value of I and S for ordinary and new nails*

Section	I_x, mm^4	I_y, mm^4	$S_{y,1}$,mm^3	$S_{y,2}$,mm^3	S_x, mm^3
Circle	117.8	117.8	33.65	-	33.65
Relo	122.54	122.54	39.19	28.73	33.15

There were two types of experiments.

2.1 Experiments for determination of the take-out force Pto

In that case wooden elements (beams) made out of dry coniferous wood with sizes (length x height x width): 150 mm x 60 mm x 48 mm. We drive in them nails of the two types so that the top of the nail comes out of the other side of the wooden element. After that the nail is taken-out. A mechanical testing machine Instron1195 was used, allowing to mark-down the diagram moving – force when we drive and take-out the nails. From these diagrams we calculate the maximum force of the driving in and the removal. We drilled, in advance, holes with 3 mm diameter in the wooden elements, to assure the driving was to be done easily, and without unnecessary force that would possibly lead to the deformation of the nails. There were 10 experiments held with each of the two types of nails.

2.2 Experiments for determination of the torque Mr

In this case, wooden slats with dimensions (thickness x length x width) 30 mm x 200 mm x 65 mm from dry coniferous wood were used. Two slats are connected to each other with a nail at a 900 angle. The resulting wooden structure was tested in rotation under two types of load: when an external force acts simultaneously on the two slats - Fig. 4.; when an external force acts on only one slat - Fig. 5. The maximum moment at which the structure becomes inefficient (the slats are rotated relative to each other) is denoted with by and respectively. Using the calculation schemes for these moments shown in Fig. 3c and Fig. 4c is obtained:

$$M_r^{two} = 2 \times 0.2 \times 0.3543F \text{ , Nm} \qquad (4)$$

M_r^{one} = 0.155F, Nm

a) **b)**

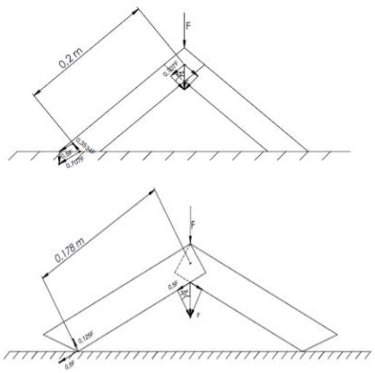

c) **d)**

***Fig.4.** Pictures of tested wooden structure when force acts simultaneously onthe two slats: a – in the beginning; b – during the experiment; c, d – scheme to determine the moment*

a)

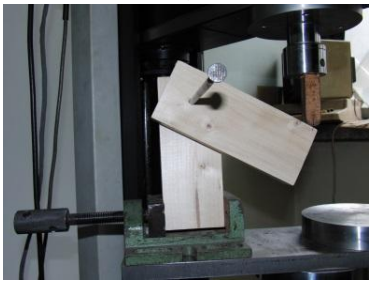

b)

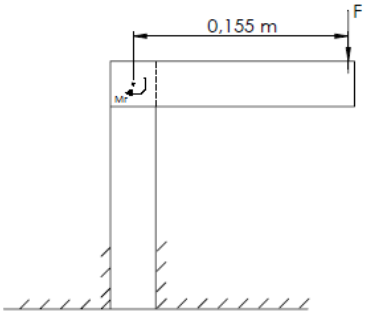

c)

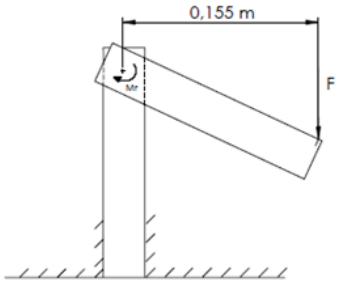

d)

Fig.5. *Pictures of tested wooden structure when force acts on one slat:*
a – in the beginning; b – during the experiment;
c, d – scheme for determine of torque

III. RESULTS

3.1 Determination of the driven and take-out forces

The driving of the nails is at a speed of 10 mm / min, and the removal of them is at a speed of 20 mm / min. The obtained values of the forces of driving Fd and take-out Fto are given in Table 2.

When connecting the wooden slats, the nails were driven in at a speed of 10 mm / min. The speed of movement of the contact element in the torque test Mr was 5 mm / min. The results are shown in Table 3. Due to the small differences in the values of the moments in the individual experiments, in Table 3 only their average values are given.

Table 3. *Average values of* M_r^{two} *and* M_r^{one}

Crosssection	M_r^{two}, Nm	M_r^{one}, Nm
Circle	20.83	7.6
Releaux Triangle	34.72	15.2

Table 2. *Driven in and take-out forces*

Type	Driven forceF_d, N	Take out force F_{to}, N
Circle cross-section	3728	2453
	3267	2158
	3482	1864
	3709	2394
	2943	2551
	3434	2048
	3744	2366
	3160	2370
	3460	2483
	3420	2644
Average	**3435**	**2333**
Relo Triangle cross-section	4513	5494
	4218	4513
	4120	5297
	4120	5240
	4120	4905
	4218	5248
	4194	4463
	4124	4562
	4158	4470
	4262	5274
Average	**4205**	**4947**

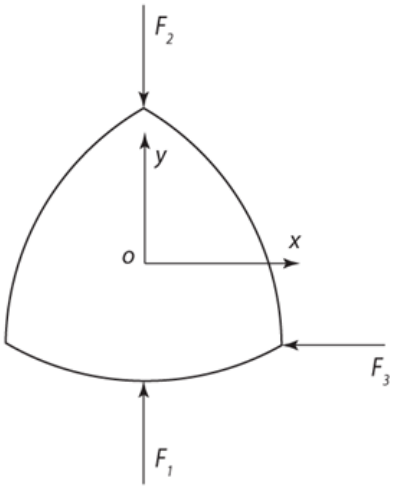

Fig. 6*. A scheme of the forces, acting upon a section of a Reuleaux Triangle nail, when determining the elastic section modulus S: F1> F3> F2*

IV. CONCLUSION

From Table 1 it can be seen that the resistance against elastic bending of a nail with a section of the Reuleaux Triangle depends on the application point of the external force. Fig. 6 shows the forces F1, F2 and F3, which are used to determine the elastic section modulus S. The difference in the magnitude of these forces gives us grounds for the following conclusion:

When it is necessary to achieve maximum resistance against elastic bending of a nail with a Reuleaux Triangle section, when driving the nail it must be oriented so that the external force acts in the direction of the force F1 from Fig. 6.This means that, when using the new nail, an oriented driving can be performed according to the location of the edges on its stem. Oriented driving is a unique quality of the new nails, which will lead to drastic changes in the integration of wooden structures.

From Table 2. we can calculate the difference between the average forces of driving and removing a nail with a round section and with the Reuleaux Triangle one:

When driving a nail with a section of Relo's Triangle, the force Fd,R = 1.24Fd,C.

When removing a nail with a section of the Relo Triangle, the force Fto,R = 2.12Fto,C.

This means that wooden structures, whose elements are joined with nails with a Reuleaux Triangle section, will have twice as much resistance to destruction as those, joined with ordinary nails, when the wooden structures are subjected to superior destructive forces.This result can be explained by the following effects, which occur when driving and taking-out a nail with a Reuleaux Triangle section: (i) in the ends of the edges of the nail you get a compaction of the wooden material, which increases the coefficient of friction and the friction force in these areas along the length of the nail; (ii) the larger perimeter determines a larger area of the surrounding surface of the nail body and hence a greater friction force on this surface than the friction force arising on the surrounding surface of a nail with circular section.

From Table 3. it can be determined:

When an external force acts simultaneously on two elements of a wooden structure, the maximum moment at which the elements will not rotate relative to each other is M_(r,R)^two = 1.66 M_(r,C)^two.When an external force acts on an element of a wooden structure, the maximum moment at which the elements will not rotate relative to each other is M_(r,R)^one = 2M_(r,C)^one.This means that wooden structures, which elements are connected with a nail with a Reuleaux Triangle section will have between 1.66 and 2 times more resistance to destruction than those, connected with ordinary nails, when forces, which strive to rotate the wooden elements relative to each other, act on them. This result is due to the presence of three longitudinal edges on the body of the nail with a Reuleaux Triangle section.

The presented results were obtained by using one nail of each type to connect the wooden elements. When using N number of nails, the effects of applying a nail with a section of the Relo Triangle will increase in proportion to N, when building wooden structures. In this way, greater resistance of wooden structures can be achieved, both in conditions of static external forces (furniture) and in dynamic forces (hurricanes, earthquakes, floods).

An important feature that can help the wide application of the new type of nails is that for its production the same materials, machines and technologies are used, which are used for the production of nails with round section.

REFERENCES

[1] http://www.anythingresearch.com
[2] http://www.madehow.com
[3] http://www.strongtie.com
[4] M.Haroldsen, Needles made from non-round stock, EU Application 93112434.1, 09.02.1994
[5] V.Kolev, A.Ivanov, Nail, Patent BG 65071 B1, 31.01.2007.
[6] http://mathworld.wolfram.com/ReuleauxTriangle.html
[7] http://mathworld.wolfram.com/CurveofConstantWidth.html
[8] N.Anward, F.Najam, Structural Cross-Sections Analysis and Design, Butterworth-Heinemann, 2016, ISBN 9780128044438
[9] J.Ochshorn, Structural elements for Architects and Builders. Design of Columns, Beams and Tension Elements in Wood, Steel and Reinforced Concrete, Butterworth-Heinemann, 2009, ISBN 9781856177719
[10] P. Bodurov, P. Sirakov, T. Penchev, D. Mihaylov, NAIL, HAGUE, European Union(EM), (DM/213 785), 12.04.2021.

Physico-chemical characterization of the corn silk by DTA-TGA, SEM-EDS and FTIR analysis

Milan Gorgievski [1*], Dragana Božić [2], Miljan Marković [1], Nada Štrbac [1], Vesna Grekulović [1], Kristina Božinović [1], Milica Zdravković [1]
University of Belgrade Technical Faculty in Bor, Vojske Jugoslavije 12, 19210 Bor, Serbia[1]
Mining and Metallurgy Institute Bor, Zeleni bulevar 35, 19210 Bor, Serbia[2]
mgorgievski@tfbor.bg.ac.rs

Abstract: *In this paper, the results of the DTA-TGA, SEM-EDS, and FTIR analysis of the corn silk are presented. The DTA-TGA analysis shows that the decomposition of corn silk has several stages which are manifested with corresponding peaks on obtained DTA-TGA curves. SEM-EDS analysis was performed before and after the adsorption of copper ions. It has shown that untreated corn silk has a non-uniform structure, consisting of channels and cavities of irregular orientation, which facilitates the penetration of the water phase into the adsorbent structure, and incorporation of copper ions in the internal active sites. After the adsorption of Cu^{2+} ions, the structure becomes more compact, and uniform, as a result of the incorporation of copper ions into the molecular structure of the corn silk. FTIR analysis shows that ion exchange is not the dominant mechanism of binding copper ions to the active sites in the molecular structure of the corn silk, but also chemisorption and physical adsorption is present.*

Keywords*: CORN SILK, CHARACTERIZATION, DTA-TGA, SEM-EDS, FTIR, COPPER IONS*

1. Introduction

Water pollution with heavy metals is a significant environmental problem all over the world. Most of these pollutants are not biodegradable and tend to accumulate in living organisms. Their toxicity, along with their non-biodegradability makes the polluted wastewater purification an initial concern [1].

Conventional methods for wastewater purification include ion exchange, chemical precipitation, membrane processes, electrolysis, etc [1, 2]. Among these wastewater treatment methods, sorption has shown good prospects, thanks to its economic feasibility, and environmental-friendly nature [2].

The use of waste biomass, including agricultural by-products, as adsorbents for wastewater purification, has been very popular in the scientific world in the past decade. This process is often referred to as biosorption. The main advantages of the biosorption process are the low-cost, biodegradability, efficiency, ease of operation and simplicity of design, and abundance of potential biosorbents. Further, this process can remove/minimize the different types of pollutants, and thus it has wider applicability in water pollution control [2, 3].

Corn silk (*Stigma maydis*) has been used for thousands of years as a folk medicine in many parts of the world for the treatment of edema as well as for cystitis, gout, kidney stones, nephritis, diabetes mellitus, and prostatitis [4].

Corn silk is a by-product of corn after deep processing, and is one kind of crop waste, widely available in large quantities. Corn silk, whose components are significantly different from maize stalk, maize corncob, and maize leaf, mainly contains cellulose. However, corn silk is constituted of lignin and cellulose and there are a large number of oxygen-containing functional groups, such as hydroxyl groups, carboxyl, and carbonyl on its surface classifying it as a potential adsorbent for metal ions [1, 5]. However, there are only a few papers dealing with metal removal by raw or modified corn silk [1, 6].

In this study, SEM-EDS, DTA-TGA, and FTIR analysis of corn silk, as a potential adsorbent for copper ions biosorption is given. The SEM-EDS and FTIR analysis was performed on samples before and after the biosorption process.

2. Materials and methods

Corn silk was collected from the local cornfields near the city of Bor (Serbia). Collected samples were firstly washed, ground, then sieved through a set of laboratory sieves, and the sieve fraction (−1 + 0.4) mm was analyzed for potential use as an adsorbent for copper ions biosorption.

A synthetic Cu^{2+} solution of an initial concentration of 0.2 g dm^{-3} was used for the adsorption experiments, to obtain a corn silk sample after the biosorption process for the SEM-EDS and FTIR analysis.

The SEM-EDS analysis was performed on a VEGA 3 LMU TESCAN scanning electron microscope, coupled with an integrated energy-dispersive X-ray detector X-act SDD 10 mm^2 (Oxford Instruments).

The DTA-TGA analysis was performed on a simultaneous DSC-DTA-TGA device (SDT-Q600), under an inert atmosphere (nitrogen).

The FTIR analysis of the corn silk samples before and after the biosorption process was performed on a BOMEM MB-100 (Hartman & Braun Michelson) FTIR spectrometer.

3. Results and discussion

3.1 SEM-EDS analysis of corn silk

Based on a large number of results from scientific research in which the SEM analysis of different biosorbents was performed, the corn silk was analysed before and after the biosorption process. On the basis of the SEM analysis, in which the surface of the samples was observed, certain differences in the structure of the surface before and after the biosorption process were noted. The surface morphology of the corn silk samples before and after the biosorption process is shown in Figure 1.

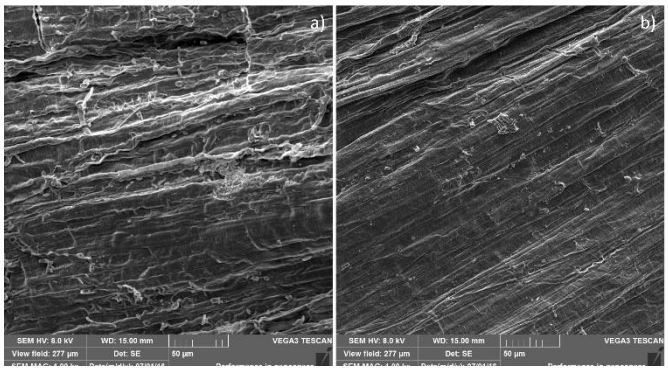

Figure 1. *SEM micrographs of the corn silk samples before (a) and after the biosorption of copper ions (b)*

Figure 1a shows a micrograph of the surface of untreated corn silk. Macro-pores and cavities can be seen in the image. The presence of macro pores and larger cavities facilitate the movement of the aqueous phase through the corn silk structure and promotes internal diffusion. The cavities and macro-pores of untreated corn silk have a chaotic and irregular orientation, and their openings are also irregularly shaped, as can be seen in Figure 1a. It is assumed that metal ions through these pores easily penetrate into the structure of the adsorbent where they are adsorbed on numerous

internal active sites [6]. Similar morphological changes in biosorbents were observed by other authors using SEM analysis in their works [7, 8].

After the biosorption process, a change in the morphology of the surface is noted (Figure 1b), compared to the untreated sample. Figure 1b shows a relatively uniform structure of the corn silk sample. The change in morphology is manifested as a compact cellulosic structure, where no pores are observed, and the surface has become rough [9]. The given changes in the morphology of the sample lead to the conclusion that the adsorption of copper ions is related to chemical changes on the surface of corn silk.

The EDS spectra of corn silk samples before and after the biosorption process are shown in Figure 2. As can be seen from Figure 2a, pointed on the alkali and alkali earth metal ions, the EDS spectrum before the biosorption of copper ions shows a high content of Ca, K, and Mg. After the biosorption process, the K peaks decreased with the disappearance of Ca and Mg peaks, and peaks for Cu were observed (Figure 2b). Hence, it could be assumed that the ion-exchange mechanism occurs between Ca^{2+}, Mg^{2+}, K^{+}, and Cu^{2+} ions [10].

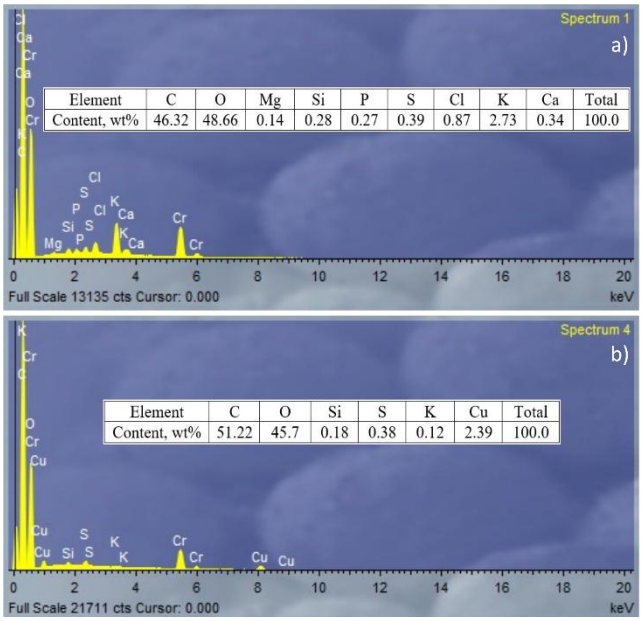

Figure 2. *The EDS analysis of the corn silk samples before (a) and after the biosorption of copper ions (b)*

3.2 DTA-TGA analysis of corn silk

The DTA-TGA analysis of corn silk was performed in order to determine the thermal stability of the biosorbent. 4 mg of corn silk was heated at a constant rate of 10 °C/min in the range from 20 °C to 900 °C, and the obtained results are shown in Figure 3.

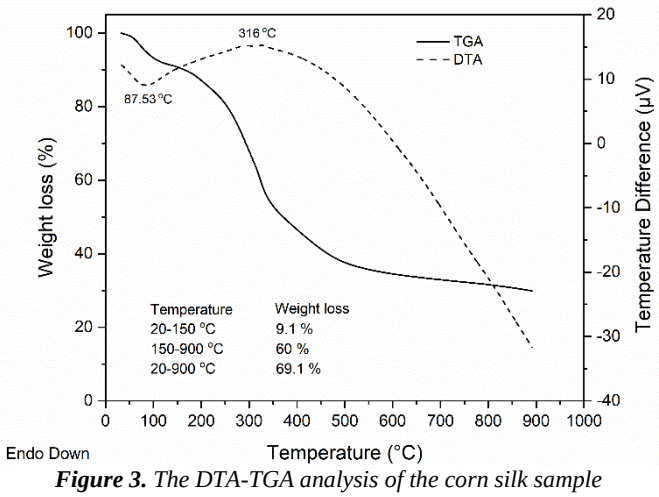

Figure 3. *The DTA-TGA analysis of the corn silk sample*

Figure 3 shows the DTA and TGA profiles of corn silk. The TGA curve shows a weight loss of 9.1 % in the temperature range from 20 to 150 °C, as a result of the loss of physically bound water within the sample. This process is followed by an exothermic peak on the DTA curve with a minimum of 87.53 °C. Further, in the range from 150 to 900 °C, the TGA curve shows a weight loss of about 60 %, which can be contributed to the degradation of the lignocellulose components present in the corn silk sample, and the formation of volatile products like CO, CO_2 and others [10, 11]. This change is followed by an exothermic peak on the DTA curve, with a maximum of 316 °C. The total weight loss, in the temperature range from 20 to 900 °C, was 69.1 %.

3.3 FTIR analysis of corn silk

FTIR spectroscopy is an instrumental method used to determine the functional groups in the adsorbent responsible for ion exchange with metal ions from the solution. The FTIR analysis of the corn silk samples was performed in the spectral range from 4000-400 cm^{-1}, with a resolution of 2 cm^{-1}. The obtained results are shown in Figure 4.

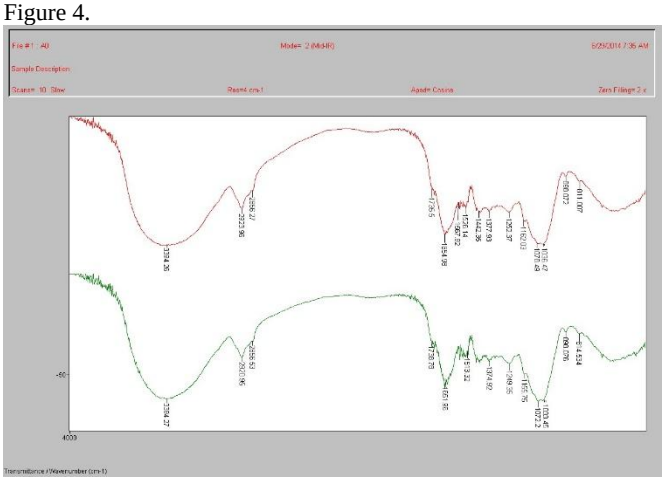

Figure 4. *FTIR spectra of the corn silk samples before (green band) and after the biosorption of copper ions (red band)*

The obtained FTIR spectra before and after the biosorption process do not show significant shifts in the terms of wavelengths, which suggests that ion exchange is not the dominant mechanism of binding copper ions to the active sites in the molecular structure of the corn silk, but also chemisorption and physical adsorption is present.

4. Conclusions

The characterization of corn silk, as a potential adsorbent for copper ions biosorption is presented in this work. The SEM-EDS analysis was performed on corn silk samples before and after the biosorption of copper ions. The SEM analysis showed a change in the surface morphology of the corn silk samples after the biosorption process. The macro-pores and cavities, present on the SEM image before the biosorption process, disappeared, and the structure of the corn silk sample became more uniform and compact. The change in the morphology of the sample occurred as a result of the incorporation of the copper ions inside the structure of the corn silk.

DTA-TGA analysis was performed on a corn silk sample to determine its thermal stability. The sample was heated at a constant rate of 10 °C/min, from 20 °C to 900 °C. The obtained results showed a total weight loss of 69.1 % in the analysed temperature range indicating the degradation of the lignocellulose components in the sample.

The FTIR analysis was performed on samples before and after the Cu^{2+} ions biosorption. The obtained FTIR spectra showed no significant shifts in the terms of wavelengths. This led to the conclusion that ion exchange is not the dominant mechanism of binding copper ions to the active sites in the molecular structure of

the corn silk, but also chemisorption and physical adsorption is present.

5. Acknowledgment

The research presented in this paper was done with the financial support of the Ministry of Education, Science and Technological Development of the Republic of Serbia, within the funding of the scientific research work at the University of Belgrade, Technical Faculty in Bor, according to the contract with registration number 451-03-68/2022-14/200131.

6. References

1. H. Yu, J. Pang, T. Ai, L. Liu, *J. Taiwan. Inst. Chem. Eng.* **62** (2016), 21-30.
2. G. Tan, H. Yuan, Y. Liu, D. Xiao, *J. Hazard. Mater.* **174** (2010), 740-745.
3. A. Bhatnagar, M. Sillanpää, *Chem. Eng. J.* **157** (2010), 277-296.
4. Q.-L. Hu, L.-J. Zhang, Y.-N. Li, Y.-J. Ding, F.-L. Li, *Int. J. Phys. Sci*. **5(4)** (2010), 321-326.
5. H. Yu, J. Pang, M. Wu, Q. Wu, C. Huo, *Anal. Sci.* **30** (2014), 1081-1087.
6. M. Petrović, T. Šoštarić, M. Stojanović, J. Petrović, Č. Lačnjevac, K. Trivunac, S. Stanković, *Zaštita Materijala* **57** (2016), 480-487.
7. J. O. Ighalo, A. G. Adeniyi, *SN Appl. Sci.* **2** (2020), Ar, No 509.
8. D. Božić, M. Gorgievski, V. Stanković, M. Cakić, S. Dimitrijević, V. Conić, *CICEQ* **27** (2021), 21-34.
9. M. Petrović, T. Šoštarić, M. Stojanović, J. Milojković, M. Mihajlović, M. Stanojević, S. Stanković, *J. Taiwan. Inst. Chem. Eng.* **58** (2016), 407-416.
10. P. M. K. Reddy, P. Verma, C. Subrahmanyam, *J. Taiwan. Inst. Chem. Eng.* **58** (2016), 500-508.
11. H. Yang, R. Yan, H. Chen, D. H. Lee, C. Zheng, *Fuel* **86** (2007), 1781-1788.

Application of characterisation methods in the development of biomedical titanium alloys

Magdalena Jajčinović[1,*], Ljerka Slokar Benić[1], Robert Pezer[1], Tamara Holjevac Grgurić[2]
University of Zagreb, Faculty of Metallurgy, Croatia[1]
Catholic University School of Medicine, Croatia[2]
magdalenaj@simet.unizg.hr

Abstract:
Biomaterials are becoming an increasingly important research topic over time as they are used to replace parts and functions of the human body, helping to improve the quality of human life. Titanium alloys are particularly important for the development of new biomaterials. Commercial pure titanium and its alloys are used as essential structural biomaterials in the manufacture of implants due to their excellent biocompatibility, good corrosion resistance and mechanical strength. However, studies have shown that aluminum and vanadium ions are released in alloys such as Ti-6Al-4V, which can cause health problems over time. Because of the problems that occur, researchers are working to improve the properties of titanium alloys by adding new elements. In most cases, different metals are added to titanium and it is known that with the presence of different metals, the properties of titanium also change. All biomedical titanium alloys must undergo various testing procedures before they can be used. The article describes the characterisation methods used in the development of titanium alloys, such as: light and scanning electron microscopy, energy-dispersive spectrometry, X-ray diffraction analysis, differential scanning calorimetry, differential thermal analysis. The reliability of the results depends on the methods used and the avoidance of errors in the characterisation of biomedical alloys in order to reach better conclusions and produce alloys of the highest quality desirable for use in the human body.
Keywords*: BIOMEDICAL ALLOYS, Ti-ALLOYS, CHARACTERISATION, PROPERTIES*

1. Introduction

After the first meeting on biomaterials, held in South Carolina in 1969, the field of biomaterials received a lot of attention. [1] Nowadays, biomaterials play an important role. [2] Biomaterials are artificial or natural materials. They are used to make structures or implants to restore form or function or to replace a diseased or lost biological structure. [3,4] In this way, biomaterials help to improve the quality of life. [1] With the advances in medicine and materials processing in recent decades, a large number of biomaterials have been developed with properties suitable for various applications. [2] Metals have been used for decades for various applications in medicine. They are used in different parts of the body, such as artificial heart valves, as replacement implants in the knee, hip, elbow and shoulder, as stents in blood vessels and as dental implants. A large number of biomaterials are used for hip, spine and knee replacements. [1,5] Biomaterials must meet various criteria such as sufficient strength, bioadhesion, osseointegration ability, biofunctionality, high corrosion resistance, biocompatibility, high wear resistance and low friction. [6, 7] Biomaterials are also characterised by their biocompatibility. Biocompatibility is an important property of the material. [8] From studies conducted, elements such as Ti, Mo, Nb, Zr, W, Ta, Au and Sn are highly biocompatible, while Al, V, Cr and Ni are elements considered hazardous to the human body. Figure 1 shows detailed information about pure metals and their biocompatibility. [9]

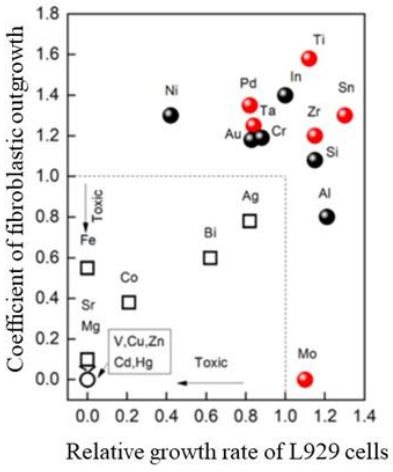

Fig. 1 *Pure metals and their biocompatibility* [9].

Metals and alloys used in biomedicine include stainless steels, titanium and cobalt based alloys. [6, 10] Only commercially pure titanium (CP-Ti) has the best biocompatibility among metallic materials, but its mechanical properties are not satisfactory. [11] Titanium and titanium alloys are currently the most commonly used metals in the manufacture of medical components, especially implants. Their natural properties such as low density and thus low weight, good corrosion resistance, low modulus of elasticity, wear resistance, high mechanical strength, relatively low modulus of elasticity, excellent biocompatibility and non-magnetic behavior give them an advantage over other metals such as chromium and cobalt alloys and stainless steels. [6, 9, 12] Titanium has long been considered a safe and inert element for human use. It also produces minimal side effects in the human body. This can also be considered one of the main reasons for using titanium as an implant. These alloys have better biocompatibility than stainless steel and cobalt-based alloys due to their good corrosion resistance. [2] However, in addition to the good properties mentioned, titanium alloys also have some poor tribological properties due to low resistance to plastic shear, low protection by surface oxides and low hardening. [6] Most of the published literature refers to the alloy Ti-6Al-4V because of its properties. However, there are some issues that limit the long-term use of these commonly used alloys as implants. Some of the disadvantages of these Ti-based alloys are that they lead to loosening of the implant and fracture of the bone due to the stresses being shielded due to the difference in elastic strength between the implant and the surrounding tissue, causing discomfort over a long period of time. [13] Concerns have been raised with the use of aluminium and vanadium as alloying elements regarding their harmful effects following the release of ions into the body, which can cause dermatitis, while in some cases implant rejection occurs. Although Ti-6Al-4V is considered highly resistant to corrosion, no material is completely bioinert. The release of ions can cause allergic reactions in some cases. Vanadium can have both positive and negative effects on the body. Therefore, great efforts have been made to develop titanium alloys with relatively harmless elements. Elements considered safer than aluminium and vanadium include niobium, tantalum and zirconium. Similarly, the release of aluminium and vanadium ions can cause neurodegenerative diseases such as Alzheimer's disease and peripheral neuropathy. It can be deduced that there is a need to explore metals that are better substitutes for alloying elements in Ti-alloys, as well as their properties. [13] With the increasing demand for durable implants, it has become necessary to accelerate research into the development of biomaterials, which should lead to a significant production of implants. [14]

2. Methods of characterizations

The article describes some of the test methods used in the development of titanium alloys. The methods described and explained in the article are characterisation methods using a light microscope (LM), a scanning electron microscope (SEM), an energy- dispersive spectrometer (EDS), X-ray diffraction (XRD), differential scanning calorimetry (DSC) and differential thermal analysis (DTA) methods. The aim of these methods is to characterise materials in order to determine suitable process parameters that will result in an alloy with a satisfactory microstructure or properties desirable for use in the human body.

Two types of microscopy are generally known. These are light microscopy (LM) and scanning electron microscopy (SEM). In light microscopy, the specimen is illuminated with visible light and the image is produced with a system of objectives and eyepieces. Scanning electron microscopy (SEM) is one of the most commonly used instrumental methods to examine and analyse the characterisation of solids containing micro- and nanoparticles. SEM can provide information on surface topography, crystal structure and chemical composition. It is used to obtain a realistic three-dimensional image of the surface of the sample under investigation. One of the reasons why SEM is preferred for particle size analysis is its resolution of 10 nm or 100 Å. The basics of SEM 's work involve scanning the surface of the sample under investigation with a very precisely focused electron beam. The smaller the electron beam, the smaller the surface of the sample and the more accurate the image. Energy dispersion X-ray spectroscopy (EDS) works in conjunction with SEM to provide qualitative and qualitative results. [15]

X-ray diffraction (XRD) is an increasingly important method for the qualitative and quantitative characterisation of crystalline materials. It is a particularly valuable analytical method because it is possible to obtain a large amount of necessary information based on a very small sample. A key feature of qualitative analysis is that the constituents are identified as specific compounds. [16] It provides information on phases, structures and parameters such as crystallinity, average grain size, defects and crystal deformations. It can be said that the sample obtained by this method actually corresponds to a fingerprint, i.e. the periodic arrangement of the atoms of the material under investigation. [17] X-ray diffraction is one of the most important methods for studying and diagnosing atomic structure, particle morphology, phase composition and a number of other structural features. After the discovery of the effects of X-ray diffraction, it has been successfully used to determine the structure of crystalline, conventionally crystalline and amorphous materials, as well as the size and shape of microscopic and submicroscopic particles in liquid and solid states. [18]

The most common methods of thermal analysis are differential scanning calorimetry (DSC) and differential thermal analysis (DTA). Thermal analysis is a method that has continued to develop in terms of new applications in the study of phase equilibria and phase transformation behaviour. [19] These methods have a major impact on materials science as they allow the measurement of a wide range of physical and chemical properties. They are also two closely related methods that analyse the change in temperature difference between a sample and a reference sample while subjected to temperature change and thermal effects in the material. Differential scanning calorimetry is a method in which the change in heat flow difference between a sample and a reference sample is analysed while they are subjected to a temperature change. Differential thermal analysis is a method in which the change in temperature difference between a sample and a reference sample is analysed while they are subjected to a temperature change. The notation of the DTA method is the differential thermocurve or DTA curve. [20] The above methods explain endothermic and exothermic processes at very low (-120°C) to high temperatures (DSC 600°C and DTA 1800°C). Physical properties measured by these methods include crystallisation temperatures, melting transitions, specific heat capacity, enthalpy of melting and crystallisation, liquid crystal transitions, solid-solid transitions, evaporation, sublimation, thermal conductivity and glass transition temperature. Chemical properties monitored by the above methods include oxidative reactions, solid-state reactions, dehydration, decomposition, chemisorption, combustion, hardening and polymerisation. [21] Depending on the measurement method used, a distinction is made between two measurement methods. These are differential scanning heat flow calorimetry (heat flow DSC) and differential scanning calorimetry with power compensation (power compensation DSC). [20, 21]

Ti- alloys

S. Y. Alshamari et al. analysed binary Ti-Cu alloys, i.e. Ti-0.5Cu, Ti-2.5Cu and Ti-5Cu, prepared by vacuum sintering of compacted powders. Using a light microscope, the sintered samples were found to have mostly closed spherical pores in the centre of the samples in the range of 15 to 50 μm. The alloys were sintered at a temperature of 1250˚C, resulting in the formation of spherical isolated pores. This is an indication that the sintered Ti-Cu alloys have reached the final stage of sintering. Since Cu is a stabilizer of the titanium β-phase, its addition leads to the formation of an α+β lamellar structure. Using SEM analysis, they found that there is a microstructural difference in the thickness and amount of β-phase between the different alloys, even when the amount of β-phase present increases. Only the increase in β-phase was determined by the XRD analysis. The XRD patterns of the sintered alloys Ti-2.5Cu and Ti-5Cu show the peaks of β-Ti and Ti_2Cu phases, especially in the Ti-5Cu sample. [22]

P. Pripanapong and colleagues conducted the tests on a Ti-Cu alloy with compositions Ti-2Cu, Ti-4Cu, Ti-7Cu and Ti-10Cu. The samples were sintered at 1000 °C for 1 hour in an argon atmosphere. The microstructure of the investigated alloys shows a 4% Cu alloy, which has a hypoeutectoid structure. The mentioned structure includes primary α-Ti (white phase) and eutectoid phase (lamellae α-Ti/Ti2Cu), which transforms from β-Ti at high temperature. The alloy with 10% Cu has a predominantly eutectoid structure. XRD analysis showed Ti-2Cu peaks corresponding to α-Ti only, while the Ti-10Cu alloy had α-Ti and Ti_2Cu peaks. In the differential thermal analysis (DTA), Ti-15Cu was investigated because the amount of copper added is the largest and it is also easier to detect a possible reaction between titanium and copper powder. The DTA curve showed an exothermic reaction at 1078°C, which is consistent with the melting temperature of pure copper. This compares to the XRD result of the sintered samples. The exothermic peak of the DTA analysis results indicates the formation of Ti2Cu in the alloy after the copper powder was melted. [23]

Algattaan and co-workers added another alloying element, in this case manganese, to the Ti-Cu alloy. Ti-0.5Mn-0.25Cu, Ti-1Mn-0.5Cu, Ti-2Mn-1C, Ti-3.5Mn-1.75Cu and Ti-5Mn-2.5Cu alloys were tested. The XRD diffractograms of the mentioned Ti-Mn-Cu alloys show that the α-phase of titanium is the primary phase forming the alloys. The relative intensity of the β-phase of titanium increases with the addition of a larger amount of alloying elements, as both manganese and copper are elements that stabilize the β-phase of titanium. Accordingly, it is expected that the β-phase of titanium in the microstructure of Ti-Mn-Cu alloys will be more pronounced in heavier alloy compositions. The microstructural analysis results show that the sintered Ti-Mn-Cu alloys have a fully lamellar microstructure composed of almost equal α-Ti grains and parallel α-Ti and β-Ti lamellae, regardless of the alloy composition. With increasing manganese and copper content, the relative amount of β-Ti phases present in the microstructure increases linearly. The higher manganese and copper content increases the fineness of the lamellae and thus decreases the spacing between them. [24]

Xu et al. investigated a biocompatible Ti-28Nb-35.4Zr alloy used as a bone implant. The results showed that the sintering temperatures have a significant influence on the mechanical properties of the alloys. SEM microphotography showed that the atomised powders have a typical spherical shape. XRD analysis showed that the atomised powders consist of a β-Ti, while the spherically milled powders consist of β-Ti and TiO_2. TiO_2 mostly appears because some oxygen is introduced during the ball milling process. The hardness of Ti-28Nb-35.4Zr alloy generally increases with increasing sintering temperature, which significantly improves the mechanical properties of the produced alloy. [25]

Examining Ti-Nb alloys, Haq et al. determined that before the start of heat treatment, the microstructure of the investigated alloy consisted mainly of separated α-Ti grains and Nb grains with a lamellar α- and β-structure at the interface between them. As the heat treatment was performed at 1200°C, the lamellar microstructure started to grow. After 4 hours of heat treatment, the microstructure consisted only of lamellar morphology. The microhardness of the sample increased with increasing heating time. The microstructure had no influence on the change in hardness. The phase change actually played a role in increasing the hardness. [26]

Kalita et al. prepared a Ti-Nb alloy with different chemical composition (Ti-14Nb, Ti-20Nb and Ti-26Nb) using the mechanical alloying method. In XRD analysis of the sintered alloy after sintering, they observed the β-phase. Only a small amount of hexagonal α-phase was present in the samples. Traces of the orthorhombic martensitic α" phase were observed in the Ti-14Nb and Ti-20Nb alloys. In the microstructure of the obtained alloys, β-phase grains with a size of 10-50 μm were observed in the case of the Ti-14Nb alloy. Darker areas of the Nb-depleted α-phase were present at the grain boundaries. It was found that the amount of α-phase decreases with the Nb content. Very bright areas of Nb were also observed. The presence of these particles leads to a decrease in the niobium content in the matrix. XRD analysis was also performed after heat treatment and confirms that the applied heat treatment resulted in a reduced amount of hexagonal α-phase. A regular β-phase was observed in all alloys. A martensite phase was observed within the β-phase grains in the microstructure of these alloys. The temperatures determined by DCS analysis for A_s and A_f were -12.4 and 2.2°C, respectively. There were no visible effects associated with martensitic transformation in the Ti-20Nb and Ti-26Nb alloys. [27]

Zhou et al. prepared three types of Ti-Ta binary alloys (Ti-10Ta, Ti-30Ta, Ti-70Ta). Microscopic analysis showed that the tested alloys have lamellar and acicular microstructure. The SEM analysis showed the formation of passive oxide films on the surface of the samples. Oxide films formed on the surface of the Ti-30Ta alloy. The results of XRD analysis showed that TiO_2 formed on the surface of the Ti-10Ta alloy, while orthorhombic Ta_2O_5 films were present on the surfaces of the other alloys studied. [28]

Elshalakany and colleagues produced five alloys with different compositions (Ti-15Mo-6Zr, Ti-15Mo-6Zr-1Cr, Ti-15Mo-6Zr-2Cr, Ti-15Mo-6Zr-3Cr and Ti-15Mo-6Zr-4Cr). Optical micrographs showed that the Ti-15Mo-6Zr alloy mainly consists of the (α' + β)-phase. After addition of 1 wt%Cr, a small amount of the β-phase was detected. In all Ti-15Mo-6Zr-xCr alloys investigated, the microstructure of the whole alloy was transformed into a granular equiaxed β-phase. As the chromium content increased, the average grain size of the β-phase decreased. Unlike the Ti-15Mo-6Zr-xCr alloy, the microstructure of the Ti-15Mo-6Zr-2Cr alloy appears to consist of β-phase grains. In other words, in the Ti-Cr alloy system, the β-phase can be completely preserved after rapid cooling when the chromium content increases. The average grain sizes of the β-phase decreased with increasing chromium content. The Ti-15Mo-6Zr-2Cr alloy has the highest amount of β-phase and also showed the highest microhardness values (412 HV). [29]

Ho et al. investigated the structure and properties of a series of binary Ti-Mo alloys with molybdenum content ranging from 6 to 20 wt%. The experimental results of XRD analysis showed that the crystal structure and morphology of the cast alloys were sensitive to the molybdenum content. At a Mo content of 6 wt.%, a fine, acicular martensite structure of the orthorhombic α" phase was observed. At a molybdenum content of 7.5 wt%, the entire alloy was dominated by the martensitic α" structure, and when the molybdenum content was increased to 10 wt% or more, the retained β-phase became the only dominant phase. Of all the Ti-Mo alloys, the Ti-7.5-Mo alloy with α"-phase exhibited the lowest hardness. [30]

Luz et al. observed the Ti-40Zr alloy during sintering at a temperature between 800-1300°C. From the microstructure analysis, they determined that the formation of a two-phase (α+β) region started at a temperature of 800°C. The microstructure showed dark areas with titanium particles. Grey areas with dissolved zirconium particles were also visible. The two-phase (α+β) region becomes visible at 1000 °C and consists of a pure zirconium core surrounded by a two-phase microstructure. In the samples sintered at 1300 °C, a fine-plate α- and intergranular β-structure prevailed. Analysis of the results showed that slight additional densification occurs at temperatures above 1300°C. The hardness analysis values showed that as the temperature increases, the hardness value also increases. X-ray diffraction analysis revealed peaks related to the α- and β-phases of titanium, while the peaks of zirconium were not determined, confirming its complete resolution at a temperature of 1300°C. Zirconium-rich regions are present up to 1200°C. [31]

In their study, Slokar et al. produced a $Ti_{90}Zr_{10}$ alloy mixture that was analysed. The SEM analysis of the powders showed different morphologies of the starting powders, for example, the titanium powder consisted of spherical particles with a rough surface and the zirconium powder consisted of angular particles. In addition, a relatively high degree of agglomeration of the titanium particles was observed, as the smallest particles were not separated from the powder. In addition, after grinding $Ti_{90}Zr_{10}$ according to the SEM analysis and the corresponding EDS analysis, it was observed that many smaller particles retained their original shape as the particles were subjected to low energy collisions. In addition, only a small portion of the powder was agglomerated and deformed into flakes. After milling the powders, the EDS line scan confirmed that elemental zirconium remained, indicating that the milling parameters were not satisfactory for complete dissolution of zirconium into titanium. After sintering, a large number of pores were visible that were not spherical, indicating that the final stage of sintering had not been completed. Subsequently, the samples were subjected to SEM and EDS analysis and it was found that the zirconium content in the samples varied, indicating that the mixing of the starting powders was not done correctly. Peaks were only found for Ti and Zr in all the samples, and titanium was seen to be evenly distributed across the analysed range. [32]

Liu et al. investigated the microstructure of the powder metallurgy produced Nb-25Ti-xTa alloy (x = 10, 15, 20, 25, 35 at.%). In the SEM analysis of the alloy, the β-phase was very easy to detect. After sintering at 1700 °C, grain boundaries were clearly observed in the Nb-25Ti-xTa alloy. The average grain sizes were 50 μm, 46 μm and 33 μm. As the Ta content increased, the grain size decreased, while the dissolution rate of Nb and Ta into the Ti matrix increased with increasing sintering temperature. As the sintering temperature increased from 1600 °C to 1800 °C, a gradual transition to the β-phase occurred. It was also found that the acicular α-phase transitioned to the α + β-phase, and when the temperature increased to 1800 °C, a transition to the β-phase occurred. EDS line scanning was then performed to determine the distribution of the elements Nb, Ti and Ta in the Nb-25Ti-25Ta alloy sintered at 1600 °C. Titanium was the main element in the dark areas. As shown by the analysis of SEM, the pore size and shape gradually changed as a function of the sintering temperature. At higher sintering temperatures (1800 °C), there were more pores with regular shape, while at low sintering temperatures (1600 °C), the pores were mostly irregular in shape. XRD analysis of the sintered Nb-Ti-Ta

alloys was also performed and it was found that the predominant diffraction peaks of the sample were from the spatially centred cubic (bcc) β-phase. Due to the small difference between the lattice parameters of Nb and Ta, the diffraction peaks of these elements overlapped. [33]

Popescu and colleagues investigated a new TiZrNbTaFe alloy. Based on the morphology of the starting powders, they found different spherical shapes for each type of elemental powder. They also found that the titanium powder consists of flattened angular particles, for zirconium they are needle-like particles, for niobium they are flaky, while for tantalum irregular particles with a slight tendency to spheroidise and for iron spheroidal particles can be seen. XRD analysis of the homogenised sample revealed that in addition to Ti, Zr, Nb and Fe powder, a combination of these elements with hydrogen or oxygen also occurs, which is due to the high degree of oxidation or hydration of the metal powder. After alloying the mixture for 20 hours, the analysis of SEM showed that the formation of NbTiZr phases was predominant, with some unalloyed powders also visible. Based on the results of the X-ray analysis, it could be assumed that the alloying process had started, but that the milling time was not sufficient to achieve complete mixing of the powders into a homogeneous mixture. Thus, Ti made up 45 % of the powder mixture, Fe 17 %, Ta 12 %, Zr 4 % and the Nb content was 3 %.[34]

3. Conclusion

The excellent properties of titanium alloys have made these alloys a very important material for various applications, especially in biomedicine. Although titanium and titanium alloys are widely used biomedical materials, research continues in order to obtain the highest quality and most reliable material possible. The above overview shows the importance of the presented conventional methods for the development of biomaterials. However, they should be applied together with other characterisation methods in order to be able to adjust the parameters of the biomaterials manufacturing process based on the characterisation results obtained, with the aim of obtaining titanium alloys with satisfactory properties for biomedical applications.

4. References

1. M. Geetha, A.K. Singh, R. Asokamani, A.K. Gogia, Materials Science, **54**, 97-425 (2009).
2. A.J. Festas, A. Ramos, J.P. Davim, Proceedings of the Institution of Mechanical Engineers, Part L, **234**, 1-11 (2019).
3. M. Kaur, K. Singh, Materials Science and Engineering: C,**102**, 844-862 (2019).
4. L.-C. Zhang, L.-Y. Chen, Adv. Eng. Mater., 21, 1-29, 2019.
5. C. S. Pitchi, A. Priyadarshini, G. Sana, S.K. R. Narala, Materials Today: Proceedings, **26**, 3297-3304 (2022).
6. FA Anene, CN A. Jaafar, I Zainol, MA Azmah Hanim, MT Suraya, Proc IMechE Part C: J Mechanical Engineering Science 235, 1-14 (2020).
7. W. Xu, Z. Liu, X. Lu, J. Tian, G. Chen, B. Liu, Z. Li, X. Qu, C. Wen, Science China Materials, **62**, 1-12 (2019).
8. K. Pałka, R. Pokrowiecki, Adv. Eng. Mater., **20**, 1-18 (2018).
9. M. A. Hussein, A. S. Mohammed, N. Al-Aqeeli, Materials, **8**, 2749-2768 (2015).
10. V. S.de Viteri, E. Fuentes, TribologyFundamentals and Advancements, **5**, 1-28 (2013).
11. S. Lascano, C. Arévalo, I. Montealegre-Melendez, S. Muñoz, J. A. Rodriguez-Ortiz, P. Trueba, Y. Torres, Appl. Sci, **9**, 982 (2019).
12. F. Mahyudin, H. Hermawan, Biomaterials and Medical Devices. Vol. 58, Springer International Publishing, **58**, 1-249 (2016).
13. S. Agarwal, J. Curtin, B. Duffy, S. Jaiswal, Mater. Sci. Eng. C, **68**, 948-963 (2016).
14. D. Annur, I. Kartika, S. Supriadi, B. Suharno, Mater. Res. Express, **8** ,1-24 (2021).
15. A. Mohammed, A. Abdullah, Proceedings of 2018 International Conference on Hydraulics and Pneumatics-HERVEX, 1-9 (2018).
16. A. L. Ryland, Journal of Chemical Education, **35**, 1-4 (1958).
17. A. A. Bunaciu, E. G. Udriştioiu, H. Y. Aboul-Enein, Critical Reviews in Analytical Chemistry, **45**, 289-299 (2015).
18. G.V. Fetisov, Physics-Uspekhi, **63**, 2-32 (2020).
19. K. Hildal, Handbook of Thermal Analysis and Calorimetry, **6**, 781-828 (2018).
20. C. Schick, D. Lexa, L. Leibowitz, Characterization of Materials, 1-13 (2013).
21. R. A. Meyers A. Riga, R. Collins, Encyclopedia of Analytical Chemistry, 1-33 (2020).
22. A. Mohammed, A. Abdullah, J. Mech. Behav. Biomed. Mater., (2019).
23. P. Pripanapong, T. Luangvaranunt, Advanced Materials Research, **93**, 99-104 (2010).
24. M. Alqattan, L. Peters, Y. Alshammari, F. Yang, L. Bolzoni, Regenerative Biomaterials, 1-8 (2020).
25. W. Xu, M. Li 1, C. Wen, S. Lv, C. Liu, X. Lu, X. Qu, Materials, **11**, 1-12 (2018).
26. M.A. Haq, S.F. Abbas, N.S.A. EOM, T.S. Kim, B.Lee, K.-T. Park, B.S.Kim, Arch. Metall. Mater., **63**, 1429-1432 (2018).
27. D. Kalita, Ł. Rogal, T. Czeppe, A. Wojcik, A. Kolano-Burian, P. Zackiewicz, B. Kania, J. Dutkiewicz, Journal of Materials Engineering and Performance, **29**, 1445-1452 (2022).
28. Y. L. Zhoua, M. Niinomi, T. Akahori, H. Fukui, H. Toda, Materials Science and Engineering A, **398**, 28-36 (2005).
29. A. B. Elshalakany, S. Ali, A. A. Mata, A. K. Eessaa, P. Mohan, T.A. Osman, V. A. Borras, Journal of Materials Engineering and Performance, **26**, 1262-1271 (2017).
30. W.F. Ho, C.P. Ju, J.H. Lin, Biomaterials, **20**, 2115-2122 (1999).
31. T. dos Rei Luz, V. A. Rodrigues Henriques, J. L. de Oliveira, E. F. Diniz, SAE Technical Paper Series [SAE International 22nd SAE Brasil International Congress and Display - (OCT. 07, 2013)] SAE Technical Paper Series, **1**, 1-6 (2013).
32. Lj. Slokar, A. Štrkalj, Z. Glavaš, Engineering Review, **39**, 115-123 (2019).
33. J. Liu, L. Chang, H. Liub, Y. Li, H. Yanga, J. Ruan, Mater. Sci. Eng. C, **71**, 512–519 (2017).
34. G. Popescu, B. Ghiban, C. A. Popescu, L. Rosu, R. Truscă, I. Carcea, V. Soare, D. Dumitrescu, I. Constantin, M. T. Olaru, B. A. Carlan, Mater. Sci. Eng., **400**, 1-9 (2018).

Study of aluminum content on the structure and phase composition of synthesized aluminum-matrix composites

Yevheniia Kyryliuk, Genadii Bagliuk, Stepan Kyryliuk, Bykov Oleksandr, Yulia Shishkina
Frantsevich Institute for Problems in Materials Science, NASU, Kyiv, Ukraine, 03142, Krzhizhanovsky str., 3

Abstract: *The work shows that there is no significant change in the phase composition of composites with a change in the synthesis temperature, so we can use pre-synthesized heats at a temperature of 950 oC to obtain hot-stamped aluminum-based composites. The best characteristics of the synthesized titanium carbide were obtained for the composition 45Al-11C-44Ti (%, wt.). The lattice period of titanium carbide for this sample is 0.4324, and the particle size of titanium carbide formed after sintering is 0.8-1.5 μm. The influence of the component composition of the initial charge on the features of the structure and the phase composition of the thermally synthesized heat of the Al-C-Ti system was established.*

KEYWORDS: *THERMAL SYNTHESIS, MASTER ALLOY, METAL MATRIX COMPOSITE, ALUMINUM, STRUCTURE, PHASE COMPOSITION, TITANIUM CARBIDE, LATTICE SPACING.*

Today, aluminum matrix composites (AMC) have found the most effective application in automotive, aviation and rocket engineering [1, 2]. This is explained by their low weight, high mechanical, tribotechnical and corrosion properties. The most widely used AMCs are reinforced with ceramic particles, since they have isotropic properties and are made according to a simpler and cheaper technology compared to fibrous and layered aluminum composites. Ceramic powders of aluminum oxide (Al_2O_3) and silicon carbide (SiC) with a size of 10-20 μm with a volume fraction of up to 25% are used as a reinforced phase in most of the manufactured AMCs. However, in recent years, attention has been paid to the use of titanium carbide (TiC) as a dispersion-strengthened phase, since TiC particles can provide AMC with a complex of properties, surpassing all other discretely strengthened AMC [3]. This is due to the fact that TiC has an fcc crystal lattice that coincides with the α-Al crystal lattice, as well as high strength, hardness, and thermodynamic stability. Both powder metallurgy and casting methods are applicable for the production of Al/TiC composites [4]. All these methods can be divided into ex-situ methods, when the reinforced particles are produced in advance, separately, outside the matrix, and then introduced into the matrix during the manufacturing process of the composite, and in-situ methods, when the reinforcing particles are synthesized by chemical reactions directly in the matrix during preparation of the composite. In the case of ex-situ methods, the surface of the powders is usually contaminated with oxides, moisture, adsorbed gases, which impair the wettability of the powders by the matrix and the adhesion between the particles and the matrix. In the case of in-situ methods, the reinforcing particles synthesized in the matrix have a clean, uncontaminated surface, which is important for ensuring strong adhesion to the matrix, they are thermodynamically stable and do not replay with the matrix, they can have a smaller size and a more uniform distribution in the matrix [5, 6], thanks to these advantages, in-situ methods are currently being intensively developed.

Therefore, promising for Al-Ti-C aluminum composites is the direction associated with the preliminary synthesis of titanium carbide in a powder mixture. Depending on the ratio of the content of titanium and carbon in the mixture, when it is heated, in-situ formation of dispersed particles of titanium carbide and ternary titanium carbide occurs, which allows you to control their dispersion and shape. Titanium carbide does not interact with the aluminum matrix and does not form undesirable compounds.

As a result of previous studies [7-10], the authors have accumulated and systematized a certain amount of information on obtaining new composite materials, technologies for preparing powder mixtures (mechanical methods: grinding, chemo-thermal methods: processing in argon and vacuum), consolidation conditions (sintering in controlled gas environments, hot pressing and stamping), which will create new powder composite materials.

The purpose of the work is to study the phase and structure formation of alumino-matrix composite materials strengthened by titanium carbide during their thermal synthesis, as well as to study the influence of the phase composition of composites on the synthesis temperature.

The achievement of the set goal will occur as a result of using the effects of obtaining the required dispersed phases during thermal synthesis, which will allow to purposefully influence the growth rate of grains and artificially create heterogeneity of the composite and thereby form a fine-grained microheterogeneous structure with high physical, mechanical and tribotechnical properties. A new approach in the creation of such powder materials is that refractory reinforcing additives can be formed by recrystallization in thermal synthesis from elementary powders.

Objects and research methods

Aluminum, titanium and graphite powders were used as raw materials for preparing the charge mixture which was subsequently thermal synthesized. To evaluate the effect of blending ratio on the structure and properties of the samples after sintering four compounds of row charge mixtures were chosen. The materials used in this study are summarized in Table 1.

Table 1 *- Chemical composition of charge mixtures for the synthesis of composites*

Number	Composition, % (mass.)		
	Al	C	Ti
1	45	11	44
2	50	10	40
3	55	9	36
4	60	8	32

The initial mixtures were pressed under a pressure of 500 MPa, thermal synthesis was carried out in a vacuum furnace of induction heating at a temperature of 950 ° C and held for 1 hour with a sintering rate of 5-10 degrees./ min. Composites was studied using a scanning electron microscope with an energy-dispersive microanalyzer REM 106i, which allows obtaining images of the structure with high spatial resolution and depth of field in reflected (BSE) and secondary (SE) electrons, as well as provides information about the chemical composition and structure. Etching of the samples was performed in a 40% NaOH solution. Microspectral analysis, X-ray phase analysiscand differential thermal analysis (DTA) was also performed.

Results and discussion

The composition of powder mixtures used for the synthesis of Al-Ti-C composites is shown in Table. 1. as a result of synthesis, the initial samples (fig. 1. b, c) turned into fairly strong and relatively dense compacts. After sintering, there was no significant increase in volume and no change in the shape of the compacts due to thermal synthesis at a low heating rate of 5-10 degrees/min. The

advantage of this method is the production of dispersed particles of titanium carbide in the aluminum matrix as a result of the in-situ reaction between the original elementary powders of Al, Ti and C. It is assumed that as a result of the in-situ reaction during the synthesis of the material, the intergrain boundaries between the particles of the strengthening phase and aluminum will be free from oxides, which significantly increases the interfacial strength, and the titanium carbide particles themselves will have a submicron size and a fairly homogeneous volume distribution, which leads to an increase in the mechanical properties of the composite [11, 12].

By adjusting the heating rate, the final porosity of the synthesized compacts can be controlled. The porosity of the synthesized composites varies from 8 to 25%, depending on the aluminum content (45-60% by mass) and the sintering rate from 5 to 10 degrees/min.

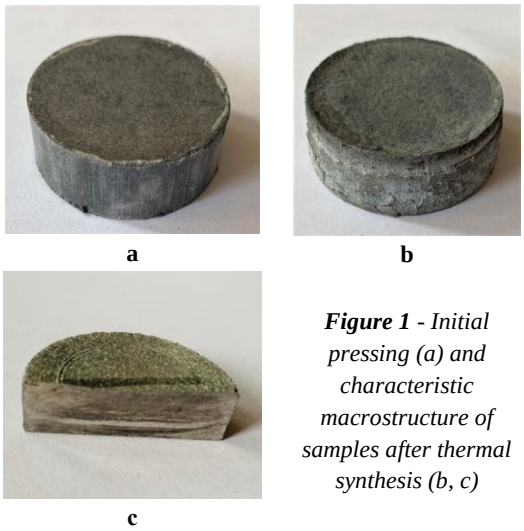

a **b**

c

Figure 1 *- Initial pressing (a) and characteristic macrostructure of samples after thermal synthesis (b, c)*

The results of scanning electron microscopy (SEM) of the samples after thermal synthesis presented in Figure 2 and show that the studied samples have mainly a two-phase structure - a gray field, on which light small particles are evenly distributed. It should be noted that the number of light particles significantly decreases with the increase in the amount of aluminum in the samples.

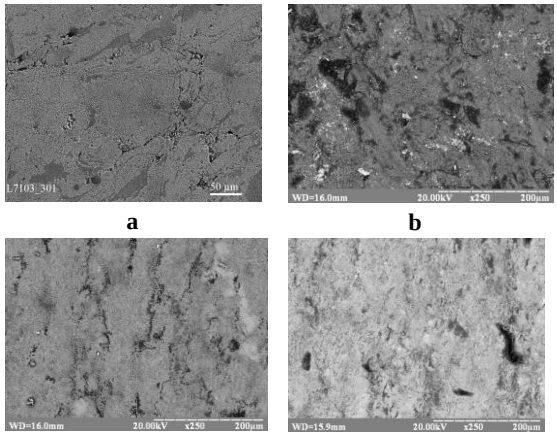

a **b**

c **d**

a – 45Al-11C-44Ti (%, мас.); b – 50Al-10C-40Ti (%, мас.); c – 55Al-9C-36Ti (%, мас.); d – 60Al-8C-32Ti (%, мас.)

Fig. 2 *- SEM microstructure of Al-Ti-C composites after thermal synthesis*

Quantitative analysis showed that the gray field in the photographs of microstructures (Fig. 3) consists mainly of aluminum (Table 2, spectra 2), or a mixture of aluminum and titanium carbide particles (spectra 4, 7-10), light rounded particles (spectra 3, 5 and 6) correspond to the close to stoichiometric composition of titanium carbide. In addition, an increase in the amount of aluminum from 45 to 60% leads to an increase of oxygen in the samples, the percentage of which gradually increases in the samples 55Al-9C-36Ti (%, wt.) and 60Al-8C-32Ti (%, wt.).

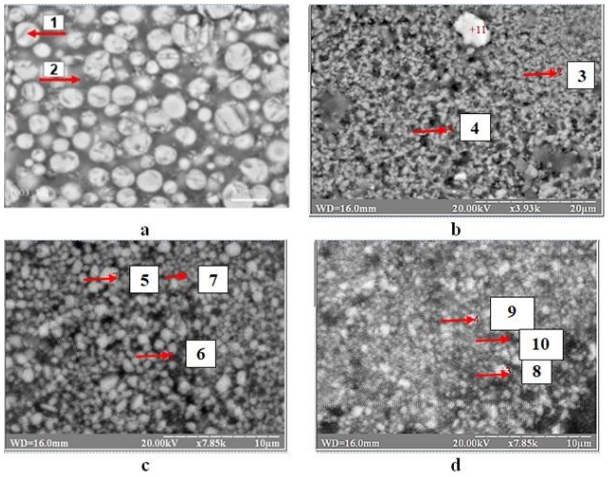

a **b**

c **d**

a – 45Al-11C-44Ti (%, мас.); b – 50Al-10C-40Ti (%, мас.); c – 55Al-9C-36Ti (%, мас.); d – 60Al-8C-32Ti (%, мас.)

Fig. 3 *-.SEM microstructure of Al-Ti-C composites after thermal synthesis*

Table 2 *- Content (wt.) of elements at different points synthesized ligatures of the Al-Ti-C system (see Fig. 2)*

№ spectrum	Al, %	Ti, %	C, %	O,%
1	30,33	60,36	9,3	-
2	55,1	44,1	3,86	-
3	15,48	47,01	24,26	13,25
4	30,91	26,18	31,36	11,55
5	8,94	55,40	22,70	12,97
6	20,56	45,38	16,33	17,73
7	21,5	41,60	23,66	13,24
8	35,75	25,06	20,57	19,62
9	35,91	30,13	17,52	16,44
10	45,19	23,52	18,07	13,20

The dispersion of titanium carbide particles in the sample with the composition 45Al-11C-44Ti (%, wt.) lies in the range from 0.8 to 1.5 μm (Fig. 3, a), which is less than in other samples in which the grain size 2-4 μm, respectively (Fig. 3, b - d).

This is explained by the different content of aluminum: the greater its amount surrounds the titanium carbide particles formed in the synthesis process, the larger the diffusion path becomes and the smaller the driving force that promotes the growth of the particles.

Fig. 4 presents the XRD pattern of initial mixture and composites. It can be seen that the initial mixture contains Al, Ti and C as shown in Fig 4a. The XRD results revealed the presents of TiC and Al in all specimens Fig 4 (b, c, d, e)

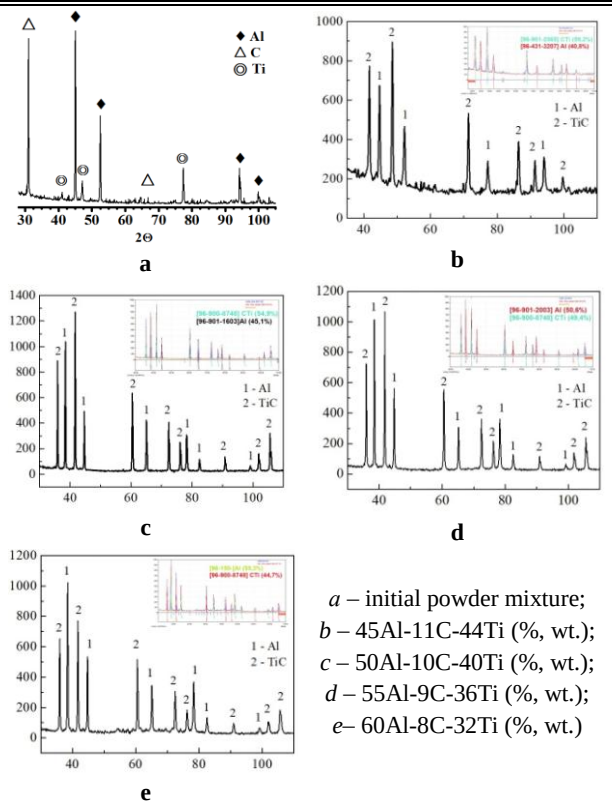

a – initial powder mixture;
b – 45Al-11C-44Ti (%, wt.);
c – 50Al-10C-40Ti (%, wt.);
d – 55Al-9C-36Ti (%, wt.);
e– 60Al-8C-32Ti (%, wt.)

Fig. 4 *- Diffraction patterns of the initial powder mixture (a) and synthesized Al-Ti-C master alloys (b, c, d, e)*

The influence of the aluminum content on the parameters of the titanium carbide lattice was investigated (Fig. 5). In all samples, the diffraction lines of titanium carbide are at approximately the same angle, which explains the close values of the period of the TiC lattice (Fig. 5).

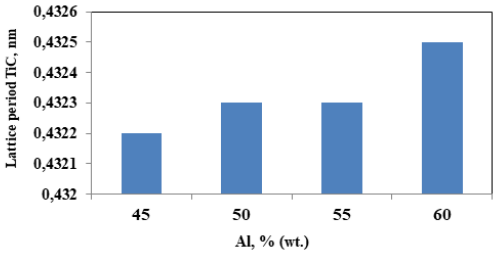

Fig. 5 *- The value of the period of the TiC lattice on the content of aluminum in composites*

However, it should be noted that with an increase in the amount of aluminum in the samples, it can be seen that the value of the lattice period increases. The low value of the period of the TiC lattice may be related to too little amount of aluminum, which in this system at the synthesis temperature of 950 ºC is an environment that facilitates the interaction between titanium and carbon, and its deficiency affects the completeness of the carbide formation reaction.

The differential thermal analysis of the studied systems showed that for all compositions of the initial mixtures, the DTA curves have pronounced endothermic and exothermic peaks (Fig. 6). For samples with a content of 50 and 60 wt. %. aluminum, the minima of the endothermic and the maxima of the exothermic peaks practically coincide (at temperatures of about 640 °C and 800 °C, respectively). In a sample with a content of 45 wt. % of aluminum, endothermic peaks with minima at 635°C are observed, and exothermic peak maxima correspond to temperatures of 812 °C and 800 °C. The endothermic effect at temperatures of 635 - 675 °C is explained by the appearance of a liquid phase. The exothermic peaks on the DTA curves at 800 °C and 812 °C correspond to the in-situ formation of titanium carbide as a result of the solid-phase interaction of titanium with carbon, where the aluminum melt acts as a medium that intensifies the formation of titanium carbide. Based on the fact that this reaction is one of the most thermodynamically advantageous, it can be assumed that the formation of titanium carbide proceeds in this way. The temperature of formation of TiC on DTA may be underestimated, because measurements of a small mass were used for the research. During the synthesis of ligatures, heating of the presses to an average of 1100 °C was recorded.

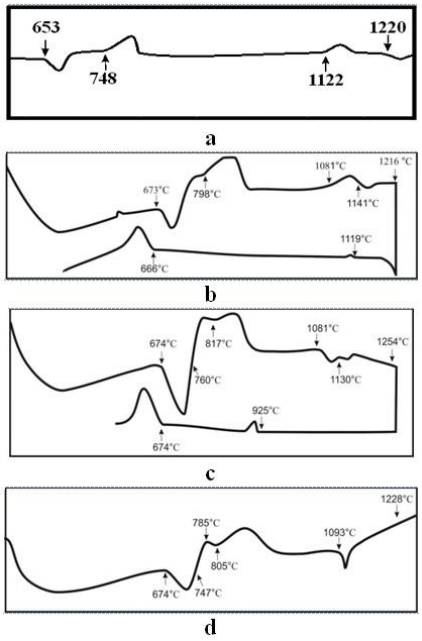

a – 45Al-11C-44Ti (%, мас.); *b* – 50Al-10C-40Ti (%, мас.);
c – 55Al-9C-36Ti (%, мас.); *d* – 60Al-8C-32Ti (%, мас.)

Fig. 6 *-.Differential thermal analysis of Al-Ti-C powder mixture*

Thus, the results of microspectral analysis, X-ray phase analysis, and differential thermal analysis of samples obtained by thermal synthesis from powder mixtures of different compositions made it possible to establish that for all investigated compositions of the starting mixtures, when they are heated, in-situ separation of TiC titanium carbide particles occurs. The alloys synthesized from a mixture of the compositions 45Al-11C-44Ti (%, wt.) and 50Al-10C-40Ti (%, wt.) are characterized by the greatest dispersion of the particles of the strengthening phase, which were chosen for obtaining aluminum composites by the method of hot stamping, together with the sample composition 60Al-8C-32Ti (%, wt.), in which complex titanium carbide appears.

Conclusions

1 The results of microspectral analysis, X-ray phase analysis, and differential thermal analysis of samples synthesized from powder mixtures of different compositions made it possible to establish that for all the compositions of the initial mixtures, upon

heating, in-situ formation of TiC titanium carbide particles and a small amount of titanium aluminides occurs.

2. It is shown that there is no significant change in the phase composition of the composites with a change in the synthesis temperature, therefore, in the future, we can use pre-synthesized heats at a temperature of 950 °C to obtain hot-forged aluminum-based composites. The best characteristics of the synthesized titanium carbide were obtained for the composition 45Al-11C-44Ti (%, wt.). The lattice period of titanium carbide for this sample is 0.4324, and the particle size of titanium carbide formed after sintering is 0.8-1.5 μm.

3. The influence of the component composition of the initial charge on the structural features and phase composition of the thermally synthesized heat of the Al-C-Ti system was determined. It is shown that in the case of using a charge with a stechiometric carbon content in relation to titanium, the predominant strengthening phase of the alloy is titanium carbide.

References

1. *Kainer K.U.* Metal Matrix Composites // Weinheim, Germany: Verlag GmbH & Co. KGaA, 2006.

2. *Adebisi A.A., Maleque M.A., Rahman Md.M.* Metal matrix composite brake rotor: historical development and product life cycle analysis. International Journal of Automotive and Mechanical Engineering. – 2011. - Vol. 4. - p. 471 – 480.

3. *Амосов, А.П., Луц А.Р., Латухин Е.И., Ермошкин А.А.* Применение процессов СВС для получения in-situ алюмоматричных композиционных материалов, дискретно армированных наноразмерными керамическими частицами: обзор // Изв. Вузов. Цветная металлургия. - 2016. - №1.- С. 39-49

4. *Rana R.S, Purohit R., Das S.* Review of Recent Studies in Al Matrix Composites // International Journal of Scientific Engineering and Research. – 2012. - Vol. 3. – P. 1-16

5. *Kennedy A.R and Wyatt S.M.* Characterising particle–matrix interfacial bonding in particulate Al–TiC MMCs produced by different methods // Composites Part A: Applied Science and Manufacturing. – 2001. - Vol. 32. – Issues 3-4. - P. 555 – 559.

6. *Das B., Roy S., Rai R.N., Saha S.C.* Development of an in-sity synthesized multi-component reinforced Al – 4.5%Cu-TiC metal matrix composite by FAS technique – Optimization of process parameters // Eng. Sci. & Technology, an International Journal.– 2016. - Vol. 19 (1). –P. 279 – 291.

7. *Баглюк, Г.А., Шишкина Ю.А.* Новые композиционные дисперсно-упрочненные материалы на основе алюминия // Технологические системы. – 2011. – № 4 (57). – С. 36-43.

8. Shishkina Y., Baglyuk G., Mamonova A., Tihonova I. Specific features of structure formation in Al-Ti-C powder master alloys after thermal synthesis // International Scientific Journal «Machines. Technolo Materials». – 2012. – Vol. 12. – P. 45-49.

9. Shishkina, Y.A. Baglyuk G.A., Mamonova A.A., Tikhonova I. B. Effect of carbon and aluminum contents on the structurization of Al–Ti–C powder master alloy during reaction synthesis // International Scientific Journal «Machines. Technologies. Materials». – 2013. – Vol 52. – No 3-4. – P. 154–160.

10. *Богачева А.Г. Баглюк Г.А., Шишкина Ю.А.* Получение и свойства дисперсно-упрочненных легких сплавов / А.Г. Богачева, // Технологические системы. – 2013. – № 6 (64). – С. 23-38.

11. *Луц. А. Р.* Самораспространяющийся высокотемпературный синтез модифицирующих лигатур и композиционных сплавов в расплаве алюминия с применением флюсов: автореф. дис**.** канд. техн. наук: 01.04.17 / А. Р. Луц. – Самара, 2006. – 25 с.

12. *Савицкий А. П.* Современные представления о спекании в жидкой фазе // А. П. Савицкий / Порошковая металлургия. – 1987. – №8. – с. 35-41.

Eco-inspired synthesis and photocatalytic application of novel ZnO nanoparticles from peel extract of banana

Daniela Šojić Merkulov*, Sabolč Bognar, Nina Finčur, Dušica Jovanović
University of Novi Sad Faculty of Sciences, Department of Chemistry, Biochemistry and Environmental Protection,
Trg Dositeja Obradovića 3, 21000 Novi Sad, Serbia
daniela.sojic@dh.uns.ac.rs

Abstract: *The time being, one of the greatest concerns is the environmental pollution. Nowadays, various dangerous compounds reach to the air, soil and water. Pharmaceuticals, such as 17α-ethinylestradiol (EE2), are one of the most emerging pollutants in water ecosystems. Hence, powerful but green approaches should be developed in order to completely remove the pollutants. Heterogeneous photocatalysis is a sustainable and efficient process in the removal of organic pollutants, such as pharmaceuticals. ZnO is one of the most commonly used semiconductors but also possess some drawbacks. In this study novel synthesis pathway of ZnO nanoparticles from banana peel extract was obtained. Besides, the photocatalytic efficiency of the newly synthesized ZnO was examined in the degradation of EE2. Both the eco-friendly ZnO nanoparticles, as well as pure banana peel extract showed a promising photocatalytic activity in the degradation of EE2 under simulated solar irradiation (SSI). Namely, EE2 was completely degraded after 60 min of SSI.*
Keywords*: ENVIRONMENTAL POLLUTION, SUSTAINABLE WASTEWATER TREATMENT, ADVANCED OXIDATION PROCESSES, HETEROGENEOUS PHOTOCATALYSIS, GREEN SYNTHESIS, ZNO NANOPARTICLES, BANANA PEEL EXTRACT.*

1. Introduction

Nowadays, various dangerous compounds reach to the air, soil and water. Environmental pollution is an emerging global issue, with severe impact on natural fields. The water contamination is the second most serious problem, right after the air pollution [1]. Even though all natural ecosystems are exposed to the harmful effects of different pollutants, the water pollution is the most emerging one. Each year, about 380 billion m^3 of wastewater is released to the aquatic environment and this amount is expected to be increased by 24% until 2030 [2].

Pharmaceuticals, such as 17α-ethinylestradiol (EE2), are one of the most emerging pollutants in water ecosystems. EE2 is a synthetic steroid estrogen and commonly applied in controlling ovulation, as well as in treating alopecia, prostate and breast cancer in humans and reproductive disorders. Furthermore, it is also applied in contraceptives and in hormone replacement therapy. Even though this compound can be successfully used for different medical purposes, the human organism cannot it completely use and it can be excreted in the biologically inactive formulation, such as sulfate and glucuronide conjugates, but also as free active molecules. EE2 belongs to the group of endocrine disruptors and has been globally detected at concentrations ranging from 0.3 to 84.0 ng/L in surface water, sanitary sewage, and drinking water and wastewater effluents from sewage treatment plants. Unfortunately, even at low concentrations EE2 can cause serious damages to the living organisms. Several destructive wildlife and human diseases are believed to be caused by EE2. For instance, fish feminization, turtle egg production alterations, functional digestive gland alterations in mussels and also prostate cancer and decreased sperm production in human males [3,4].

Another serious issue is the ineffectiveness of the most commonly used conventional wastewater treatment techniques, which also use harmful chemicals. Hence, powerful but green approaches should be developed in order to completely remove the pollutants.

Advanced oxidation processes (AOPs) are considered to be adequate alternatives. Heterogeneous photocatalysis, as one of the AOPs, is a sustainable and efficient process in the removal of organic pollutants, such as pharmaceuticals [5]. This technique is based on the interaction between semiconductors as photocatalysts and sunlight. As a result, reactive oxygen species are generated, which attack and mineralize the present pollutants. ZnO is one of the most commonly used semiconductors but also possess some drawbacks, which limit its application in photocatalysis. Thus, various ZnO nanoparticles are being synthesized with unique characteristics [6].

The aim of this study was to prepare novel green ZnO nanoparticles from banana peel extract. In addition, the photocatalytic efficiency of the newly synthesized ZnO and pure banana peel extract was examined in the degradation of EE2 under simulated solar irradiation (SSI).

2. Materials and methods

The aqueous solution of EE2 (0.05 mM) was prepared by dissolving appropriate mass in ultrapure water. The solution was stored in dark environment (protected from light) at room temperature.

The synthesis of the novel-green ZnO nanoparticles (ZnO NPs) was conducted using banana-peel-based extract. Banana was obtained from local stores.

Firstly, prior to the ZnO synthesis, the banana peel was washed several times with tap, distilled and ultrapure water. After that, 220 g of washed peel was mixed with 400 mL ultrapure water. The mixture was heated until boiling and cooked for 10 min. Finally, 100 mL of pure extract was separated and stored in a refrigerator for further analyses.

In the eco-friendly synthesis of novel ZnO NPs, $ZnSO_4 \times 7H_2O$ (Sigma−Aldrich, St. Louis, MO, USA) was used as a precursor. To begin with, 300 mL banana peel extract was mixed with 1500 mL $ZnSO_4$ (0.08 M) solution. Then, the pH was set to 10, using 3 M NaOH. During the addition of NaOH, snow-white precipitation was observed, which is proved the formation of ZnO nanoparticles. The mixture was filtrated through a Büchner funnel and the precipitation was collected on a filter paper. The newly-formed ZnO NPs were washed (two times) with ultrapure H_2O, until pH 7. Finally, ZnO nanoparticles were dried in an oven at 100 °C, until constant mass.

3. Analytical procedures

The photodegradation experiments were performed in a photoreactor (TOPT-V, Toption, China). The samples were prepared and irradiated in a photochemical cell made of quartz glass (total volume of ca. 100 mL). The photochemical cells were placed in a circle around the Xe lamp, which was used as simulated solar irradiation. The cells were equally exposed to the irradiation source. Xenon lamp was in a quartz cold trap, which was equipped with water-circulating jackets and connected to a cooler in order to ensure a constant temperature inside the photoreactor (Fig. 1).

The samples of EE2, taken after different times of irradiation using simulated solar irradiation, were firstly filtered through Millipore (Millex-GV, Burlington, MA, USA, 0.22 μm) membrane filter to remove all possible impurities. After that, they were analyzed using high-pressure liquid chromatograph with fluorescence detector (UFLC-FL, Shimadzu Nexera, Tokyo, Japan)

(excitation and emission wavelength of EE2 were 220 nm and 310 nm, respectively) equipped with Inertsil® ODS-4 column (2.1 mm × 50 mm i.d., particle size 2 µm, 30 °C) was used. Prepared samples (10 µL) were injected and analyzed. The mobile phase (flow rate 0.7 mL/min) was a mixture of acetonitrile and water (80:20, v/v, pH 2.56), while the water was acidified with phosphoric acid, so that the mass fraction of phosphoric acid was 0.1%.

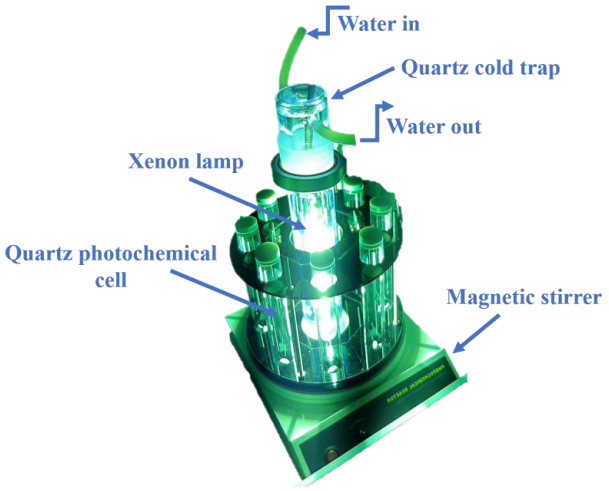

Fig. 1. *TOPT-V photoreactor*

4. Results and discussion

In order to determine the photocatalytic activity of newly synthesized plant-based ZnO nanoparticles, the photocatalytic degradation efficiency of EE2 was investigated. Firstly, experiments were carried out in the presence of both commercially available ZnO and novel green ZnO NPs. Based on the obtained results (Fig. 2) it can be concluded that banana-peel-based ZnO showed higher photocatalytic activity, since 95% of EE2 was degraded after 60 min of simulated solar irradiation. On the other hand, in the system with commercial ZnO 91% of EE2 was removed, respectively.

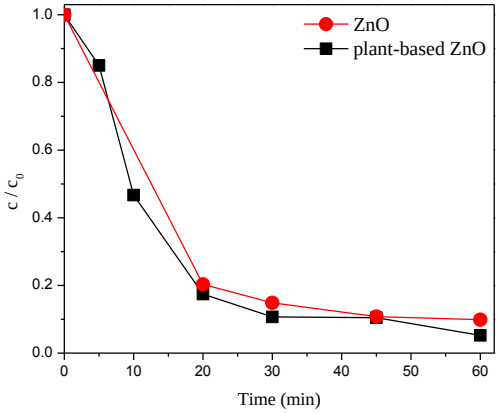

Fig. 2. *Kinetics of EE2 (0.05 mM) degradation in the presence of commercial and plan-based ZnO (γ = 1.0 mg/mL), under simulated solar irradiation*

Considering that the novel green ZnO NPs showed the highest removal efficiency, they were used in further experiments. Moreover, the efficiency of pure banana peel extract in the photodegradation of EE2 was also examined. According to the obtained data (Fig. 3), it can be seen that the removal of EE2 was slightly improved in the presence of banana peel extract, compared to the system with ZnO NPs. Namely, 98% of EE2 was successfully degraded in the presence of banana extract, after 60 min of solar irradiation.

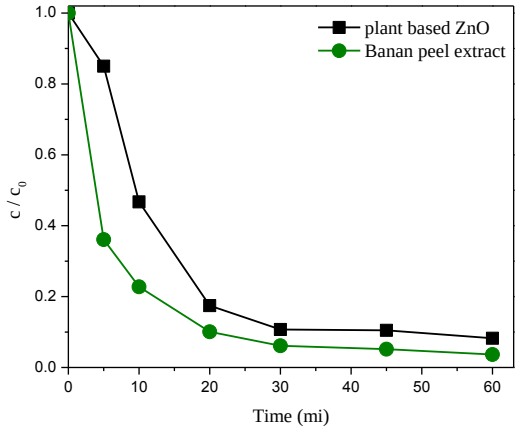

Fig. 3. *Kinetics of EE2 (0.05 mM) degradation in the presence of plan-based ZnO (γ = 1.0 mg/mL) and pure banana extract (5%, v/v), under simulated solar irradiation*

5. Conclusion and outlooks

Banana-peel-based ZnO nanoparticles were successfully synthesized via precipitation method with $ZnSO_4 \times 7H_2O$ as a precursor.

Based on the conducted experiments on the photodegradation of EE2, we successfully proved the possible water remediation application of the newly synthesized ZnO-based nanomaterials, as well as banana peel extract.

In general, the phytochemicals present in natural extracts act as reducing and capping agents, thus the synthesis procedure can be accomplished without using the expensive toxic organic stabilizers and complicated time-consuming procedures. Moreover, the plant extracts used for the sustainable synthesis can additionally improve the photocatalytic activity, because of the biomolecules and other natural compounds present in them. However, the exact effects of the biomolecules obtained from plants in the synthesis of nanoparticles, as well as in the photocatalytic processes, are not exactly known and require further investigation.

6. Acknowledgement

The authors acknowledge the financial support of the Science Fund of the Republic of Serbia (Grant No 7747845, *In situ* pollutants removal from waters by sustainable green nanotechnologies-CleanNanoCatalyze).

7. References

1. P. O. Ukaogo, U. Ewuzie, C. V. Onwuka, Environmental pollution: causes, effects, and the remedies, in: P. Chowdhary, A. Raj, D. Verma, Y. Akhter (Eds.), Microorganisms for Sustainable Environment and Health, Elsevier Inc., 2020, pp. 419−429.
2. UNESCO, UN-Water, 2020: United Nations World Water Development Report 2020: Water and Climate Change, Paris, UNESCO.
3. D. Ren, F. Chen, Z. Ren, Y. Wang, Process Saf. Environ. Prot. **121** (2019), 367−373.
4. F. P. Chaves, G. Gomes, A. Della-Flora, A. Dallegrave, C. Sirtori, E. M. Saggioro, D.M. Bila, Sci. Total Environ. **746** (2020), Art. No. 141041.
5. A. Santos, S. Rodríguez, F. Pardo, A. Romero, Sci. Total Environ. **563−564** (2016), 657−663.
6. S. Bognár, P. Putnik, D. Šojić Merkulov, Nanomaterials **12** (2022), Art. No. 263.

The influence of electrochemical corrosion on the structure and phase composition of a sintered multicomponent titanium-based composite in a 3% NaCl solution

Oksana Baranovska[1], Gennadii Bagliuk[1], Oleksandr Bykov[1], Oleksandr Hrypachevsky[2], Viktor Talash[1], Yulia Rudenko[1], Dmytro Baranovskyi[1]

Frantsevich Institute for Problems in Materials Science[1], Kurdyumov G.V. Institute for Metal Physics[2] of the NASU, Kyiv, Ukraine, 03142
E-mail: ksenya.suprun@gmail.com, gbag@ukr.net

Abstract: *The electrochemical corrosion properties in a 3% NaCl solution of the titanium-based multicomponent composite of the 65TiH_2–30FeSiMn–B_4C system were investigated. The kinetics and the mechanism of anode dissolution of metals and oxidation of specimens have been studied by using polarization curves, chemical and x-ray phase analyses. It was found a decrease in the titanium carbide peaks on the X-Ray defractions also the titanium silicon carbide almost disappears after immersing the sample in a 3% NaCl solution. Formation of silicon and boride phases of titanium in the synthesis process leads to an increase in corrosion resistance due to the inhibition of the velocities of both the anode and cathode processes.*

KEYWORDS*: POWDER MATERIALS, ELECTROCHEMICAL CORROSION, POLARIZATION CURVES, TITANIUM SILICON CARBIDE, TITANIUM CARBIDE*

1. Introduction

For the successful development of modern technology, it is necessary to create new materials that can work in extreme conditions and possess of physical and technical properties: refractory, heat resistance, wear resistance, resistance to aggressive environments.

Titanium and titanium-based materials are among the stable materials in many aggressive environments, especially in the electrochemical corrosion, for example, in the marine environment or in the wastewater environment. Which is caused by the rapid formation of a titanium thin inert film of dioxide on its surface, which interacts with the lower layer of titanium with the formation of lower oxides soluble in the metal.

In recent years, powder metallurgy methods have been increasingly used for the production of titanium materials [1-3]. One of the effective options for obtaining sintered titanium-containing materials is the use of titanium hydride powders instead of serial titanium powder as raw materials [4,5].

In [6], the results of the electrochemical corrosion test of three-layer ceramics based on Ti_3SiC_2 are presented. Titanium silicon carbide is highly stable in concentrated hydrochloric acid solution and exhibits high crystalline hydrogen evolution activity. In [7] Ti_3SiC_2 exhibits excellent tribocorrosion resistance *in situ* due to the formation of an oxide film on the surface was found, unlike pure titanium. Thus, it can be concluded that Ti_3SiC_2 can have very wide prospects for the use in seawater as a substitute for non-corrosive components. However, obtaining titanium silicon carbide requires the use of many technological operations [8], as well as the use of pure powders of titanium, silicon and graphite as raw materials, which significantly increase the price of the finished product.

The appropriateness of choosing an alloying element to obtain our multicomponent material is determined by technical and economic factors. Thus, the introduction of up to 3÷5% of iron, silicon or manganese into the composition of the powder charge significantly increases the strength of the sintered alloy. In addition, during the synthesis of titanium hydride with ferro-silicon-manganese, there is an active interaction with the formation of hard and wear-resistant silicide phases of titanium, which favorably affect corrosion resistance in sea water and sulfuric acid. Additional introduction of boron, carbon, or nitrogen transition metals to IV-VI groups makes it possible to obtain a composite material with a combination of unique electrophysical and mechanical properties, while having chemical and thermal stability [9,10].

A number of interesting temperature and mechanical properties of borides, for example, a high melting point and high hardness, have already been studied and successfully exploited in such areas as wear-resistant products. Composite materials that include borides make it possible to use them in high-tech areas, along with well-known oxide ceramic materials, as well as silicon carbide and hard alloys [11].

Considering the above, ***the aim*** of this paper is to study the influence of a 3% NaCl solution on the stability of a multicomponent titanium based composite doped with ferrosilicomanganese and boron.

2. Objects and research methods

As the base of charge, we used powders of PTKh-80 titanium hydride with a particle size of ≤ 63μm. The main alloying elements were added to the charge in the form of MnS-17 ferro-silicon-manganese (FSM) powder with a particle size of ≤ 80 μm the chemical composition of which is given in the table 1 and boron carbide with a particle size ≤ 50 μm. The morphology of the powders of the initial charge is shown in Fig. 1.

Table 1: Chemical composition of Ferro-Silicon-Manganese MnS-17 (%, wt.)

Mn	Si	Fe	C
62,5	14,1	21	2,1

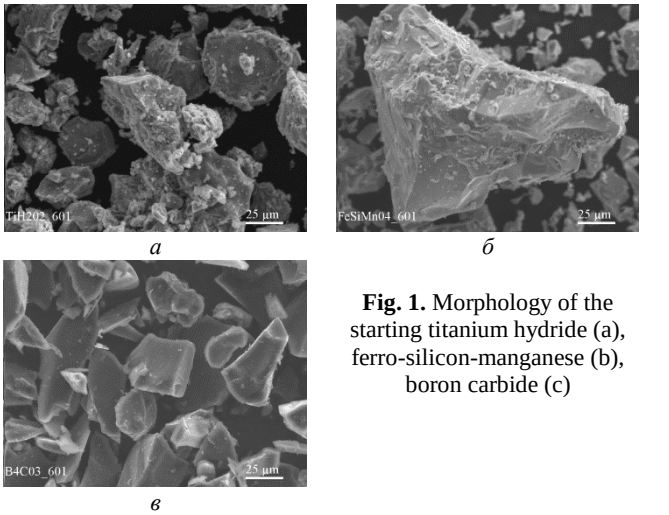

а *б* *в*

Fig. 1. Morphology of the starting titanium hydride (a), ferro-silicon-manganese (b), boron carbide (c)

The initial powder mixture was mixed in a ball mill in an alcohol for 6 hours with grinding carbide balls (diameter of 4–12 mm) and a ratio of the mass of the mixture to the mass of the balls of 1:5.

Samples of size 43×6×6 mm were pressed from the obtained mixture under a pressure of 500 MPa. The test samples were sintered in a vacuum furnace type СШВЛ - 1.2,5/25-М04 with a heating rate of 5-7 degrees/min in two successive stages: heating to 600 ^oC with isothermal holding for 30 min (to remove the main amount of hydrogen), further heating to 1250 ^oC with exposure for 60 min.

The microstructures of the starting powders after mechanoactivation was examined employing REM-106Y scanning electron microscope.

The change in the local chemical composition of the samples was studied by X-ray spectral analysis using the MS-46 "Cameca" microprobe. The phase composition was determined by X-ray defraction in filtered Co-K_α ($\lambda = 0.15418$) radiation using a DRON-3M diffractometer. The diffractograms were processed using the ORIGIN 2016 program to determine the reflection angles and lattice parameters. The phase composition of the samples was determined by the intensity distribution along the diffraction vector.

The process of electrochemical oxidation of the material was carried out by the method of obtaining anodic polarization curves with a potential sweep speed of 0.5 mV/s on a PI-50-1 potentiostat in a 3% NaCl solution. A platinum electrode was used as a cathode; anode potentials were measured using a silver chloride reference electrode. The studied sample was not subjected to grinding before the test due to high fragility.

3. Results and discussion

Figure 2 shows the schematic of a cathodic and anodic polarization curve after electrochemical oxidation of the synthesized TiH2-FeSiMn-B4C in 3% NaCl solution.

It is known [12] that during anodic oxidation of binary compounds of transition metals, the formation of a wide range of oxides should be expected. This is especially characteristic of titanium, which forms compounds with different degrees of oxidation.

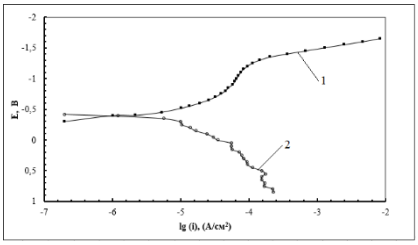

Fig. 2. *Cathodic (1) and anodic (2) polarization curves of the 65TiH2-30FeSiMn-5B4C composite in a 3% NaCl solution*

As can be seen from curve 2 (Fig. 2), in the initial range of potentials from stationary (Est = -0.42 V) to -0.3 V, active anodic oxidation is observed, which is accompanied by its dissolution in the electrolyte with transition to a solution of Ti^{3+} ions. On the basis of curve 2 (see Fig. 2), the following anodic process on the TiB surface can be proposed: in the range of potentials Est = - 0.3 V, Ti^{3+} ions and boric acid ions pass into the solution:

$$TiB + 3H_2O = Ti^{3+} + BO_3^{3+} + 6H+ + 6e^- \quad (1)$$

With the development of the anodic process, passivation of the sample with the formation of a TiO2 (rutile) film is observed at potentials more positive than -0.3 V, which is evidenced by the changed slope of the polarization curve:

$$TiB + 5H_2O = TiO_2 + BO_3^{3+} + 10H^+ + 7e^- \quad (2)$$

The cathodic recovery process (curve 1), which occurs on the surface of the sample, proceeds as actively as the anodic process. According to the course of the curves, the rate of corrosion is controlled by the course of reactions (1) and (2), i.e., the value of the limit oxygen current.

Taking into account that electrochemical reactions occur on the surface of the material, the nature of the distribution of phases and their composition, which are in direct contact with the aggressive environment, is important. For this purpose, the microstructure and surface composition of the material before and after oxidation were investigated. The material 65TiH2/30FeSiMn/B_4C has a heterophase microstructure based on grains of titanium carbide, titanium silicide, titanium boride, a matrix in the form of a Ti-Mn compound and some amount of ternary carbide Ti_3SiC_2. X-ray phase analysis is presented in Fig. 3.

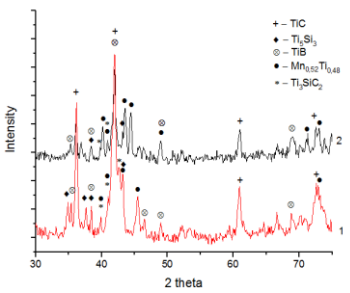

Fig. 3. *Fragment of the X-ray diffraction pattern of an alloy synthtesized at 1250°C from the TiH_2-FeSiMn-B_4C: 1 – sample after synthesis, 2 – sample after synthesis immersed in a 3% NaCl solution*

Based on the X-ray diffraction pattern (Fig. 3(1) before the sample is immersed in a 3% NaCl solution), the matrix phase is presented in the form of the Ti–Mn system, there is a significant number of clear lines of silicide phases (Ti_5Si_3). The main phase is titanium carbide, which is located at angles of 36°; 42°; 61° and 73°, whose diffraction maxima are (111), (200), (220), (311), respectively. Reflexes of titano-silicon carbide Ti_3SiC_2 and some amount of TiB were also observed.

After immersing the sample in 3% NaCl (Fig. 3(2)), the diffraction pattern changes slightly: a decrease in the intensity of the carbide peaks is observed. The most intense reflection (200) is almost halved from 100.0 to 58.3, probably due to the formation of a passivation film. Titanium silicon carbide almost disappears and the amount of silicide phase decreases. As noted in [6], the decrease in the number of these phases indicates that most of the Ti and Si atoms in the lattice are selectively dissolved in the solution, and carbon remained in free form. The chemical bond between the Si and Ti–C layer was very weak, and the electrical conductivity could be mostly attributed to the 3d electrons of titanium atoms adjacent to silicon. Therefore, most electrons in the loop were provided by titanium and silicon easily diffused into the solution during corrosion.

The corrosion/passivation mechanism could be sketched in Fig. 4 that layered crystal structure and weaker chemical bond between Si and Ti–C layer made silicon atoms are more likely diffused outward which promoted the reaction [6].

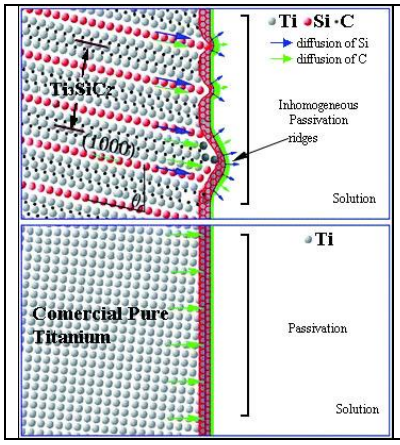

Fig. 4 The Schematic of passivation in 3.5% NaCl solution and the difference, (a) schematic of Ti_3SiC_2, (b) schematic diagram of CP titanium. [6].

Silicon and titanium inhomogeneous diffusion reduced efficiency of passivation films generation and a great deal of silicon and titanium atoms loss into solution and which could be due to the increasing of polarization potential.

On the contrary, titanium atoms in CP Ti diffused uniformly into the barrier layer enhanced the protection of the passivation film as shown in Fig. 4b.

The microstructure of the surface of the material before and after oxidation differs significantly (Fig. 5). Before the tests (Fig. 5(a)), the Mn-Ti matrix phase (Table 2) and the carbide phase

separation (Table 2 phase 1) were observed on the surface of the sample. After testing the sample for electrochemical corrosion, a passivating film appears on the sample surface (Fig. 5b). Such structural changes occurred as a result of partial dissolution of less stable surface layers based on Ti and Si.

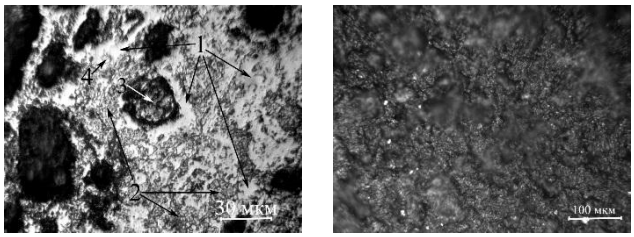

a b

Fig. 5. X-ray microspectral analysis of sintered samples obtained from the $65TiH_2/30FeSiMn/B_4C$ powder mixture: a – sample after synthesis at 1250°C, b – sample after synthesis immersed in a 3% NaCl solution

Table 2: Chemical composition of elements in different phase components of the $65TiH_2/30FeSiMn/B_4C$ composite (%, wt.)

	Fe	Mn	Si	Ti	C/B	Фаза
1	0,36	0,73	0,17	78,96	19,94	TiC
2	7,83	14,74	1,66	69,32	6,44	Mn_xTi_x
3	7,86	24,52	0,39	65,11	2,12	Mn_xTi_x
4	10,68	44,56	2,81	39,01	2,95	Mn_xTi_x

4. Conclusion

The electrochemical corrosion properties in a 3% NaCl solution of a multicomponent composite based on titanium, system 65TiH2–30FeSiMn–B4C, were studied. It was found that after immersing the sample in a 3% NaCl solution, the radiograph shows a decrease in the titanium carbide peaks by half, the titanium silicon carbide almost disappears. Amount of the silicide phase also decreases, which is associated with the dissolution of the Ti and Si phases in the solution.

The corrosion/passivation mechanism of Ti/Si/C compared to commercially pure titanium was elucidated. A high resistance to anodic oxidation was established, which is due to the formation of a protective TiO_2 (rutile) film on the surface of the sample. The conducted research makes it possible to predict the corrosion behavior of new titanium-based composites during their operation in natural environments.

5. References

1. Froes F. H., Eylon D. Powder-Metallurgy of Titanium Alloys // Int. Mater. Rev. – 1990. – Vol., 35, (3). – P. 162–182.

2. Liu Y., Chen L. F., Tang H. P., Liu C. T., Liu B., Huang B. Y. Design of Powder Metallurgy Titanium Alloys and Composites // Materials Science and Engineering. A. – 2006. – Vol. A418, (1–2). P. 25–35.

3. Whittaker D. Powder Processing, Consolidation and Metallurgy of Ttanium // Powder Metallurgy. – 2012. – Vol. 55; No. 1. – P. 6-10.

4. Ivasyshyn O.M., Bagliuk G.A., Stasyuk O.O., Savvakin D.G. The Peculiarities of Structure Formation Upon Sintering of TiH2+TiB2 Powder Blends // Physics and Chemistry of Solid State. - 2017. - Vol. 18, No. 1. - P. 15-20.

5. Bagliuk G.A., Stasyuk A.A., Savvakin D.G. Structure and Phase Composition of Sintered Alloys Obtained From Powder Mixtures of the TiH_2+TiB_2 System // Powder Metallurgy: Surface Engineering, New Powder Materials. Quarrel. - Minsk: "Belarusian Science", 2017. - P. 347-359.

6. Ming Zhu, Rui Wang, Chen Chen, Haibin Zhang and Guojun Zhangc Electrochemical Study on the Corrosion Behavior of Ti_3SiC_2 in 3.5% NaCl Solution // RSC Advances. – 2017. – Vol.7; Iss. 21 – P. 12534-12540.

7. Jovic V. D. Corrosion Behavior and Passive Film Characteristics Formed on Ti, Ti_3SiC_2, and Ti_4AlN_3 in H_2SO_4 and HCl / V. D. Jovic, M. W. Barsoum. // Journal of The Electrochemical Society. – 2004. – Vol.151; No.2. – P. B71–B76.

8. Zhou Y., Sun Z., Chen S. & Zhang Y. (1998). In-situ Hot Pressing/Solid-Liquid Reaction Synthesis of Dense Titanium Silicon Carbide Bulk Ceramics // Materials Research Innovations. – 1998. – Vol. 2; No.3. – P.142–146.

9. Shein A.V., Pavroznyk V.S., Rokytyanskaya I.L. Silicides of Transition Metals - Promising Corrosion-Resistant Electrode Materials // 18th Mendeleev Congress on General and Applied Chemistry. Moscow. – September 23-28, 2007. Abstracts of reports. T. 2. Chemistry of metals, nanostructures and nanotechnology. - M.: Granitsa. - 2007. - P. 616.

10. Boltovets N.S., Ivanov V.N., Konakova R.V. SiC Schottky- Barrier Diodes Formed with TiB(x) and ZrB(x) Amorphous Layers / N.S. Boltovets, V.N Ivanov, R.V. Konakova and all. // Semicond. Phis., Quantum Electron and Optoelectron. – 2004. – 7. 1. – P. 60–62.

11. Danylovich D.P., Kayumov R.A., Mukhamedova I.Z. High-Temperature Properties of Ceramics Based on Titanium Diboride and Silicon and Boron Carbides / D. P. Danylovich, R. A. Kayumov, I. Z. Mukhamedova. // Bulletin of the Kazan Technological University. – 2014. – Vol. 17 No. 9. – P. 28–30.

12. Chirkin A.D., Lavrenko V.A., Talash V.N., Panasyuk A.D. Formation of Oxide Nanofilms on The Surface of Titanium, Molybdenum, and Tungsten Disilicides During Anodic Polarization // Dop. NAS of Ukraine. – 2006. – No. 12. – P. 96–101.

Studying the surface and microstructure of a chromium coating with nanodiamond particles deposited on monolithic composite with layered structure

Vladimir Petkov[1,*], Mihaela Aleksandrova[1], Radoslav Valov[1], Valery Korzhov[2], Vyacheslav Kiiko[2], Tatyana Stroganova[2]
[1] Bulgarian Academy of Sciences, Institute of Metal Science, Equipment and Technologies with Center for Hydro- and Aerodynamics "Acad. A. Balevski", 67 Shipchenski Prohod Blvd, 1574, Sofia, Bulgaria
[2] Institute of Solid State Physics, Russian Academy of Sciences, 2 Akademik Osilyan str., Chernogolovka, Moscow Region, 142432, Russia
vladimir2pe@yahoo.com

Abstract: *Electrochemical coatings of chromium modified with nanodiamond particles applied directly on niobium-aluminum alloy were obtained. Nanodiamond particles produced by detonation synthesis were used. Chromium coatings were deposited on a monolithic composite with a complex structure based on niobium and aluminum alloys, called later matrix for short. Standard chromium electrolyte and electrolyte with nanodiamond particles concentration of 10 g/l were used. Analyzes were performed by Scanning Electron Microscope system of Bruker Inc. and the Polyvar Met metallographic microscope. The microhardness was measured using a PolyvarMet 4000 microhardness tester. The obtained results of the microhardness were 788 kg/mm^2 in the chromium layer and 168 kg/mm^2 and 692 kg/mm^2 in the matrix. The microstructural and SEM-EDS analysis showed the presence of two intermetallides Nb_2Al and Nb_3Al in the monolithic composite of niobium aluminum matrix. The average thickness of the chromium coatings modified with nanodiamond particles is 55 μm.*
Keywords*: CHROMIUM COATING, NANODIAMOND PARTICLES, NIOBIIUM ALUMINUM MATRIX, MICROSTRUCTURE*

1. Introduction

High-temperature monolithic composites with layered structures are usually obtained by pressing at certain temperature of bundled layers of various metal foils and powders such as: Mo-Al, Nb-Al, Nb-Al-Ti, Cr-Al-Nb [1], Mo-Nb-B-Si [2] and others. In our case, we consider a composite of niobium (niobium alloy with 0.1% carbon) and aluminum foils pressed at 1-2 MPa at a temperature of 1300°Cin vacuum.

In the binary system Nb-Al the main phases are: $NbAl_3$, Nb_2Al and Nb_3Al [3]. According to some authors the phases Nb_7Al_3 and $Nb_{17}Al_3$ also coexist [4]. The first attempt to use the batch rolling method to obtain a monolithic composite was made to densify aluminum and niobium foil at a temperature of 300°C[5].

To improve the properties of this type of monolithic composite (MC) such as heat resistance, microhardness, wear resistance, corrosion resistance, they are electrochemically coated with metallic chromium. The composite chromium coatings modified with nanodiamond particles deposited on various metals and alloys such as steel, aluminum, etc. additionally contribute to increasing the above-mentioned properties. [6, 7, 8].

In the present research the main aim was to obtain composite chromium coatings with diamond nanoparticles deposited directly on a monolithic composite based on a niobium aluminum matrix with a layered structure. Their structure and morphology were studied on the one hand, and on the other hand, the thickness of the coating and its microhardness were determined. A uniform and dense layer of chromium with nanodiamonds with thickness of about 55 μm was obtained. The microhardness in the chromium layer is about 800 kg/mm^2, in the matrix close to the chromium layer it is about 170 kg/mm^2 and in the middle of the sample it is about 700 kg/mm^2.

Any application of coatings, regardless of the type of metal matrix, is carried out by preliminary removing of the oxide layer from the metal surface immediately before depositing the coating. In our case, a series of oxide layers of the main elements Nb and Al, from which the monolithic composite was obtained, must be removed. Multicomponent alloys are usually chemically treated with a series of acids and their mixtures and bases also in some cases. Electrochemical polishing in appropriate electrolyte solutions is also used to remove the oxide layers.

2. Experimental data

The objective of the study is to obtain a chromium coating with nanodiamond particles on a monolithic composite with a layered structure obtained on the basis of a niobium alloy with 0.1% carbon and aluminum. The phase composition, microstructure and elemental composition in different areas of the matrix and of the chrome coating were investigated. The primary test samples are rectangular tiles with dimensions - 30 x 20 mm and height h - 1.5 mm. Figure 1 shows some of the chromium-coated test samples shot with an optical microscope (LM). There, the structure of the chromium coating surface was shot with magnification marked A x20 and B x80 with different levels of illumination. The chromium coating follows the surface of the monolithic composite sample with a layered structure that is slightly rough with elongated stripes. The basic chromium coating has a slightly wavy structure with fine grains, which is more clearly observed in (Fig. 1B).

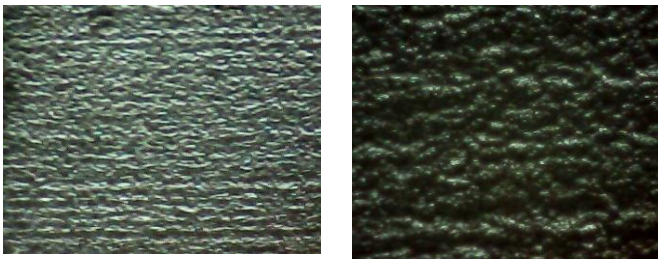

A, x20 *B, x80*

Fig. 1 *Chromium coating with ND deposited on the niobium aluminum matrix with magnification A x20 and B x80*

Short description of the preliminary treatment (technological process) for obtaining chromium coatings with ND on MC of the niobium aluminum matrix (alloy): The samples are first grinded, then degreased and etched with a mixture of acids. The niobium alloys are usually cleaned of the surface oxides with a mixture of the acids HF, HNO_3, H_3PO_4 in a ratio of 1:1:1 or 1:1:2 [9]. Finally they are immersed in a special acid-alkaline solution [10] before connected to the cathode and immersed in the chromium plating electrolyte.

The preliminary chemical treatment is extremely important for obtaining a uniform, dense and well-adhered chromium coating. Otherwise, the coatings crack, peel or do not adhere well to the metal matrix. In the present study a standard chromium plating electrolyte was used with chromic anhydride:sulfuric acid ratio of 100:1 [6, 10]. It has the following chemical composition: CrO_3 – 220 g/l; H_2SO_4 - 2.2 g/l.

The electrochemical parameters of the process are:

Current density: 45 A/dm^2

Duration: approx. 45 min

The electrolyte temperature: approx. 50^{o}C

Two electrolytes are prepared. The first is the standard chromium electrolyte described above and the second one is with the nanodiamond particles. It is in the form of an aqueous suspension with an ND concentration of 10%. The suspension with ND was then activated in an ultrasonic bath, after which the resulting

electrolyte is added to the standard electrolyte for chromium plating with a final concentration of nanodiamonds of 10 g/l. The previously treated niobium aluminum samples connected to the cathode are immersed in the obtained in this way electrolyte and the electrodeposition of metallic chromium is carried out. The final result of the chromium plating of the niobium aluminum matrix is shown in (Fig. 1).

3. Research, results and discussion

3.1. X-ray structural analysis

Investigations were done with a Bruker D8 Advance powder X-ray diffractometer. The Bruker DIFFRAC.EVA program was used to determine the qualitative and quantitative phase analysis.

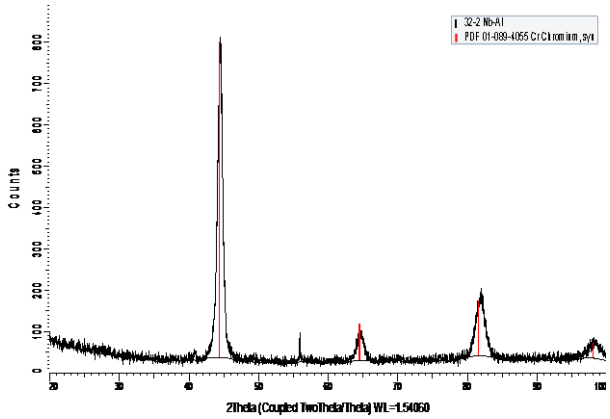

Fig. 2 *Diffractogram of chromium coating with diamond nanoparticles deposited on MC of the niobium aluminum matrix designated as(32-2Nb-Al)*

In the diffractogram in Fig. 2 one phase of metallic chromium with a cubic structure is found, which is evidence of a good density of the chromium coating.

3.2. Microstructure and microhardness

The microstructure of the chromium coating with ND deposited on MC of niobium aluminum alloy was imaged with a "Polyvar Met" metallographic microscope (Fig. 3). The chromium coating was prepared from electrolyte with concentration of nanodiamonds in the electrolyte 10 g/l. The microhardness in the chromium layer was about 800 kg/mm^2, which is typical for chromium coatings with ND. It was determined using a PolyvarMet 4000 microhardness tester (Fig. 3). In the matrix with a layered structure it is 168 kg/mm^2 which we assume was measured in the aluminum and niobium solid solution and it was about 690 kg/mm^2 most likely measured at the obtained intermetallyde Nb_2Al.

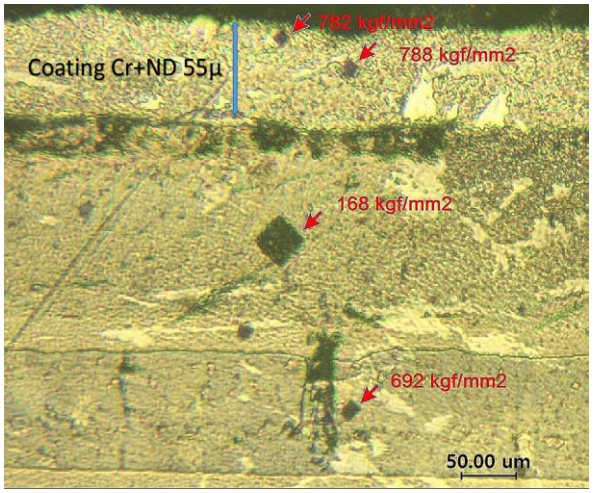

Fig. 3. *Microstructure and microhardness of chromium coating with nanodiamond particles deposited directly on MC of niobium aluminum alloy*

The chromium layer is 55 µm thick, uniform and dense, following the surface of the monolithic composite of the niobium aluminum matrix. (Fig. 3).

3.3. Surface morphology and elemental composition determination

The studies were carried out using a scanning electron microscope "HIROX SH-5500P" with an EDS system "QUANTAX 100 Advanced" with accelerating voltage: from 1 to 30 kV. In Fig. 4 A the chromium coating is observed which is in gray. The coating in Fig. 4 B is in black and its border is hardly distinguishable from the final border with the resin with which the sample is prepared. The SEM examination of the chromium coating deposited on MC of the niobium aluminum matrix is surrounded by a yellow square marked with the number 3.

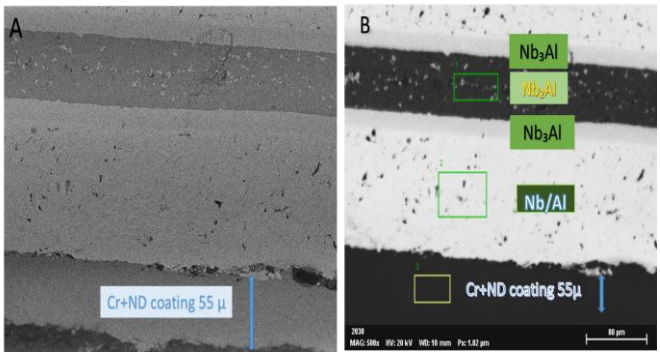

Fig. 4. *SEM image of a chromium coating with nanodiamond particles deposited on a MC of a niobium aluminum matrix*

The surface was investigated at magnification x500 and it consists of continuous and uniform layer of chromium with nanodiamond particles with thickness approximately 55 µm thick.

1

Element	At. No.	Netto	Mass [%]	Mass Norm. [%]	Atom [%]	abs. error [%] (1 sigma)	rel. error [%] (1 sigma)
Nb	41	13931	47.53	50.84	18.28	1.84	3.88
Al	13	17517	33.31	35.62	44.09	1.66	4.98
C	6	311	12.65	13.53	37.63	4.16	32.88
		Sum	**93.49**	**100.00**	**100.00**		

2

Element	At. No.	Netto	Mass [%]	Mass Norm. [%]	Atom [%]	abs. error [%] (1 sigma)	rel. error [%] (1 sigma)
Nb	41	40929	91.38	88.05	49.56	3.42	3.74
C	6	422	11.74	11.32	49.26	3.49	29.69
Si	14	539	0.66	0.63	1.18	0.07	10.82
		Sum	**103.78**	**100.00**	**100.00**		

3

Element	At. No.	Netto	Mass [%]	Mass Norm. [%]	Atom [%]	abs. error [%] (1 sigma)	rel. error [%] (1 sigma)
Cr	24	29844	82.11	94.55	86.40	2.29	2.79
C	6	186	2.52	2.90	11.49	1.02	40.30
Nb	41	457	1.62	1.86	0.95	0.13	8.29
Si	14	244	0.59	0.68	1.16	0.08	13.17
		Sum	**86.84**	**100.00**	**100.00**		

Figure 4 shows the examined in zones and characterized by SEM-EDS analysis of the surface of the chromium coating with ND and of the niobium aluminum matrix. The elemental composition

was determined in three zones: In zone 1 the intermetallyde Nb_2Al was found according to the elemental composition and microstructural analysis from. In zone 2 it was a solid solution of niobium and aluminum in the niobium aluminum matrix. And in zone 3 it was only the chromium layer with diamond nanoparticles.

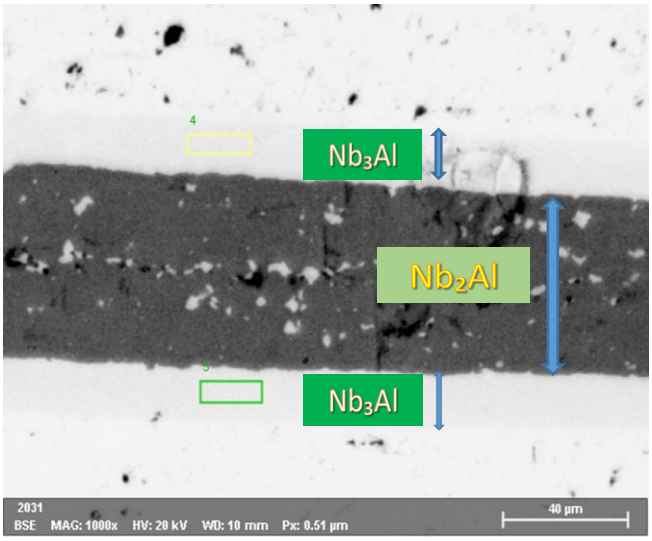

***Fig. 5**. SEM image of zone study of the monolithic composite with a layered structure based on a niobium aluminum matrix*

Figure 5 shows the zone examination and characterization by SEM-EDS analysis of MC of the niobium aluminum matrix. The elemental composition is determined in two zones: 4 and 5, where the intermetallyde Nb_3Al is most likely to be found, and the broad dark band is the intermetallyde Nb_2Al.

The data from the studies in a Nb/Al matrix are shown in the zone marked with 4. The main elements are Nb, Al, C and traces of Si.

4

Element	At. No.	Netto	Mass [%]	Mass Norm. [%]	Atom [%]	abs. error [%] (1 sigma)	rel. error [%] (1 sigma)
Nb	41	13800	78.04	75.19	34.70	3.01	3.86
C	6	195	13.57	13.07	46.67	5.26	38.79
Al	13	2898	11.73	11.31	17.97	0.67	5.71
Si	14	138	0.45	0.43	0.66	0.07	16.59
		Sum	**103.79**	**100.00**	**100.00**		

In zone 5, the yellow rectangle in Fig. 5 the data from the studies inside the matrix are presented, from which it is clearly seen that the quantities of the main elements match and are approximately the same in mass percentages as those of zone 4.

The identified carbon, although with a large error, is very likely to be from the nanodiamonds used in the chromium plating electrolyte (Fig. 4), zone 3 and/or from the carbon content of the niobium alloy used together with aluminum foil to produce a monolithic composite with a layered structure (Fig.5), zone 4 and 5.

5

Element	At. No.	Netto	Mass [%]	Mass Norm. [%]	Atom [%]	abs. error [%] (1 sigma)	rel. error [%] (1 sigma)
Nb	41	56111	82.54	76.26	36.84	3.08	3.73
Al	13	11765	12.86	11.89	19.77	0.66	5.16
C	6	678	12.37	11.43	42.71	3.16	25.57
Si	14	530	0.46	0.43	0.68	0.06	12.47
		Sum	**108.24**	**100.00**	**100.00**		

4. Conclusions:

Electrochemical chromium coatings with ND were deposited directly on a monolithic niobium aluminum matrix composite.

The presence of chromium with a cubic structure in the coating was determined by X-ray structural analysis.

The chromium coatings with ND were found to be dense, discontinuous, following the surface of the monolithic niobium aluminum matrix composite with a layer thickness of about 55 µm.

It was found that the microhardness in the chromium coating is nearly 15 % more than that measured in the Nb_2Al intermetallyde obtained in the niobium aluminum matrix.

The microhardness in the chromium coating was found to be nearly 5 times greater than that measured in the Al/Nb solid solution obtained in the niobium aluminum matrix.

The presence of two intermetallydes Nb_2Al and Nb_3Al was determined by microstructural and SEM-EDS analysis.

SEM-EDS analysis determined the presence of carbon in the samples, most likely from the niobium alloy (Nb01C) in the matrix and traces of carbon in the chromium coating, which are most likely from the diamond nanoparticles which proves their participationin the structure of the layer.

5. Acknowledgments

5.1. This study was performed with the financial support of the Fund "Scientific Researches" (research project No KP-06-Russia/18, date 15.12.2020)

5.2. The work was supported by RFBR grant 50-53-18002

6. References

1. F. Stein, H. Cuiyun, I. Wossack I, J. of Alloys and Comp. **598**, 253–265 (2014)
2. T. Yang, X. Guo, 2019, *Metals*, **9**, 653 (2019)
3. A. da Silvaa, G. Coelhob, C. Nunesb, J. Fiorani, N. David, M. Vilasi, Mat. Res., **22**, 5 (2019)
4. M.J. Richards, Jour. Mét., 1-12, (1962)
5. A. Nishimoto, K. Akamatsu, Mat. Sci. Forum, **634**, 1390 (2010)
6. V. Petkov, R. Valov, S. Simeonova, M. Kandeva, Arch. of Foundry Eng., **20**, 115, (2020)
7. N. Gidikova, M. Sulowski, V. Petkov, R. Valov, G. Cempura, Arch. Metall. Mater, **62,** 2421-2424 (2017)
8. N. Gidikova, A. Cias, V. Petkov, M. Madej, M. Sulowski, R. Valov,. Arch. Metall. Mater, **59**, 1523, (2014)
9. V. Palmieri, F. Stivanello, S.Yu., The 10th Workshop on RF Superconductivity, Tsukuba, Japan, (2001)
10. N. Gidikova N., **V.** Petkov, R. Valov, BG Patent 67042B1, (2020)

Effect of solanine on corrosion of steel 3 in lactic acid

Tamara Pyzhik[1], Tatyana Povshok[1], Valery Sarokin [1], Angel Velikov[2]
Yanka Kupala Grodno State University[1] – Grodno, Belarus, Bulgarian Academy of Sciences, Institute of Metal Science, Equipment and Technologies with Center for Hydro- and Aerodynamics "Acad. A. Balevski",, Bulgaria[2],
E-mail: pyzhik_tn@grsu.by, povshok_to@ grsu.by, sorvg@grsu.by, anmabg@abv.bg

Abstract: *The object of research – the natural glycoalkaloid solanine as a possible inhibitor of acid corrosion of steel St3. Modern data on the structure and physico-chemical properties of solanine, such as amphiphilicity, surface activity, basicity, characteristic of modern organic corrosion inhibitors, are presented. The basic concepts are defined: basic nitrogen, solanine amphiphilicity, mass and volume corrosion indicators, corrosion inhibitor, degree of protection, corrosion inhibition coefficient. The literature data on the corrosive activity of lactic acid (MC) are presented and characterized.*
KEYWORDS*: CORROSION, ST 3, CORROSION INHIBITOR, LACTIC ACID, SOLANINE DEGREE OF PROTECTION, BRAKING COEFFICIENT*

1. Introduction

Structural carbon steel St3 of ordinary quality is a universal alloy used in all areas of industry. Various metal structures are made of it, working under normal conditions. However, in an aggressive environment, this steel needs anti-corrosion protection.

One of the modern strategies aimed at combating corrosion is the search for non-trivial corrosion inhibitors based on the principles of Green Chemistry. The starting material for the production of such substances can be not only affordable and renewable plant raw materials, but also industrial waste of plant and animal origin. Rational use of waste, prevention of its adverse or harmful effects on people and the environment, is the most important concept of modern production.

This is especially important for chemical industries associated with the use of aggressive media, or the production of substances that have high corrosive activity. Such substances include oil, solutions of inorganic acids (sulfuric, hydrochloric, orthophosphoric), some salt solutions and solutions of organic acids (formic, acetic, lactic).

Numerous studies in recent years have mainly focused on the creation of corrosion inhibitors for strongly acidic media, such as solutions of hydrochloric, sulfuric, nitric acids [1]. The effect of organic acids on the corrosion of industrial steel has not been sufficiently studied.

Of undoubted interest is the study of the corrosive activity of lactic acid (MK). This is due to the constantly increasing demand for this product. MK is widely used in the food industry in the production of beverages, flour products, fruit and vegetable processing. The chemical industry uses MK for the production of neutralizers, for the production of optically active substances, complexing agents and cosmetic products. It is also used as an anti-scale agent, as part of solvents and cleaning agents. Large volumes of MC are used for the synthesis of the biodegradable polymer polylactate (PLA) [2].

According to [3], the global production of MK in 2015 amounted to 354 thousand tons. Currently, the global production capacity is 430 thousand tons. According to the results of 2016, the global demand for MK amounted to 1 million 220 thousand tons and should grow by 16.2% by 2025. Today, the following trends are observed in the global lactic acid market:

– growth of production capacities for the production of MK;
– increase in the share of MK use in non-food industries;
-orientation of the largest manufacturers to the output (PLA).

Further development of the PLA market is predicted, an increase in the production of pharmaceuticals, environmentally friendly food products and food additives.

MK is not produced on an industrial scale in the Republic of Belarus. It has to be purchased abroad. Our country's demand for it has reached 600 tons per year.

An essential condition for increasing the efficiency of enterprises for the production and processing of MK is to increase the reliability of equipment. Anticorrosive protection of equipment, ensuring the safety of the stock of metal products are a guarantee of increasing the safety of production.

Currently, there is fragmentary and contradictory information about the rate of corrosion of metals under the influence of MK. According to [4] stainless titanium-containing high-strength austenitic steels of the AISI 304 (V2A) and AISI 316Ti (V4A) grades have "excellent" chemical resistance in MK solutions. Other authors note that MK causes corrosion of steel [5]. Yu.I. Batsko and R.S. Reshetova point to the significant role of MK in the corrosion destruction of equipment of sugar factories [6]. Along with the information that MK causes corrosion of steels only at high concentrations [7], there are statements of the opposite nature [8]

Thus, fragmentary and contradictory information about the rate of corrosion of steel under the influence of MK complicates the problem of finding effective corrosion inhibitors.

The aim of the study was to study the dynamics of corrosion of steel St3 in aqueous solutions of various concentrations of MK under the influence of solanine extract.

2. Materials and methods of research

Lactic acid (2-hydroxypropane) has two optical isomers (D and L). It is most often used as a racemate, an optically inactive mixture consisting of equal amounts of D- and L-enantiomers (Figure 1).

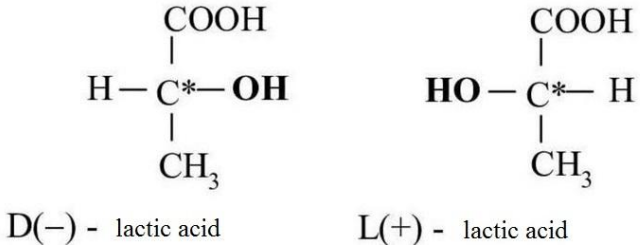

Figure 1 *Lactic acid – D- and L-enantiomers*

MK is a heterofunctional compound that simultaneously possesses the properties of alcohols and carboxylic acids. This largely explains its high reactivity. Intramolecular hydrogen bonds between hydroxyl and carboxyl groups enhance the acidity of lactic acid (pKa 3,8). It is 80 times stronger than acetic acid.

High hygroscopicity and pronounced acidity are extremely important properties for the manifestation of corrosion activity of MK.

Solanine (Figure 2) is a glycoalkaloid from the Solanaceae family, consisting of aglycone and solatriose. Aglicon is represented by the steroid alkaloid solanidine. The presence of a nitrogen atom in the composition of solanidine gives the whole compound the properties of an organic NH-base with high chemical activity. The carbohydrate fragment of the solatriose molecule includes residues of glucose, galactose and rhamnose monosaccharides. The hydrophobic aglycone and hydrophilic carbohydrate component give the compound an amphiphilic character and determine the surface activity of solanine.

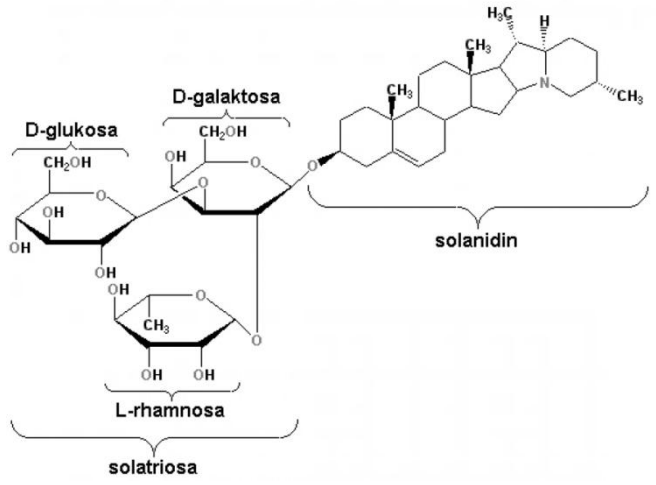

Figure 2 *Chemical structure of corned beef*

Solanine is a natural alkaloid, it is synthesized in all parts of plants of the Solanaceae family. The highest content of solanine is observed in unripe berries of black nightshade (Solanum nigrum). The tubers of ripe potatoes contain a small amount of solanine – about 0.01%. In sprouted, green tubers, the level of solanine increases many times, reaching 0.5%, while especially a lot of solanine appears in potato sprouts and peel [9].

To obtain the solanine extract, potatoes previously aged in sunlight for 30 days were used. A thin layer of peel was removed from the sprouted and green tubers together with the seedlings, crushed and homogenized. Solanine was extracted with a hot ethanol solution acidified with acetic acid. An extract containing a suspension of solanine was used in the experiment.

In laboratory studies, samples of St3 steel weighing 8.07 – 8.23 g, with a diameter of 30 mm were used. A 1M H_2SO_4 solution was used to etch the samples. Then the samples were cleaned with sandpaper, degreased, washed under running water, dried, weighed.

In all variants of the experiments, MK with concentrations of 0.5% (0.055 mol/l); 5% (0.56 mol/l); 50% (6.7 mol/l) were used. The volumes of the reaction mixture with steel samples were adjusted to 80 cm3. The experiments were carried out at a temperature of 200C.

In the first series of experiments, 4 cm^3 solanine extract was added to lactic acid solutions (4 mg in terms of pure substance) (experiment 1). In the second series of experiments, a suspension of solanine was applied directly to heated steel samples and dried. After applying the extract, the samples were covered with a film. Then the samples were placed in lactic acid solutions without adding solanine to them (experiment 2). Control samples were placed in MK solutions with concentrations of 0.5%, 5% and 50%.

Considering that under experimental conditions, electrochemical corrosion of steel St3 proceeds with hydrogen depolarization, the corrosion rate was determined by the volumetric method, fixing the volume of hydrogen released. To do this, the prepared samples were placed in eudiometer flasks, tightly closed and the volumes of hydrogen released were monitored for 24 hours.

The volumetric corrosion index was expressed in cm3/m2h; the mass index was expressed in g/m2h.

To assess the effectiveness of the inhibitor, the degree of protection Z (%) and the inhibition coefficient ɣ (inhibitory effect) were determined according to the formula 1 and 2, respectively:

$$\text{Degree of protection: } Z = (K_1\text{-}K_2) / K_1 100\% \quad (1)$$

$$\text{Inhibitory effect: } \gamma = K_1 / K_2 \quad (2)$$

3. Results and discussion

As can be seen from the presented data (Table 1), in the experimental conditions there was no clear relationship between the concentration of MC and the volume of hydrogen released. Thus, in the region of low concentrations of MK, in the range from 0.5% to 5%, an increase in the volume of hydrogen released by 175% was observed. However, during the transition from a low concentration of 5% to a high concentration of 50%, only a slight (by 14%) increase in the level of hydrogen was recorded. Thus, low concentrations of MK have a more effective effect on the speed of the cathode process than high concentrations.

Table 1: *Volumes of released hydrogen, V(H_2), cm^3*

MK concentration	control	experience 1	experience 2
0,5%	5,2	1,8	1,7
5%	9,1	2,8	2,0
50%	10,4	4,6	5,5

The addition of solanine extract to the reaction mixture led to an effective reduction in hydrogen release at all the studied concentrations of MK – by 2.9, 3.25 and 2.2 times by 0.5%, 5% and 50%, respectively (experiment 1). Identical dynamics of hydrogen release was revealed when solanine was applied directly to the samples (experiment 2), which confirms the effect of inhibition of the corrosion activity of MK by solanine obtained in experiment 1 (Figure 3).

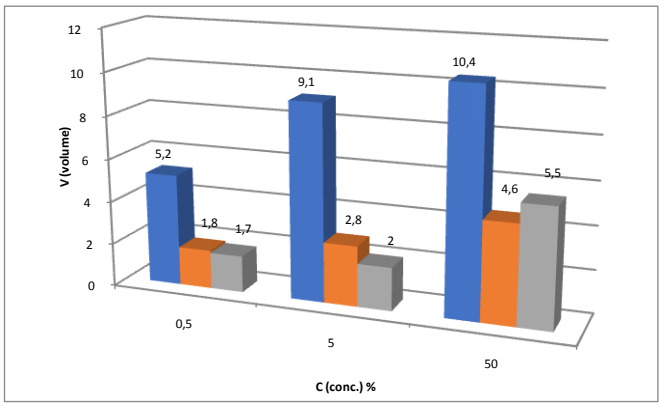

Figure 3 *Volumes of released hydrogen, V(H_2), cm^3*

Data on the corrosion rate obtained by calculating the volume and mass indicators also indicate the activation of the corrosion process with an increase in acid concentration (Table 2). However, this dependence is complex. In the area of low concentrations, with an increase in acid concentration by 10 times (0.5 – 5%), the corrosion rate increased by 175%, but with a subsequent increase in concentration by another 10 times (up to 50%), the corrosion rate increased by only 14%.

Analyzing the results obtained in the context of the corrosive activity of acidic media, we tried to compare the results obtained with data on the corrosion rate of steel St3 in other acids. Comparison of the obtained results with the literature data [10] showed that the mass index of Ct3 corrosion in 0.5% solution of MK (0.38 g/m^2·h) coincides with that for 0.037% HCl (0.37 g/m2·h), and the corrosion rate in 50% solution of MK (0.77 g/m^2·h) is commensurate with corrosion rates of 3.7% HCl (0.72 g/m^2·h) and 0.1% H2SO4 (0.74 g/m^2·h).

It can be reasonably assumed that MK exhibits pronounced corrosion activity and that during the operation of steel St3 in environments where the synthesis of MK (lactic acid fermentation) is possible, or its use as a working medium, corrosion protection of steel equipment is necessary.

Solanine extract, the mass fraction of which in the samples was only about 0.005% (in terms of the target substance), inhibited the corrosion of the samples in all variants of the experiments. Under the influence of the indicated dose of the drug, the corrosion rate in 0.5%, 5%, 50% solutions of MK was 35%, 30%, 44% of the control, respectively (experiment 1). We obtained similar results in experiment 2, where the corrosion rate under the influence of solanine, when applied to a metal surface, was suppressed by 67%, 68% and 47% in 0.5%, 5% and 50% solutions of MK, respectively (Table 2).

Table 2: *The effect of solanine extract on the volume and mass indicators of the corrosion rate of St3 in MK solutions*

MK concentration	Variants of experiments	Volumetric corrosion index $K_V(H_2)$, $cm^3/m^2 \cdot h$	Mass corrosion index K_m, $g/m^2 \cdot h$
0,5%	control	153	0,38
	experience 1	53	0,13
	experience 2	50	0,13
5%	control	268	0,67
	experience 1	82	0,21
	experience 2	58	0,14
50%	control	306	0,77
	experience 1	135	0,34
	experience 2	162	0,40

It is important to note that solanine properties such as basicity and surface activity meet the requirements for modern corrosion inhibitors. The presence of an unshared electron pair on the nitrogen atom and a volumetric hydrocarbon radical in the molecule makes it possible to classify solanine as a mixed-type inhibitor [11]. The probable mechanism of corrosion inhibition revealed in our experiments may include chemisorption of solanine on the surface of steel, followed by blocking the penetration of hydroxonium ions to the metal surface.

Figure 3 shows photographs of St3 steel prototypes in MK solutions with a mass fraction of 50%. A large area of uniform corrosion of control samples under the influence of MK is visually noticeable (Figure 4a) and the absence of traces of corrosion on the test samples (Figure 4b, figure 4c).

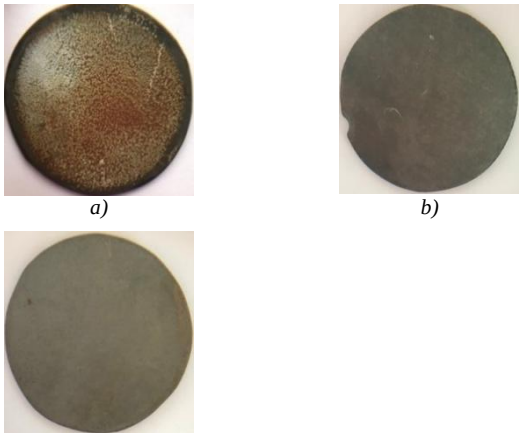

a) *b)* *c)*

a) control sample (50% lactic acid); b) prototype (50% lactic acid + solanine extract); c) prototype (50% lactic acid + solanine layer)

Figure 4 *Control and experimental samples*

The effectiveness of the anticorrosive properties of solanine was evaluated by the degree of protection (Z), as well as by the inhibitory effect (ɣ). Calculations of the values of Z and ɣ showed the greatest effectiveness of solanine in 5% MK when applied directly to the plate. The degree of protection of the St3 samples was 78%, while the corrosion rate decreased by 4.6 times. Significant, though somewhat less significant values of Z and ɣ are shown in the remaining variants of the experiment using solanine extract (Table 3).

Table 3: *Degree of protection and corrosion inhibition coefficient St3 in MK under the influence of solanine extract*

	0.5% lactic acid solution		5% lactic acid solution		50% lactic acid solution	
	Z (%)	ɣ	Z (%)	ɣ	Z (%)	ɣ
experience 1	65	2,9	69	3,3	56	2,3
experience 2	67	3,1	78	4,6	47	1,9

In order to confirm the data obtained indicating the effectiveness of solanine as an inhibitor of acid corrosion St3, we conducted experiments using hydrochloric acid as a corrosive medium. The experimental samples were treated with corned beef extract in the same way as in Experiment 2. The results demonstrated that the inhibitory effect of solanine is also manifested in hydrochloric acid. Exposure of samples in a solution with HCl (0.56 mol/L) for 24 hours resulted in a 2.54-fold decrease in the corrosion rate. Thus, the volumetric corrosion index in the experiment was 486.5 $cm^3/m^2 \cdot h$ versus 1238 $cm^3/m^2 \cdot h$ in the control; the mass index is 1.2 $g/m^2 \cdot h$ and 3.1 $g/m^2 \cdot h$, respectively. The degree of protection (Z) was 61%.

4. Conclusion

The results of the study allow us to speak about the pronounced corrosion activity of MK, on the one hand, and about the protective effect of solanine against acid corrosion of Ct3, on the other.

Maintaining the focus of further research and solving specific issues, such as selecting the optimal concentrations of solanine, determining the duration of its inhibitory effect, etc., can be productive for protecting the working surfaces of machine parts from corrosion. The conducted researches can be useful for machine-building enterprises.

5. References

1. Ivanov, E.S. Metal corrosion inhibitors in acidic media : handbook / E.S. Ivanov. – M.: Metallurgy, 1986. – 175 p.

2. Samuylenko, A.Ya. Trends in the development of lactic acid production / A.Ya. Samuylenko, S.A. Grin [et al.] // Bulletin of Kazan Technological University. – Kazan, 2017. – Vol. 20, No. 1. – P. 162-166.

3. MAS Albion [Electronic resource]. – Access mode: https://albionchem.ru/news/14809 /. – Access date: 09.24.2022.

4. Inoxpark [Electronic resource]. – Access mode: https://www.inoxpark.ru/info/characteristics/. – Access date: 10.09.2022.

5. Metalloy [Electronic resource]. – Access mode: https://metalloy.ru/obrabotka/chistka/metalla-kislotoy – Access date: 03.10.2022.

6. Batsko, Yu.I. The problem of corrosion of sugar factories equipment and ways to solve it / Yu.I. Batsko, R.S. Reshetova // Sugar. – M., 2022. – No. 4. – P. 16–18.

7. All about corrosion [Electronic resource]. – Access mode: https://www.okorrozii.com/korrozia-v-kislotah.html . – Access date: 27.10.2022.

8 Culinary Library [Electronic resource]. – Access mode: http://knigakulinara.rubooks >item. – Access date: 15.10.2022.

9. Orlin N.A., Razumova S.S. Isolation of saponins from the peel of green potatoes // International Journal of Applied and Fundamental Research. – 2011. – No. 6. – P. 154–154.

10.Figiliantov, A.P. Corrosion protection of low-carbon steel in acidic media with inhibitors of the Sonkor A.V. series / A.P. Figiliatnov, A.V. Melnikova, A.B. Shein // Izvestiya vyshchikh uchebnykh zavody. Chemistry and chemical technology. – Ivanovo, 2015. – Vol. 58, No. 11. – P. 61–65.

11. Kozlova, L. S. Corrosion inhibitors (review) /L. S. Kozlova, S. V. Chesnokov, A. E. Kutyrev // Aviation materials and technologies. - 2015. – No. 2. – P. 67–75.

Heat-insulating lightweight concretes and composite materials on the basis of inorganic binders with application in construction

Lyuben Lakov, Bojidar Jivov, Mihaela Aleksandrova, Stancho Yordanov, Krasimira Toncheva

Bulgarian Academy of Sciences, Institute of Metal Science, Equipment and Technologies with Hydro- and Aerodynamics Centre "Acad. Angel Balevski", 67 "Shipchenski prohod" Blvd., 1574 Sofia, Bulgaria,
e-mail: silicatchim@mb.bia-bg.com

Abstract: *A general overview of a number of thermal insulation materials and products made on the basis of inorganic binders (mainly Portland cement) is presented. The technological methods of production, the main operational indicators and the application in construction of various heat-insulating and structural-heat-insulating lightweight concretes are examined. The structure of various cellular concretes (foam concretes and aerated concretes), composite materials and lightweight aggregate concrete was analyzed. The role of the origin, technological processing, characteristics and composition of different types of light additive materials for the formation of the final operational properties of the products has been traced.*
Keywords: *COMPOSITE MATERIALS, INORGANIC BINDERS, LIGHTWEIGHT CONCRETE*

1. Introduction

One of the main priorities in the renovation of the existing building stock (built according to different construction systems) and the construction of new buildings is the provision of optimal energy efficiency [1-5], sound insulation and fire safety.

In modern construction, they find various applications materials with heat and sound insulation characteristics [1-4,6-19]: expanded polystyrene (EPS), extruded polystyrene (XPS), polyurethane, depron, rubber sheets, wood-fiber boards, cork boards, insulation wallpaper, mineral wool (stone, glass, slag), various composite materials and lightweight concretes with various structures and other materials.

The construction of external thermal insulation is a widely applied approach that provides a number of advantages [2,3]: protection of the building from cyclical climatic effects of the environment during the different seasons, lowering the necessary energy consumption to maintain a favorable microclimate and comfortable living environment in the living spaces during the heating period and summer months, preserving the volume of the interior space of the premises (in contrast to interior insulation), soundproofing effect, aesthetic renewal of building facades and others.

The design and construction of thermal insulation systems using some of the materials that have gained considerable popularity in recent decades (EPS, XPS etc.) does not provide an optimal solution in the long term within the entire service life of the building. Significant disadvantages of a large part of the various modifications of the mass-applied products are insufficient reliability in the conditions of fires, aging of the material, limited shelf life and other.

In a number of cases, a more expedient approach is the use of various thermal insulation materials obtained on the basis of inorganic binders [1,9,18-25], providing better complex performance indicators**.** In this aspect, products made of lightweight concretes [6,9,18,19,26-29], which are characterized by a bulk density of up to 1800 kg/m^3, represent a promising possibility. Various types of heat-insulating (compressive strength > 0.5 MPa, thermal conductivity coefficient < 0.3 W/mK), structural-heat-insulating concretes (compressive strength > 3.5 MPa, thermal conductivity coefficient < 0.75 W/mK) have been developed) and structural lightweight concretes (compressive strength > 15 MPa). Typical representatives of lightweight concretes are foam concretes [9,18,26], aerated concretes (made mainly by the autoclave method) and concretes with the presence of a significant amount of lightweight aggregates [6,25,27,28]. The main advantages of the use of lightweight concrete are the lightening of the built structures [19,20], the increase of heat and sound insulation characteristics, the use of long-lasting, non-flammable and non-combustible products (in the absence of organic lightweight aggregates).

The aim of the present overview is the presentation in a summarized form of part of the results of a preliminary study conducted in connection with the implementation of scientific-applied project financed by NIF of BSMEPA. A full opportunity to apply the obtained data is the development, based on the existing experience, of an innovative material that meets the requirements for installation around doors and windows of buildings, according to Ordinance No. I$_3$/1971 of 2009, amended in 2015, concerning construction technical rules and norms for ensuring fire safety.

2. Heat-insulating lightweight concrete and composite materialsbased on hydraulic inorganic binders

2.1. Heat-insulating lightweight concretes with a cellular structure

Foam concrete and aerated concrete refer to cellular concrete [6,24], which are characterized by the presence of pores uniformly distributed in the volume and are prepared from a binder, a quartz component, water, a suitable pore former (foam-forming and gas-forming additives), etc.

The technological methods used to obtain the cellular concretes allow the regulation of porosity and the preparation of products with different volumetric mass, appropriate thermal conductivity, sufficient strength and various purposes [1,29]. The increase in bulk density from 600 to 1200 kg/m^3 is accompanied by an increase in strength and thermal conductivity. There are different brands (15, 25, 35, 50, 75, 100, 150) of cellular concrete determined by compressive strength. Water absorption and frost resistance depend to a significant extent on the distribution, characteristics and stability of the formed porous structure [20].

Cellular concretes are classified into three main groups [6]: heat-insulating (with a volume density of not more than 500 kg/m^3), structural-heat-insulation for enclosing structures (with a volume density of 500 to 900 kg/m^3) and structural applicable to reinforced concrete (with a volume density from 900 to 1200 kg/m^3).

Portland cement is usually used to make cellular cement concrete. Developed cement-free aerated concretes (gas silicate and foam silicate) by using lime-quartz mixtures and applying autoclave hardening.

Foam concrete is obtained by mixing separately prepared cement dough and mechanically resistant foam, previously obtained in the form of an aqueous solution of a foaming agent (rosins, sulfonates, natural proteins, hydrolyzed animal blood). The air bubbles formed in the binding dough form the characteristic "cellular" structure of concrete with air pores evenly distributed throughout the volume [9,18,29]. An essential technological requirement is that the formed foam exhibits resistance in the alkaline environment of the hydrating cement and does not break before the end of the bonding [26]. To increase its stability, stabilizers and mineralizers (iron and aluminum salts or hydrophilic substances such as water glass, glue, gelatin, etc.) are introduced into the aqueous solution of the foaming agent.

With the direct introduction of air-entraining additives into the cement dough, a controlled increase in the presence of a certain amount of air in the form of small bubbles distributed evenly in the

product, which ensures a decrease in thermal conductivity, an increase in volume and a decrease in the mass of the products [1]. This allows the preparation of filled, frost-resistant and other concretes. Acidol, hydrophobic surfactants, abietic acid and others are used as air-entraining agents.

Foam concrete is non-combustible (class A1), an ecological material characterized by the presence of evenly distributed spherical closed pores, less water absorption, high frost resistance, wear ability, low thermal conductivity, good heat and sound insulation properties [9]. The spherical shape of the pores, which is characteristic of foam concrete, provides a more favorable distribution of the forces under load and the same properties in different directions. The volume weight, quantity and size of the formed pores vary widely in the case of foam concretes, providing an appropriate combination of the necessary thermal insulation and strength characteristics, which are consistent with the intended functional use of the product [18]. Foam concrete is used in the construction of partition walls, load-bearing walls (in accordance with its load-bearing capacity), heat and sound insulation of walls and ceilings, floor screeds and others. Significant opportunities are provided by the application of mobile units for the preparation and laying of foam concrete directly on construction sites, which speeds up the execution of construction activities and allows the preparation of concrete masses with the necessary indicators. Foam concrete mixtures are characterized by low density, very good workability, self-leveling and self-compacting properties and the possibility of applied through pumping equipment and installations [9,18]. The material is applicable for monolithic casting in formwork forms, leveling of floor surfaces, as filler (for cavity filling and hard-to-reach areas), etc.

Aerated concrete is cellular concrete prepared by the autoclave method from mixtures of Portland cement, quartz component (fine fraction) and gas-forming additives, forming a characteristic structure with evenly distributed holes in the volume of the finished product [6]. The formation of pores is carried out by the introduction of gas-forming additives, in which gas is released as a result of chemical reactions [1].

According to the type of gas-forming chemical reaction, gas-forming additives are classified into three types [6]:

- entering into a chemical interaction with the binder or the products of its hydration (for example, aluminum powder - most often a degassing agent). The aluminum powder interacts with the calcium hydroxide $Ca(OH)_2$ obtained during the hydration of the cement, during which hydrogen is released. In this interaction, the particles of aluminum powder become the centers of the formation of gas bubbles, which gradually increase and form pores in the cement paste;
- decomposing additives with gas release (perhydrol H_2O_2 when interacting with CaClOCl);
- interacting and releasing gas as a result of exchange reactions - ground limestone and hydrochloric acid.

In the production of aerated concrete, cement, quicklime, gypsum dihydrate, ground quartz sand, aluminum powder and water are used as raw materials [6]. The prepared mixture is sieved and left in a heat tunnel for up to 3 hours at a temperature of 50-60°C. The hardening of aerated concrete blocks takes place in the process of autoclaving at a pressure of 20 Bar and a steam temperature of 180-190°C (with a technological downtime in the autoclave of 10 h).

Among aerated concrete products, the YTONG trademark has gained exceptional popularity. The Autoclaved aerated concrete (AAC) is fire-resistant, non-combustible (class A1), ecological, long-lasting product with low density, good vapor permeability, suitable sound and heat insulation properties. Various construction products are made from the material [1,6]: bricks, blocks, slabs, panels, vaults, roofing and flooring. The appropriate complex operational characteristics of aerated concrete products ensure their wide application in modern construction. The low weight of the products facilitates transport and their application on construction sites. The diverse assortment, the concrete sizes, the easy workability, allow accelerated implementation of the planned construction activities. Foam concrete products are applicable for the construction of external walls, internal partition walls, internal insulation and others. The strength indicators of some products allow their application in the construction of load-bearing structures. The material is resistant to the impact of various weather conditions and their cyclical changes. At the same time, the use of aerated concrete products reduces the risk of condensation and the development of mold and mildew.

2.2. Thermal insulation composite materials and lightweight aggregate concrete

Products obtained on the basis of light additive materials and matrix frominorganic binders**,** are composite materials [30-32]. A variety of heat-insulating composite materials and various lightweight concretes, applicable in modern construction, have been developed [30]. Different fractions lightweight aggregates find application [33-36]: volcanic pumice, volcanic slag, limestone tuff, swollen vermiculite, diatomite, obsidian, perlite, clay mica, slate, ceramsite, fireclay, slag ashes, slag pumice, granulated blast furnace slag (GBFS), clinker, ash from TPS, carbon-containing waste, wood waste, expanded polystyrene granules, etc. According to their origin and degree of technological processing, lightweight aggregates are classified as natural and artificial [33]. Natural lightweight aggregates are obtained by partial crushing and screening of natural porous rocks (volcanic tuff, pumice, shelly limestone, etc.). Artificial lightweight aggregates are products obtained during the heat treatment of various mineral raw materials. With these materials, two groups of lightweight aggregates are distinguished: specially prepared (swollen perlite, vermiculite, clays and mica) and secondary products from industry (ash from TPS, metallurgical slag, etc.).

When developing various composite materials (in particular lightweight concrete), the pre-planned operating characteristics (thermal conductivity, mechanical parameters, manufacturability, processability, cost) determine the selection and use of specific lightweight aggregates materials [33]. For products in which high structural resistance is not required, but the priority characteristic is the presence of thermal insulation properties, it is recommended to apply a highly porous, especially light additive material [1]. At the same time, due to the significantly lower bearing capacity of these composites, their functional application is limited.

The most favorable complex combination of the main indicators (bulk mass, thermal conductivity, strength) of the final products and the negligible consumption of cement for their preparation is achieved with maximum saturation with lightweight aggregates and their compact distribution in the volume [6]. Effective saturation with lightweight aggregates is possible only with appropriate selection of the particle size composition of the introduced small and large fractions and the application of some technological factors (intensive compaction, use of plasticizing additives, etc.). This minimizes the presence of cement stone, which is the heaviest part of the composite [30].

The most important characteristics of lightweight aggregates are their bulk density and compressive strength, which largely determine the performance of the products [33]. Perlite and vermiculite are most often used for the preparation of heat-insulating composite materials. Volcanic tuff is applicable in the production of structural-heat-insulating composites and lightweight concretes with a bulk mass of 1300-1800 kg/m^3 and a strength of 5-20 MPa. Swollen clays and micas (type expanded clay), sintered ash fine gravel and agglomorite are considered suitable lightweight aggregates for the preparation of structural lightweight concrete.

The sizes, the number, the local distribution and the geometric shape of the pores in the grains have a significant influence on the strength indicators of the lightweight aggregates, as the smaller volume of the pores provides higher strength. The reduction of the porosity of the shell of the aggregates allows an increase in the strength [33]. For swollen clays and micas, this is accomplished by applying heat treatment in an appropriate temperature range. The presence of a coated shell of the grains lowers water absorption, while lightweight aggregates are characterized by significantly higher water absorption [1,20,30].

The water absorption of lightweight aggregates with closed pores and an uneven surface depends on the amount of water in the cement paste, the consistency of the cement paste, the presence of plasticizers, the duration of the stay of the grains in the mixture until it is compacted [1,6].

The process of swelling or agglomeration of the raw material (clays, mica, various waste products and others) is a basic technological step in the production of artificial [33]. The swelling of the material during heat treatment to the tempering temperature is carried out under the action of the formed gas phase. To ensure effective swelling [6], the choice of raw materials is consistent with the requirements for the content of gas-forming substances and the simultaneous progress of pyroplastic processes and the release of gases during thermal treatment.

The formation of the gas phase can be the result of various chemical reactions [6]: thermal decomposition and combustion of organic compounds at temperatures above 400°C, separation of water from clay minerals at a temperature of about 600°C, release of CO_2 from carbonates at temperatures of about 900°C, reduction of Fe_2O_3 at a temperature of about 1100°C with release of free oxygen.

After drying, the raw materials (clays, mica, etc.) are crushed and sorted into fractions with a certain maximum size [6]. If necessary, the materials are subjected to additional finer grinding. In the presence of water and special additives, the ground raw material is granulated. Clays with a plastic consistency are molded into cylindrical or other shapes. Swelling processes are mainly carried out in rotary kilns and on sinter conveyors.

The composition of composite materials is determined based on several main factors [33]: set density, influence of the characteristics of the lightweight aggregates on the properties of the final product, water absorption of the porous lightweight aggregates used.

The lightweight aggregates used are usually characterized by lower strength and stiffness than the cement matrix, therefore the maximum achievable strength of the composite is determined by the strength and deformability of the lightweight aggregates [30,33]. The use of very lightweight aggregates is accompanied by increased consumption of cement, and the use of heavy water leads to an increase in density. As the density of the lightweight aggregates increases, the strength indicators of the composite increase.

The granulometric composition of the lightweight aggregates is determined according to the planned strength and density of the composite materials, the necessary compaction of the mixture and the possibility of providing and separately storing different fractions of the lightweight aggregates [33]. The use of lightweight aggregates with a continuous granulometric composition reduces the risk of delamination during the preparation of the products. When preparing heat-insulating and structural-heat-insulating concretes with low bulk density and moderate strength, it is advisable to use lightweight aggregates with a larger share of coarse fractions [6].

The consumption of cement for the preparation of various composites with a given strength varies within wide limits according to the strength of the grains of the lightweight aggregates and the content of free water necessary to compact the resulting mixture [30-33]. The necessary recommended amount of cement is determined with sufficient accuracy experimentally by preparing individual trial mixes with lightweight aggregates with a certain granulometric composition.

An essential characteristic of the materials with the considered structure is the deformation [6] caused by external loads, fluctuations in moisture content and temperature. Deformation under the influence of prolonged static loading in a number of cases reduces the internal stresses in the material (result of shrinkage or temperature fluctuations), which reduces the risk of cracks. But in most cases, this effect is unfavorable, due to an increase in the general deformation of the material.

The preparation of various composites with a porous structure or porous lightweight concrete [6] is carried out from a binder, lightweight aggregates, with or without the introduction of sand, a pore-forming additive, water and in some cases with the introduction of additives regulating the bonding and hardening time. Similar compositions allow reducing the volume density of materials and are used to obtain products containing ceramsite or ceramsite gravel [1,30]. The volume density of the obtained products varies from 700 to 1400 kg/m^3 and depends primarily on the bulk density of the expanded clay lightweight aggregates, the specificity of the pore-forming additive and the presence or absence on sand. In construction practice, various heat-insulating (ceramsite-perlite concrete) and structural-heat-insulating light concretes obtained on the basis of Portland cement and the joint presence of ceramsite and other inorganic porous fillers are used.

A specific technological approach to forming a highly porous construction of the products involves the construction of a fibrous skeleton by introducing and interweaving kaolin, slag, glass, mineral or other fibers [1]. The operational characteristics and density of the resulting products depend on the size and flexibility of the fibers used and their placement in the volume. Air pores of different shapes and sizes are present in the resulting fibrous structure, and with directed orientation of the fibers, samples with higher strength are prepared.

Vermiculite (most often with aggregate size up to 0-6 mm) is used as a thermal insulation lightweight aggregates [1,6]. For the preparation of composite materials based on vermiculite, Portland cement is used, and when preparing different solutions - lime or a combination of cement and lime. Vermiculite concrete is characterized by good thermal insulation properties and at the same time is applicable as a refractory material at temperatures of 900-1100°C.

Swollen perlite (fig. 1) is applicable for the preparation of heat-insulating screeds, various heat-insulating composite materials, etc. paerlite concrete [33]. Due to the low strength of pearlite, the preparation of building structures with pearlite content requires a significant consumption of cement.

Fig. 1. *Perlite for construction (fraction up to 3 mm).*

Agglomerated ash gravel is lightweight aggregates, suitable for the preparation of composite materials and lightweight concrete (with a single-fraction structure or with a continuous granulometric composition) with a relatively low bulk density (1050-1550 kg/m^3) and high strength (5-30 MPa). Grains from agglomerated ash are characterized by a diameter of about 10-40 mm, which is why in some cases crushing is necessary, worsening the surface properties of the lightweight aggregates [34].

For the preparation of various composite products and lightweight concrete (slag pumice concrete and others) slag pumice and granulated blast furnace slag are suitable lightweight aggregates [6,34].

In connection with the growing trend for the utilization of various waste materials, a promising lightweight additive material

with thermal insulation characteristics is the granular foam glass (fig. 2 and 3), obtained after thermal foaming (in the presence of a foaming additive) of waste silicate glass [37,38]. Fractions of foamed glass granules with a fine-grained structure are suitable lightweight aggregates for preparing thin-walled heat-insulating screeds and insulating plasters for walls of different types. A standard application of various fractions of granular foam glass is their use as bulk insulating and filling material. A current opportunity for the use of foam glass granules is their introduction as lightweight aggregates in the preparation of lightweight heat-insulating concrete for construction [39], therefore, they can be considered as a suitable substitute for a number of traditional lightweight additive materials (ceramsite, agloporite, expanded perlite, vermiculite, etc.).

Fig. 2. *Foam silicate specimens obtained from foamed waste glass.*

Fig. 3. *Foam silicate specimen (horizontal and side section).*

Based on foam glass granules, hydraulic inorganic binder (Portland cement) and technological additives, an innovative non-flammable, non-combustible, waterproof and long-lasting composite material was obtained [40-42].

A laboratory technological methodology has been developed for the preparation of various experimental prototypes. The method allows obtaining finished products or blanks subject to additional technological processing. The application of suitable coatings (putty and others) on the external surfaces of the samples increases the operational characteristics of the products [40]. The composite is potentially applicable for the preparation of heat and sound insulation boards and panels, cladding of walls and ceilings, construction of internal non-bearing partition walls, external insulation of buildings, etc. Another possibility of using various composite boards and various profiles is insulation of various production facilities, aggregates, installations and others [39]. The composite material allows further modification and development, according to the planned specific functional role of the products in construction.

3. Conclusions

A significant priority in the reconstruction of old and the construction of new buildings is the provision of optimal energy efficiency, sound insulation and fire safety.

Some of the used standard thermal insulation materials (EPS, XPS, etc.) widely applicable for the construction of thermal insulation systems do not provide a complete solution in a long-term aspect for the entire life cycle of a building.

In a number of cases, the use of materials and products based on hydraulic inorganic binders and other inorganic components is justified. There is a significant variety of heat-insulating and structural-heat-insulating lightweight concretes with a cellular structure (foam concretes and aerated concretes), various composite materials and lightweight concretes obtained on the basis of inorganic lightweight aggregates of various origins, characteristics and fractional composition.

Due to the annually increasing amounts of waste products and existing environmental problems, the development of effective technologies for their utilization is of considerable interest. In this aspect, a promising lightweight additive material with thermal insulation characteristics is granular foam glass obtained after thermal foaming (in the presence of a foaming agent) of waste silicate glass. A full opportunity for the application of different fractions of foam glass granules is their introduction in the role of lightweight aggregates in the preparation of lightweight heat-insulating concretes for construction. On the basis of granular foam glass and inorganic binders (Portland cement), experimental composite materials have been obtained, applicable for the preparation of various insulating boards, profiles and others.

Acknowledgments

The authors express their gratitude to the National Innovation Fund and the Bulgarian Small and Medium Enterprises Promotion Agency at the Ministry of Economy of the Republic of Bulgaria for financing a scientific-applied project / Contract No. 13 ИФ-02-21/12.12.2022 between the contracting authority BSMEPA and contractors - beneficiary "MAG" LTD with partner IMSETHA "Acad. A. Balevski" - BAS.

4. References

1. H. Boydjieva, “Composite materials”, “Nasko-1701”, Sofia, 2000.
2. D. Nazarski, Building Insulations, Publishing House “St. Naum “, Sofia, 2004.
3. R. Savov, D. Nazarski, Energy Efficiency, Thermal insulation systems of buildings, Publishing house “ABC Technic”, Sofia, 2006, (in Bulgarian).
4. L. Aditya, T. M. I. Mahlia, B. Rismanchi, H. M. Ng, M. H. Hasan, H. S. C. Metselaar, Oki Muraza, H. B. Aditiya, “A review on insulation materials for energy conservation in buildings’, Renewable and Sustainable Energy Reviews, Vol. 73, 2017, pp. 1352-1365.

5. Jian-Xin Lu, H. A. Ali, Yi Jiang, X. Guan, P. Shen, P. Chen, Chi Sun Poon, "A novel high-performance lightweight concrete prepared with glass-UHPC and lightweight microspheres: Towards energy conservation in buildings", Composites Part B, 247, 2022, 110295.
6. A. Yoleva, G. Chernev, "Composite materials based on inorganic binders", Guide, UCTM, Sofia, 2009.
7. B. P. Jelle, "Traditional, state-of-the-art and future thermal building insulation materials and solutions - Properties, requirements and possibilities", Energy and Buildings, Vol. 43, Issue 10, 2011, pp. 2549-2563.
8. N. Pargana, M. D. Pinheiro, J. D. Silvestre, J. Brito, "Comparative environmental life cycle assessment of thermal insulation materials of buildings", Energy and Buildings, Vol. 82, 2014, pp. 466-481.
9. Y.H.M. Amran, N. Farzadnia, A.A. Abang Ali, "Properties and applications of foamed concrete: a review", Construct Build Mater, 101 (2015), pp. 990-1005.
10. S. Schiavoni, F. D'Alessandro, F. Bianchi, F. Asdrubali, "Insulation materials for the building sector: A review and comparative analysis", Renewable and Sustainable Energy Reviews, Volume 62, 2016, pp. 988-1011.
11. B. Orlik-Kożdoń, "Assessment of the application efficiency of recycling materials in thermal insulations'', Construction and Building Materials, Vol. 156, 2017, pp. 476-485.
12. P. Mukhtarov, R. Bojilova, "Influence of solar and geomagnetic activity on the ionosphere over Bulgaria", Comptes rendus de l'Acad´emie bulgare des Sciences, 70, 9, 2017, pp. 1289-1296.
13. N. A. Kilifarska, R. Bojilova, "Geomagnetic focusing of cosmic rays in the lower atmosphere - Evidence and mechanism", Comptes Rendus de l'Academie Bulgare des Sciences, 72, 3, 2019, pp. 365–374.
14. R. Bojilova, P. Mukhtarov, "Relationship between the critical frequencies of the ionosphere over Bulgaria and geomagnetic activity", Comptes Rendus de l'Academie Bulgare des Sciences, 73, 8, 2020, pp. 1113–1122.
15. C. Hill, A. Norton, J. Dibdiakova, "A comparison of the environmental impacts of different categories of insulation materials", Energy and Buildings, Vol. 162, 2018, pp. 12-20.
16. G. Mutafchieva, "Technological development of lighting fixtures in the field of silicate design", Collection reports, Design & applied arts - Sofia, NAA, 2018, pp. 138-144.
17. G. Mutafchieva. "Modern trends and development of lighting fixtures in the field of silicate design", PhD thesis for the award of the educational and scientific degree "Doctor", NAA, Bibliography 87, 2020, p. 215.
18. K. C. Thienel, T. Haller, N. Beuntner, "Lightweight Concrete-From Basics to Innovations. Materials", 13, 2020, 1120.
19. K. S. Elango, J. Sanfeer, R. Gopi, A. Shalini, R. Saravanakumar, L. Prabhu, "Properties of light weight concrete -A state of the art review", Mater. Today Proc., 46, 2021, pp. 4059–4062.
20. H. Boydjieva, "Binders technology", "Nasko-1701", Sofia, 2001.
21. P.-C. Aïtcin (Editor), R. J. Flatt (Editor), "Science and Technology of Concrete Admixtures", Book, Publisher: Woodhead Publishing, 1st edition, 2015, p. 666.
22. P.-C. Aïtcin, S. Mindess, "Sustainability of Concrete (Modern Concrete Technology)", Book, Publisher: CRC Press; 1st edition, 2017, p. 302.
23. M. L. Gambhir, "Concrete Technology: Theory and Practice", Book, Publisher: McGraw Hill Education; 2017. p. 792.
24. I. R. Upasiri, K. M. C. Konthesingha, K. Poologanathan, S. M. A. Nanayakkara, B. Nagaratnam, "Review on Fire Performance of Cellular Lightweight Concrete", Lect. Notes Civ. Eng. 44, 2020, pp. 470–478.
25. I. Farina, I. Moccia, C. Salzano, N. Singh, P. Sadrolodabaee, F. Colangelo, "Compressive and Thermal Properties of Non-Structural Lightweight Concrete Containing Industrial Byproduct Aggregates", Materials, 15, 2022, 4029.
26. S. S. Sahu, I. S. R. Gandhi, "Studies of influence of characteristics of surfactants and foam on foam concrete behavior", J. Build. Eng., 40, 2021, 102333.
27. T.S. Al-Attar, K. Heiza, F. Eid, T. Masoud, M. A. Al-Neami, W. S. AbdulSahib, "Lightweight self-compacting concrete with light expanded clay aggregate (LECA)," MATEC Web of Conferences, vol. 162, 2018, p. 02031.
28. A. Pujianto, H. Prayuda, "Fresh and hardened properties of lightweight concrete made with pumice as coarse aggregate", Geomate Journal, vol. 21, Issue 87, 2021 pp. 110-117.
29. B. A. Otakulov, D. T. Sobirova, M. T. Yokubova, "Raw materials and optimal compositions for new generation cellular concrete", Sci. Prog., 2, 2021, pp. 473–475.
30. H. Boydjieva, "Composite silicate materials", MNP, Sofia, 1989.
31. A. L. Brooks, H. Zhou, D. Hanna,"Comparative study of the mechanical and thermal properties of lightweight cementitious composites", Construct Build Mater, 159, 2018, pp. 316-328.
32. L. Wei, W. Zuo, H. Pan, K. Lyu, W. Zhang, W. She, "Rational design of lightweight cementitious composites with reinforced mechanical property and thermal insulation: particle packing, hot pressing method, and microstructural mechanisms", Compos B Eng, 226, 2021, Article 109333.
33. S. Chandra, L. Berntsson, "Lightweight Aggregate Concrete", eBook ISBN: 9780815518204, 1st edition, 2002.
34. V. W. Y. Tam, M. Soomro, A. C. J. Evangelista, "A review of recycled aggregate in concrete applications (2000–2017)", Constr. Build. Mater., 172, 2018, pp. 272–292.
35. Y. Yang, B. Chen, W. Zeng, Y. Li, Q. Chen, W. Guo, H. Wang, Y. Chen, "Utilization of Completely Recycled Fine Aggregate for Preparation of Lightweight Concrete Partition Panels", Int. J. Concr. Struct. Mater. 2021, 15, pp. 1–11.
36. M. M. Abdelfattah, R. Geber, I. Kocserha, "Enhancing the properties of lightweight aggregates using volcanic rock additive materials", Journal of Building Engineering, Volume 63, Part A, 2023, 105426.
37. L. Lakov, K. Toncheva, A. Staneva, T. Simeonova, Z. Ilcheva, "Composition, synthesis and properties of insulation foam glass obtained from packing glass waste", Journal University of Chemical Technology and Metallurgy 48, 2, 2013, pp. 125–129.
38. M. Marinov, L. Lakov, K. Toncheva, "Granulated foam glass. Production. Physical and mechanical characteristics", Proceedings of the XIII Scientific congress on machines, technologies and materials 2016, 14-17 September, 2016, Varna, Bulgaria, Part II, 2016, pp. 56-58.
39. L. Lakov, B. Jivov, Y. Ivanova, S. Yordanov, K. Toncheva, "Alternative possibilities for application of foamed silicate materials", International Scientific Journal "Machines. Technologies. Materials" Issue 1/2021, pp. 25-27.
40. L. Lakov, B. Jivov, M. Aleksandrova, Y. Ivanova, K. Toncheva, "An innovative composite material based on sintered glass foam granules", Journal of Chemical Technology and Metallurgy, 53, 6, 2018, pp. 1081-1086.
41. Y. Ivanova, T. Partalin, L. Lakov, B. Jivov, "Airborne sound insulation of new composite wall structures", MATEC Web of Conferences 145, 2018, 05013, NCTAM.
42. L. Lakov, B. Jivov, Y. Ivanova, S. Yordanov, M. Marinov, S. Rafailov, "Composite Materials Obtained from Foamed Silicate Products", International Journal "NDT Days", Volume II, Issue 2, Year 2019, pp. 188-194.

Noise loading in beehives made out of different materials

Todorka Lepkova, Lyuben Lakov
Bulgarian Academy of Sciences, Institute of Metal Science, Equipment and Technologies with Hydro- and Aerodynamics Centre „Acad. A. Balevski”, 67 "Shipchenski Prohod" Blvd, 1574 Sofia, Bulgaria
e-mail: d_ora@abv.bg

Abstract: *Bees are highly sensitive to noise pollution and in some cases, noise can impact their behaviour. Towards the goal to create optimal living conditions for the bees, we aim to understand how the material of the beehive impacts the microclimate of the beehive. The present paper aims to examine and compare the noise levels inside beehives of the same construction but made out of different materials. Three 10-frame Dadan-Blatt beehives were used in the experiment – a ceramic beehive made out of high-cavity ceramic tiles of marl clay; a ceramic beehive made out of high-cavity ceramic tiles with increased kaolin content and a wooden beehive (pine). The noise was measured in an urbanized area and inside the beehives. The results show that the best performance in terms of noise insulation is the ceramic beehive with increased kaolin content.*
Keywords: *CERAMIC BEEHIVE, NOISE POLLUTION, BEES, BEEHIVE MICROCLIMATE*

1. Introduction

Noise pollution or unwanted noise is the excessive sound that has bad effects on human health, wildlife and environmental quality. Noise pollution is mostly caused by the sound from highways, railways, airplanes, and any transportation traffic, from construction activities and industrial sites [1]. Noise pollution affects the health and wellbeing of many animals including bees.

It is known that bees are using for communication vibroacoustic signals produced by stridulation, gross body movements, wing movements, high-frequency muscle contractions without wing movements, and scraping mandibles or tapping body parts on resonant substrates [2]. For them, airborne sound and vibration signals have a great biological significance [3]. But when honey bees are subject to pure tones at frequencies from 100 to 1500 Hz audible at distance 250 m, the normal activities inside the beehive stop and the insects stop[4, 5]. Another study of the reaction of the honeybees inside the beehive confirms this statement showing that in the presence of sound with a frequency of 100 cy/sec (120 db) to 2000 cy/sec (128 db), it is observed a considerable effect expressed in total cessation on the movements of the workers and drones which even allowed the experimenters to open the beehive and take out a frame without using any smoke [6].

Some specialists argue that noise pollution is considerably affecting the wellbeing of bees creating a great amount of stress which is leading to increased mortality. Another effect on their behavior is the inclination to leave the beehive when exposed to increased stress factors like noise.

The data from the noise level measurements over the last 10 years show that the regulated permissible noise levels have been exceeded in 72% of the examined checkpoints in Bulgaria [7]. The relative share of points with exceeded levels has not changed since 2013, and the indicated results in the last measurements of 2019 and 2020 show a relative increase in noise levels above 61dB. A threshold value of 50 dB is taken as the norm. In most of the control points, the measured equivalent noise levels exceed the limit values with no tendency for improvement.

Increasing noise pollution is threatening the wellbeing of one of the most important pollinators in nature and it is necessary to start studying opportunities to improve their living conditions. Of course, it is hard to influence the environment outside the hive but it might be possible to influence the conditions inside it. One possible way to do so is through technical improvements or even through change in the construction material of the hive. Traditional beekeeping is connected with wooden hives and sometimes plastic or Styrofoam. Recently, a new type of beehive has been introduced to the beekeepers – a ceramic beehive made out of ceramic tiles with increased cavity. One of the advantages of such hives is the better insulation properties [8].

2. Aim

The aim of the present study is to examine and compare the noise levels inside beehives of the same construction but made out of different materials in order to make conclusions about the comfort of the bees which each of them can provide in terms of noise insulation.

3. Methods

The examination has been conducted in the urbanized area of the industrial region of the city of Debeletz, Veliko Tarnovo District, Bulgaria. The evaluation has been performed during daytime (between 10:00 a.m. and 6:00 p.m.) for the period of 31 days, from 01.05.2022 to 31.05.2022. Noise levels have been evaluated by high-sensitivity super-cardioid condenser microphone brand BOYA type BY-MM1+ with the following characteristics:

Table 1. *Technical characteristics of the used microphone*

Converter	Electric capacitor
Polar diagram	Supercardioid
Frequency response	20 Hz-18kHz
Sensitivity	-36 dB +/- 3dB (0 dB = 1V/Pa, 1kHz)
Ratio Signal/ Noise	78 dB
Input plug	3,5mm TRRS line-out/ line output 3,5 мм TRS headphone output
Size	Φ26x100mm (Φ1x3.9”)
Weight	60 gr. (2.1oz)

The beehives which were used for the experiment have the same construction, type 10-frames Dadan-Blatt, but the material of the walls is different, respectively from a ceramic beehive made out of high-cavity ceramic tiles of marl clay; a ceramic beehive made out of high-cavity ceramic tiles with increased kaolin content and a wooden beehive (pine). The beehives were not inhabited.

Fig.1. *From left to right: A ceramic beehive made out of high-cavity ceramic tiles of marl clay; a wooden beehive (pine); a ceramic beehive made out of high-cavity ceramic tiles with increased kaolin content*

Table 2. *Coding*

Beehive	**Description**
Beehive 1	A ceramic beehive made out of high-cavity ceramic tiles of marl clay
Beehive 2	a wooden beehive (pine)
Beehive 3	a ceramic beehive made out of high-cavity ceramic tiles with increased kaolin content

All beehives have a removable drawer-type bottom, which is tightly closed.

The microphone was installed in the beehives and there were measured average values for noise inside the hive. Levels of the environment were also measured.

Fig. 2. *Installation of the microphone inside the beehive*

The output is visualised in figure 3.

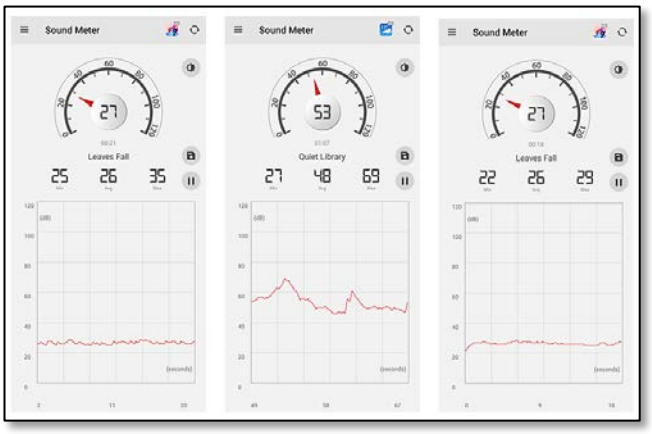

Fig. 3. *Display of the results from the noise measurement, respectively for a ceramic beehive made out of high-cavity ceramic tiles of marl clay; a wooden beehive (pine); a ceramic beehive made out of high-cavity ceramic tiles with increased kaolin content*

The obtained results for the 31-days period were statistically analysed using software IBM SPSS Statistics Software 2019.

4. RESULTS

According to Annex No. 2 of Ordinance No. 6 of June 26, 2006 [9], the maximum value of noise allowed in the urbanized area is 55 db(A) during daytime while in industrial regions, it is 70 db(A). During the time of the experiment, the noise in the area was evaluated to be between min = 32 to max = 61 db(A) with average value of 46 db(A) which is within the permitted levels for the area. Although the area is industrial, in the perimeter of 1 kilometer, there are 3 bee farms and the region is typical for beekeeping which makes the results from the present study relevant and applicable for the apiculture sector.

The following graph presents the evaluated levels of noise for the period. What we observe is that for the whole period of thirty-one days, the ceramic beehive with increased kaolin content (Beehive 3) is showing the best performance in terms of noise insulation.

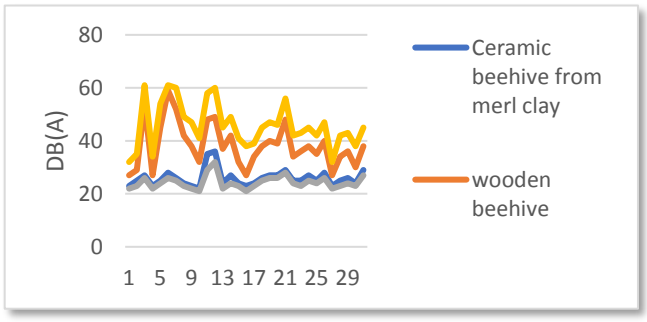

Fig. 4. *Evaluated level of noise*

The graph shows that the values of the ceramic beehive from merl clay (Beehive 1) and the ceramic beehive with increased kaolin content (Beehive 3) are close. In order to understand if the identified difference is significant or not we perform non-parametric statistical test - Related-Samples Friedman's Two-Way Analysis of Variance by Ranks. The results for the pairwise comparisons are presented on table 3.

Table 3. Pairwise comparison

Sample 1 – Sample 2	Test Statistic	Std. Error	Std. Test Statistic	Sig.	Adj. Sig.[a]
Beehive 3 – Beehive 1	1,000	,254	3,937	,000	,000
Beehive 3 – Beehive 2	2,000	,254	7,874	,000	,000
Beehive 1 – Beehive 2	-1,000	,254	-3,937	,000	,000
Each row tests the null hypothesis that the Sample 1 and Sample 2 distributions are the same. Asymptotic significances (2-sided tests) are displayed. The significance level is ,05.					
Significance values have been adjusted by the Bonferroni correction for multiple tests.					

What we see is that the difference of the levels of noise between the three beehives is statistically significant ($\alpha = 0.00 < 0.05$).

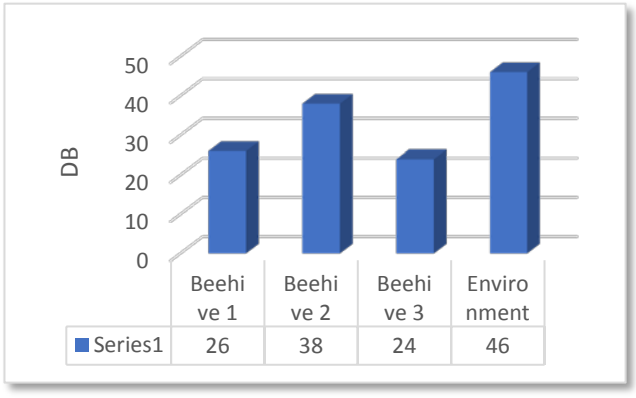

Fig.5. *Levels of noise, average values for the period*

The results displayed of figure 5 are average values for the indicated days in dB, and the graph clearly shows the relative ability to reflect and absorb noise of the different materials. The coefficient ratio $\alpha_n = Rw_n/Rw_o$, where Rw_n is the index of sound insulation from airborne noise inside hive in the range of 100-3150 Hz, where n = 1, 2, 3 is the number of the studied models, and Rw_o is the evaluated average noise in an urbanized environment.

$\alpha_1 = 26/46 = 0.5652$

$\alpha_2 = 38/46 = 0.82$

$\alpha_3 = 24/46 = 0.5217$

What we see is that in terms of noise insulation, the ceramic beehive with increased kaolin content has the best performance followed by the ceramic beehive made out of merl clay - $\alpha 3 < \alpha 1 < \alpha 2$.

5. Conclusio

With the high pace of industrial development, increased connectivity and transportation opportunities, and constantly growing number of people, we manage to create a lot of noise. Although in most parts of the world the noise level is regulated by law, we still manage to disturb the life and the regular habitat of many living creatures. The present study, discusses the importance of the level of noise for one of the most valuable insects - the honey bees. High levels of noise cause total cessation of the moves and there is no data about the influence of a constant exposure of lower noise. It is already a problem for the humanity the ability to provide them optimal living conditions and prevent loss and mortality and while it is hard to influence the environment, improving the living conditions inside the beehive is a much easier task. New approaches with construction and materials seem to give a solution. We can conclude that in terms of noise insulation, the ceramic beehives perform considerably better than the classical wooden one. This gives us the reason to think that such beehives will allow much less disturbance and respectively less stress of the bees in the hive.

6. References

[1] Noise pollution | Definition, Examples, Effects, Control, & Facts | Britannica. (n.d.). Retrieved February 12, 2023, from https://www.britannica.com/science/noise-pollution.

[2] Hunt, J. H., & Richard, F.-J. (2013). Intracolony vibroacoustic communication in social insects. Insectes Sociaux, 60(4), 403–417. https://doi.org/10.1007/s00040-013-0311-9.

[3] Kirchner, W. H. (1993). Acoustical communication in honeybees. Apidologie, 24(3), 297–307. https://doi.org/10.1051/apido:19930309.

[4] HANSSON, Å. (1945). In Lauterzeugung und Lautauffassung der Bienen/ Sound production and conception of sound among bees (Vol. 06).

[5] Michelsen, A., Kirchner, W. H., & Lindauer, M. (1986). Sound and vibrational signals in the dance language of the honeybee, Apis mellifera. Behavioral Ecology and Sociobiology, 18(3), 207–212. https://doi.org/10.1007/BF00290824

[6] Frings, H., & Little, F. (1957).Reactions of Honey Bees in the Hive to Simple Sounds. Science, 125(3238), 122–122.https://doi.org/10.1126/science.125.3238.122.

[7] ИАОС. (2014). Национален доклад за състоянието и опазването на околната среда в РБългария, Шумово замърсяване—ИАОС. Изпълнителна Агенция По Околна Среда. https://eea.government.bg/bg/soer/2014/noise/index.

[8] Lepkova,T., Martinova,I., Martinova,G., Marinova,I., & Pincheva,B. (2019). Ceramic Beehive—A Conceptual Paper. IV(2), 52–54.

[9] REGULATION No. 6 of 26.06.2006 on the environmental noise indicators, taking into account the degree of discomfort during different parts of the day, the limit values of the environmental noise indicators, the methods for evaluating the values of the noise indicators and the harmful effects of noise on the health of the population, Ministry of Healts, Republic of Bulgaria,6(2006),https://eea.government.bg/bg/legislation/noise/nar6.pdf.

Complex electrical impedance and dielectric spectroscopy studies of $BaTiO_3$-$BaSnO_3$ ceramics obtained via sol-gel method.

Mihaela Aleksandrova[1] , Lyuben Lakov[1], Yordan Marinov[2], Vladimir Petkov[1], Bojidar Jivov[1], Geordi Hadjichristov[2]

[1]Bulgarian Academy of Sciences, Institute of Metal Science, Equipment and Technologies with Hydro- and Aerodynamics Centre "Acad. A. Balevski", Shipchenski Prohod Blvd. 67, 1574 Sofia, Bulgaria, e-mail: mihaela.krasimirova@mail.bg

[2]Bulgarian Academy of Sciences, Institute of Solid State Physics "G. Nadjakov", 72 Tzarigradsko Chaussee, Blvd., 1784 Sofia, BULGARIA

***Abstract**: In view of the practical applications of the piezoelectric ceramics produced from barium titanate ($BaTiO_3$) and barium stannate ($BaSnO_3$), (the BT-BS system), the dielectric behavior of such materials was studied. The starting components (powder of both $BaTiO_3$ and $BaSnO_3$) were synthesizedand structurally characterized in advance. Bulk samples of BT-BS (formed as tablets with addition of PVA plasticizer) were prepared using the sol-gel method by varying the BT-BS composition percentage. The samples were characterized by complex electrical impedance spectroscopy and dielectric spectroscopy in the frequency range from 0.1 Hz to 1 MHz. As compared to $BaTiO_3$, an increase with at least 50 % was measured for the value of the room-temperature dielectric constant (ε′ – the real part of the dielectric permittivity) of the BT-BS samples containing 15 wt% $BaSnO_3$. In contrast, the 50 wt% content of $BaSnO_3$ led to a decrease of ε′ value of BT-BS by a factor of 3.5, due to relatively low ε′ value of $BaSnO_3$. Analyses of the frequency spectra of complex electrical impedance and complex dielectric permittivity revealed the dielectric relaxational behavior of the $BaTiO_3$+$BaSnO_3$ system. The results obtained for ε′ of BT-BS dielectrics as a function of the temperature were correlated with the data from structural studies. In particular, a specific enhancement of ε′ was observed in temperature range around 120℃ for the BT-BS samples containing 15 wt% $BaSnO_3$. Corresponding conclusions were done. The effects observed show that the synthesized $BaTiO_3$-$BaSnO_3$ ceramics are promising materials for piezoelectric and dielectric applications, e.g., in energy storage devices.*

***Keywords:** SOL-GEL, $BATIO_3$, $BASNO_3$, IMPEDANCE SPECTROSCOPY*

I. Introduction

Alkaline earth mites are interesting compounds in terms of their dielectric properties. Solid solutions in the $BaTiO_3$-$BaSnO_3$ (BTBS) system have attracted attention in recent years in the field of nanocapacitors. Synthetic $BaTiO_3$, prepared by conventional solid phase method shows great performance with high εr value of ~ 1900 at room temperature (30°C), low dielectric loss δ ~ 0,01 and piezoelectric constant d_{33}~191 pC/N [1]. $BaTiO_3$ has five polymorphic structures showing different phases that vary with temperature [2]. The phase transition of $BaTiO_3$ at the Curie temperature (Tc) significantly changes its properties, which are ferroelectric and non-ferroelectric.

The $BaTiO_3$ nepheroelectric shows a hexagonal structure at 1460°C and a cubic structure at over 120°C [3]. On the other hand, the ferroelectric properties of $BaTiO_3$ exist in three different polymorphic crystal structures, which are tetragonal, orthorhombic and rhombohedral. Zheng et al. [4] studied the effect of grain size on the dielectric constant and piezoelectric properties of $BaTiO_3$. They report that the dielectric constant and piezoelectric properties increase significantly by reducing the grain size. The maximum grain size was reached around 0.94 μm due to the density of the domain structure and the area decreased with decreasing grain size. $BaSnO_3$ has a cubic perovskite structure that exhibits n-type semiconductor behavior at room temperature [5, 6]. $BaSnO_3$ is thermally stable up to 2000°C, but has a high absorption of moisture compared to other species [6]. Thus, it is currently used for thermally stable capacitors and humidity sensors [7, 8]. Meanwhile, completely dense $BaSnO_3$ ceramics can be achieved by synthesizing them at temperatures above 1594°C [6]. Huang reported that in order to obtain single-phase $BaSnO_3$, it is necessary to heat it to 1200°C and achieve a significant amount of grain porosity [9, 10].

In addition, Azad confirmed that grain porosity can be reduced by milling $BaSnO_3$ at 1600°C [11]. The initial report on materials based on the findings found that $BaSnO_3$, synthesized at 1200°C, has a dielectric constant εr~ 14 at 25°C [6]. Kumar reported that $BaSnO_3$ was sintered at 1200°C for 12 hours using the solid state method. A huge dielectric behavior of $BaSnO_3$ has recently emerged, where the dielectric constant εr value reaches ~ 6000 when measured at 220°C and at a frequency of 1 kHz. The ε_r value of $BaSnO_3$ is two orders of magnitude higher than previously reported studies [12, 13]. However, the dielectric constantεr decreases with decreasing temperature. Therefore, it is assumed that the lack of oxygen leads to a reduction of Sn^{4+} to Sn^{2+} in $BaSnO_3$ samples, which contributes to an anomaly in the value of the giant dielectric constant ε_r when the samples were sintered at very high temperatures of $T^oC \geq 1450°C$ [13-16].

II. Experimental part

Organic precursors such as barium acetate, titanium butoxide and stannous acetate were used to synthesize the ceramic samples. The process is carried out according to the sol-gel method, with the ratio of the starting components being 1:1:1.6. The solutions were prepared in the presence of acetic acid, distilled water and acetylacetone. Each of the indicated solutions was homogenized independently using a magnetic stirrer for 30 minutes. After mixing the components, the total solution was homogenized for 5 hours. The synthesis and stabilization of the sol thus carried out allows the deposition of thin layers on various monolithic substrates. One part is allowed to gel. The gel was dried in an oven at 120°C for 24 hours. Next is annealing at 800°C and holding for 8 hours. After obtaining the desired $BaTiO_3$ and $BaSnO_3$ phases, tablets are formed and pressed in the presence of polyvinyl alcohol. The finished samples are calcined in a furnace at a temperature of 1100°C until the plasticizer burns out. The deposition of layers by the immersion method is carried out by means of a dip-coater

III. Results and discussion

Characterization of the resulting phases was performed by X-ray analysis using a Bruker D8 Advance automatic powder X-ray diffractometer with CuKα radiation (Ni filter) and registration by a LynxEye solid-state detector. The X-ray spectrum was recorded in the angular range from 10 to 80° 2θ with a step of 0.02° 2θ and a counting time of 17.5 s/step. Qualitative phase analysis was performed using the International Center for Diffraction Data (ICDD) PDF-2(2022) database. In fig. 1 and 2 are presented X-ray photographs of the prepared samples of $BaTiO_3$-$BaSnO_3$ in the ratio (85%:15%) and $BaTiO_3$-$BaSnO_3$ in the ratio (50%:50%). Figure 2 shows the distinct peaks of the $BaTiO_3$ and $BaSnO_3$ phases. We

have the presence of TiO_2 in two nonstoichiometric compositions between 24° and 25° and nonstoichiometric SnO_2 at 27°. The result may be due to the not good homogeneity during the preparation of the tableted samples or incorrectly conducted temperature mode of baking. When adjusting the percentage ratio of the $BaTiO_3$-$BaSnO_3$ system (85%:15%), we have a monophase characteristic of the $BaTiO_3$-$BaSnO_3$ structure.

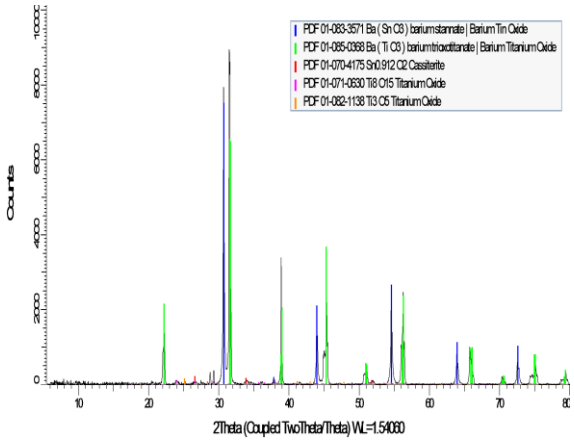

***Fig. 1**. System $BaTiO_3$ + $BaSnO_3$ in ratio (50% : 50%) ceramic*

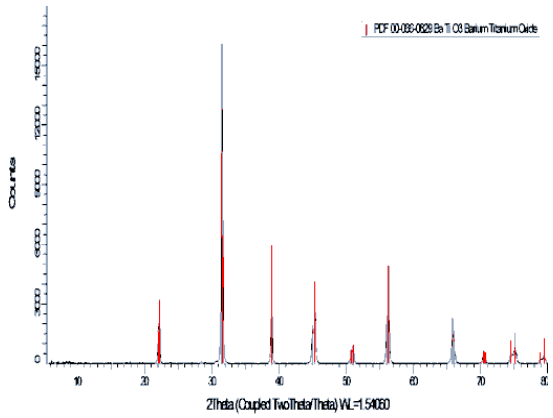

***Fig. 2**. System $BaTiO_3$ + $BaSnO_3$ in ratio (85% : 15%) ceramic*

Description of impedance spectra

Experimental data were obtained by EIS. By this technique, both real (*ReZ*) and imaginary (*ImZ*) parts of the complex electrical impedance $Z^* = ReZ + i\ ImZ$ are simultaneously measured as a function of the frequency *f* of the alternating-current (AC) electric field applied. The frequency spectra of *Z** of the produced sample were recorded by electrical impedance-meter Bio-Logic SP–200, in the range 0.1 Hz – 1 MHz, at various temperatures (Fig.4). By the measurements, forall the samples were kept identical experimental conditions. Silver paste was applied on both sample surfaces, surving as electrodes. The amplitude of the AC voltage applied between the electrodes of ceramic cylinders was 2 V_{RMS} (sine function). The dimensions of the two round electrodes were 2.0 cm in diameter, the distance between them variey 1-4 mm.

Dielectric Spectroscopic Analysis

Dielectric Permittivity

By means of the expressions

$$\varepsilon'(f) = \frac{-Z''(f)d}{2\pi f\ \varepsilon_0\ A\ |Z(f)|^2} \text{ and } \varepsilon''(f) = \frac{Z'(f)d}{2\pi f\ \varepsilon_0\ A\ |Z(f)|^2}$$

from the measured Z′ (f) and Z″ (f) spectra, we calculated the real (ε′) and imaginary (ε″) parts of the complex dielectric function of the composites under study. The geometrical parameters were A = XX cm^2 and d = XX mm, and $\varepsilon_o = 8.85 \times 10^{-12}$ $F.m^{-1}$ was the value of the permittivity of free space. The dispersion curves for both ε′ and ε″ had relaxational characteristics.

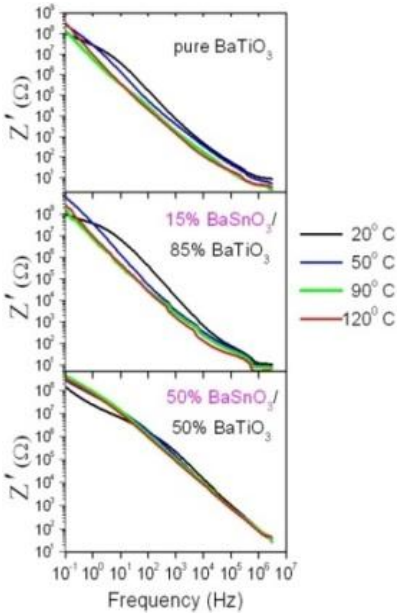

a)

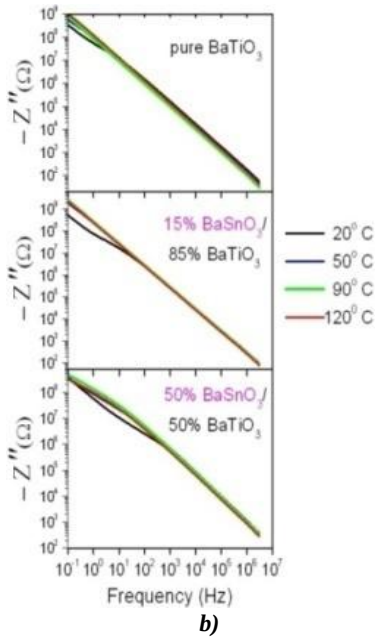

b)

***Fig**. 4 Frequency spectra of real (Z') and imaginary (Z") parts of complex electrical impedance measured for the samples at different temperatures*

Conclusion:

$BaTiO_3$-$BaSnO_3$ ceramic phases were synthesized. XRD analysis showed a good phase structure in the ratio of 85%/ 15%. The studied physical and mathematical indicators showed good piezoelectric effects. With a view to future applications in electronics, the material will be further investigated both as dip-coating deposited thin layers and presented in subsequent developments by the team.

Acknowledgements

The authors are grateful to the financial support of the Bulgarian National Science Fund at the Ministry of Education and Science, Contract No KP-06-Russian/18 от 15.12.2020 for the opportunity to carry out the necessary research.

Part of the team are grateful to the financial support of Bulgarian National Science Fund at the Ministry of Education and Science, Contract No КП-06-Н 37/26 18.12.2019 for the opportunity to present the results at an international conference.

References:

1. Eric A. Gabilondo, Shaun O'Donnell, Rachel Broughton, Jacob L. Jones, Paul A. Maggard," Synthesis and stability of Sn (II)-containing perovskites: (Ba,SnII)HfIVO$_3$ versus (Ba,SnII)SnIVO$_3$", Journal of Solid State Chemistry, (2021), 302.

2. Amine Bendahhou, Pascal Marchet, Soufian El Barkany, Mohamed Abou-Salama, "Structural and impedance spectroscopic study of Zn-substituted $Ba_5CaTi_2Nb_8O_{30}$ tetragonal tungsten bronze ceramics", Journal of Alloys and Compounds, Elsevier, 2021, 882, pp.160-716.

3. Jinyu Lu, Gang He 1, Jin Yan, Zhenxiang Dai , Ganhong Zheng 1, Shanshan Jiang, Lesheng Qiao, Qian Gao, Zebo Fang, "Interface Optimization and Transport Modulation of Sm_2O_3/InP Metal Oxide Semiconductor Capacitors with Atomic Layer Deposition-Derived Laminated Interlayer", Journal Nanomaterials, 2021, 11, 3443.

4. Fayaz Hussain, Amir Khesro, Raz Muhammad, Dawei Wang, "Effect of Ta-doping on functional properties of $K_{0.51}Na_{0.49}NbO_3$ ", 2019, Materials Research Express 6, 106309.

5. Kezhen Yin, Jingwei Zhang, Zhenpeng Li, Jingxing Feng, Ci Zhang, Xinyue Chen, Andrew Olah, Donald E. Schuele, Lei Zhu , Eric Baer, "Polymer multilayer films for high temperature capacitor application", Journal of applied polymer science, 2018, DOI: 10.1002/app.47535.

6. Dong, N., Gao, X., Xia, F., Liu, H., Hao, H. & Zhang, S. (2019). Dielectric and Piezoelectric Properties of Textured Lead-Free $Na_{0.5}Bi_{0.5}TiO_3$-Based Ceramics. Crystals, 9 (4), 9040206-1-9040206-11.

7. L. Zhang, Y. Pu, M. Chen, Ultra-high energy storage performance under low electric fields in $Na_{0.5}Bi_{0.5}TiO_3$-based relaxor ferroelectrics for pulse capacitor applications, Ceram. Int. 46 (2020) 98–105. https://doi.org/10.1016/j.ceramint.2019.08.238.

8. Hend Kacem, Ah. Dhahri, Mohamed Amara Gdaiem, Z. Sassi, L. Seveyrat, L. Lebrun, V. Perrin, J. Dhahri, "Electrocaloric properties of lead-free ferroelectric ceramic near room temperature", Applied Physics A (2021) pp127:483.

9. Dash Smaranika, Pradhan Dhiren K., Kumari Shalini, Ravikant None, Rahaman Md. Mijanur, Cazorla C., Brajesh Kumar, Kumar Ashok, Thomas Reji, Rack Philip D., Pradhan Dillip K., "Enhanced ferroelectric and piezoelectric properties of BCT-BZT at the morphotropic phase boundary driven by the coexistence of phases with different symmetries", (2021) Physical Review B, Volume: 104; Journal Issue: 22.

10. Luo Huajie, Qi He, Sun Shengdong, Wang Lu, Ren Yang, Liu Hui, Deng Shiqing Chen Jun, Structural origin for the high piezoelectric performance of $(Na_{0.5}Bi_{0.5})TiO_3$-$BaTiO_3$-$BiAlO_3$ lead-free ceramics, Journal Acta Materialia Volume: 218, (2021) doi.org/10.1016/j.actamat.2021.117202.

11. F Medjaldi, A Bouabellou, Y Bouachiba, A Taabouche, K Bouatia and H Serrar, "Study of TiO_2, SnO_2 and nanocomposites TiO_2:SnO_2 thin films prepared by sol-gel method: Successful elaboration of variable– refractive index system", Mater. Res. Express 7 (2020) 016439.

12. B. Wodecka-Du´s, M. Adamczyk-Habrajska, T. Goryczka, D. Bochenek, "Chemical and Physical Properties of the BLT4 Ultra Capacitor—A Suitable Material for Ultracapacitors", Materials 2020, 13, 659; doi: 10.3390 /ma13030659.

13. Tae Yeon Kim, Je Oh Choi, Gopinathan Anoop, Jaegyu Kim, Seong Min Park, Shibnath Samanta, Wooseon Choi, Young-Min Kim, Seungbum Hong , Ji Young Jo, "(111)-oriented Sn-doped $BaTiO_3$ epitaxial thin films for ultrahigh energy density capacitors", Ceramics International, Available online 15 June 2021, 0272-8842.

14. Lyuben Lakov, Mihaela Aleksandrova, Vladimir Blaskov, Yordan Marinov, Veselin Petkov, „Technological regulation for creating a ceramic target from $BaTiO_3$ gel powders doped with Sn. Temperature dependence of the dielectric permittivity", Machines. Technologies. Materials. Vol. 15 (2021), Issue 4, pg(s) 155-157.

15. Mihaela Aleksandrova, Bojidar Jivov, Lyuben Lakov, „Summary of sol-gel synthesis of materials with electronic applications", International Scientific Journal Materials Science. Non-Equilibrium Phase Transformations, Year VI, Issue 3 / 2020, Scienticic Technical Union of Mechanical Engineering INDUSTRY 4.0, 2020, ISSN:ISSN PRINT 2367-749X, ISSN WEB 2534-8477, 83-85.

16. Ku Noor Dhaniah Ku Muhsen, Rozana Aina Maulat Osman, Mohd Sobri Idris, "The efects of Ca, Zr and Sn substitutions into a ternary system of $BaTiO_3$–$BaSnO_3$–$BaZrO_3$ towards its dielectric and piezoelectric properties": a review, Journal of Materials Science: Materials in Electronics, Published online, june 2020.

Self-cleaning coatings of oxides transition elements (including - TiO_2) on a photovoltaic covering glass

Stancho Yordanov, Mihaela Aleksandrova, Vladimir Petkov, Marieta Gacheva, Bojidar Jivov, Lyuben Lakov
Bulgarian Academy of Sciences, Institute of Metal Science, Equipment and Technologies with Hydro- and Aerodynamics Centre "Acad. Angel Balevski", 67 "Shipchenski prohod" Blvd., 1574 Sofia, Bulgaria,
e-mail: stancho14@abv.bg

Abstract: *The aim of this paper is to review the cleaning of solar photovoltaic (PV) systems and applied coatings that eliminates costly automated cleaning systems by using nano-sized TiO_2 combined with various organic binders.*
Keywords*: PHOTOVOLTAIC SYSTEMS, SOLAR ENERGY, SURFACE CLEANING, TIO_2, HYDROPHOBIC, HYDROPHILIC.*

1. Introduction:

Solar radiation is the sum of the electromagnetic and corpuscular radiation of the Sun, which is the main source of energy and daylight for the Earth. It propagates in the form of electromagnetic waves at the speed of light and reaches the earth's surface through the atmosphere. The sun's rays pass through it to reach the surface, and it partially reflects, scatters and changes their quantity and quality. Less than two billionths of solar radiation reaches the Earth, but it is the main source of energy for all physico-chemical processes occurring on the Earth's surface and in the atmosphere. There are different forms of light - direct sunlight when the sky is clear and diffused light when the sky is cloudy

Photovoltaic power generation is a technology for generating renewable energy from solar radiation. A photovoltaic (PV) solar cell is a device used to convert solar radiation into electrical energy using semiconductor materials. There are many types of photovoltaic (PV) solar cells, such as - polycrystalline silicon, monocrystalline silicon, thin film and amorphous [1].

Solar energy production from photovoltaic (PV), concentrated photovoltaic (CPV), and concentrated solar (CSP) systems has grown steadily in recent years due to the ever-increasing demand for energy, as well as environmental and economic concerns related to fossil fuel consumption.

The average amount of solar energy falling in one year on one square meter of horizontal earth surface, expressed in kWh/m^2, defines the theoretical resource of solar energy. The average annual duration of sunshine for Bulgaria is about 2150 h, and the average annual solar radiation resource is 1,517 kWh/m^2 [2].

Cleaning the surface of photovoltaic systems is a worldwide problem.

A comprehensive review of the dust problem on photovoltaic systems is given. There are expensive automated cleaning systems that have emerged in recent years, such as electrical, mechanical, chemical, and electrostatic. [3].

Self-cleaning materials have unique properties due to their practical applications in the field of energy and the environment /4/. The self-cleaning coatings that are applied to glass (a major part of solar panels) are divided into two categories: hydrophobic and hydrophilic. Both saw coatings are self-cleaning through the action of water. The first (hydrophobic) is cleaned by the rolling droplets, and the second (hydrophilic) by flowing water that washes away the dirt.

The key difference between hydrophobic and hydrophilic molecules is that hydrophobic molecules are non-polar while hydrophilic molecules are polar. Water is a well-known solvent for dissolving most of the compounds. There are compounds in nature that do not mix with water. Substances that can mix with water are called hydrophilic substances; substances that cannot mix with water are known hydrophobic substances. This is mainly due to the polarity of the water molecules. Non-polar compounds cannot be dissolved in a polar solvent. Polar compounds can dissolve in polar solvents. Nonpolar compounds dissolve in nonpolar solvents. Therefore, hydrophilic substances must be polar to dissolve in water

Photocatalytic TiO_2/SiO_2 coatings with excellent superhydrophilic wettability were investigated on lightweight polycarbonate substrates for self-cleaning applications [6].

Regardless of whether the surfaces are hydrophilic or hydrophobic, they characterize the molecular-scale self-cleaning mechanism of TiO_2 coatings.

Self-cleaning glass uses an organic process where dirt is broken down by daylight and then washed away by rain.

Hydrophilic coatings, which are based on titanium dioxide, have an additional property: they react with sunlight and thus help the chemical breakdown of accumulated dirt. This is a process known as photocatalysis.

Research is focused on hydrophobic and hydrophilic coatings. There are also disadvantages that prevent the mass use of these coatings. Hydrophobic material processing is an expensive and time-consuming technique, and the coatings produced are usually unclear, which precludes their applications in coatings on glass substrates. Self-cleaning coatings based on hydrophilic coatings that rely not only on the flow of water to wash away dirt, but also on sunlight, as the coating breaks down organic dirt while reducing the adhesion of inorganic dirt (Fig. 1, 2).

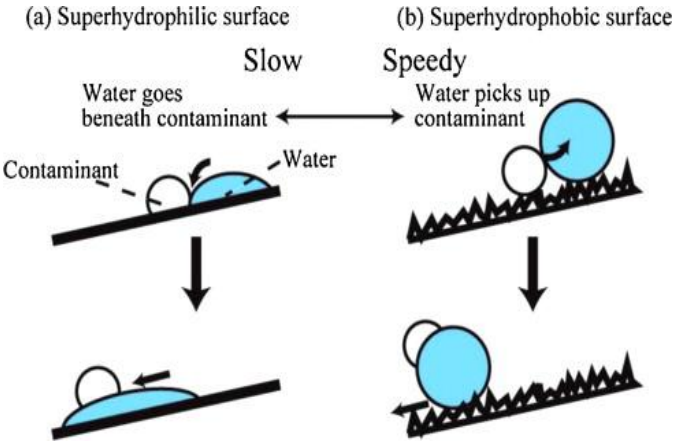

Fig. 1*. Schematic representation of self-cleaning processes on (a) superhydrophilic and (b) superhydrophobic surfaces.*

Table 1. *Contact angle and wettability*

Contact angle:	**Wettability:**
$\theta > 90°$	Hydrophobic
$\theta > 150°$	Superhydrophobic
$0° < \theta < 90°$	Hydrophilic
$\theta < 10°$	Superhydrophilic

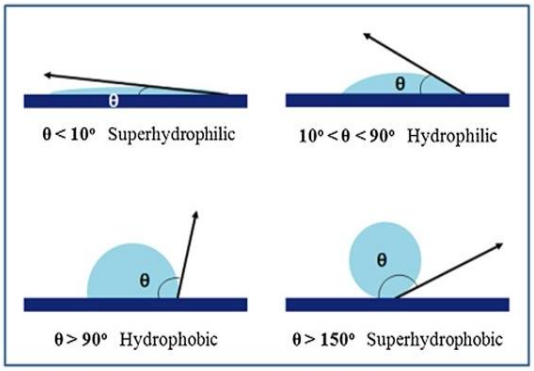

Fig. 2. *Schematic representation of a drop of liquid in equilibrium on a hydrophilic and hydrophobic surface.*

Research is focused on the participation of TiO_2 - as the main component in self-cleaning coatings.

Titanium dioxide TiO_2 is a versatile transition metal oxide that has a large number of applications such as protective coatings, photodetector, optical thin films, microelectronic devices, self-cleaning surfaces, and photocatalyst for the degradation of organic pollutants in wastewater. All these applications are a translation of their attractive properties such as high transmission in the visible region, wide band gap for the anatase phase (3.4 eV) and high photocatalytic activity under ultraviolet light [5].

Adsorption of hydrophobic molecules explains the self-cleaning properties of titanium dioxide. The possibility of aqueous photolysis has been investigated and a useful method developed. Water is transparent to visible light, it cannot decompose directly, but only by radiation with a wavelength shorter than 190 nm.

2. Experiment:

Many variants of coatings involving TiO_2, different types of solvents and silane derivatives have been investigated.

Glass substrates were cleaned in acetone to avoid any organic contamination and then washed with ethanol and water. Double distilled water was used for all experiments. Precursor materials such as $Ti(OCH(CH_3)_2)_4$ and silane derivatives were used for the synthesis of the coating layers. Isopropanol, ethanol and water function as solvents. Acetic acid is used as a chelating agent.

The goal of the research is to obtain self-cleaning glass intended for photovoltaics, construction, automotive and other fields. Applying a few nm thick titanium oxide coating to the outside of the glass creates two mechanisms by which the glass self-cleans. The first is the photocatalytic effect, where ultraviolet rays catalyze the breakdown of organic compounds on the surface. The second is the hydrophilizing effect, in which water forms a thin layer washing away the destroyed organic compounds.

3. Conclusions:

In conclusion, there should be continued research interest in the development of self-cleaning TiO_2-based materials to make the research a reality.

Acknowledgements:

The authors are grateful to the financial support of Bulgarian National Science Fund at the Ministry of Education and Science, Contract № КП-06-Н 37/26 18.12.2019.

4. References:

1. Arash Sayyah, Mark N. Horenstein, M.K. Mazumder Mitigation of soiling losses in concentrating solar collectors, (2013), IEEE 39th Photovoltaic Specialists Conference (PVSC), DOI: 10.1109/PVSC.2013.6744194;
2. Stefka Nedelcheva, Vesselin Chobanov, Solar Energy Audit For A Hybrid System, Magazine "Computer Sciences and Communications", (2013), T2, № 4 Technical University of Sofia;
3. Patil P.A., Bagi J.S., Wagh M. M A Review on Cleaning Mechanism of Solar Photovoltaic Panel, (2017), International Conference on Energy, Communication, Data Analytics and Soft Computing (ICECDS-2017);
4. Swagata Banerjee, Dionysios D. Dionysiou, Suresh C. Pillai, Review - Self-cleaning applications of TiO_2 by photo-induced hydrophilicity and photocatalysis, Applied Catalysis B: Environmental, (2015), Vol. 176–177, P 396-428;
5. Elhachmi Guettaf Temam, Faiçal Djani, Rahmane saâd, Photocatalytic activity of Al/Ni-doped TiO_2 films synthesized by sol-gel method: Effect of sunlight photocatalysis on the catalysts properties, Surfaces and Interfaces**,** 2022, Vol. 31, , 102077;
6. Takahiro Adachi, Sanjay S. Latthe, Suresh W. Gosavi, Nitish Roy and all., Photocatalytic, superhydrophilic, self-cleaning TiO_2 coating on cheap, light-weight, flexible polycarbonate substrates, Applied Surface Science, 2018, 458, 917-923.

Electrospun nano- and microfibrous materials based on cellulose acetate and water-soluble polymer loaded with 8-hydroxyquinoline derivative

Mariya Spasova[1*], Nikoleta Stoyanova[1], Milena Ignatova[1], Nevena Manolova[1], Iliya Rashkov[1], Nadya Markova[2]
[1]Laboratory of Bioactive Polymers, Institute of Polymers, Bulgarian Academy of Sciences,
Acad. G. Bonchev St, bl. 103A, BG-1113 Sofia, Bulgaria
[2]Institute of Microbiology, Bulgarian Academy of Sciences, Acad. G. Bonchev St, bl. 26, BG-1113 Sofia, Bulgaria
[*]E-mail: mgspasova@yahoo.com

***Abstract**: Nano- and microfibrous materials based on cellulose derivative - cellulose acetate and a water-soluble polymer loaded with 8-hydroxyquinoline derivative have been successfully prepared by applying one-pot electrospinning and electrospinning in conjunction with electrospraying techniques. The morphology and the physico-chemical properties of the obtained electrospun materials were studied. The water contact angle of the fibrous mats was determined as well. The incorporation of the water-soluble polymer in the fibers facilitated their wetting and the drug release. Moreover, the antibacterial and antifungal activities of the obtained materials were studied. The obtained results reveal that the created novel fibrous materials can be suitable candidates for wound dressing applications.*

***Acknowledgments**: Financial support from Bulgarian National Science Fund (Grant KP-06-N39/13/2019) is gratefully acknowledged.*

Preparation and characterization of cellulose acetate fibrous materials decorated with nanoparticles

Nasko Nachev*, Mariya Spasova, Nikoleta Stoyanova, Milena Ignatova, Nevena Manolova, Iliya Rashkov
Laboratory of Bioactive Polymers, Institute of Polymers, Bulgarian Academy of Sciences,
Acad. G. Bonchev St, bl. 103A, BG-1113 Sofia, Bulgaria
[a]E-mail: nachev_n@yahoo.com

***Abstract**: Cellulose acetate (CA) is derived from biorenewable resources and can be easily fabricated into diverse forms. Moreover, it is a biodegradable and recyclable polymer with low cost and good physico-mechanical and barrier properties. 8-Hydroxyquinoline and its derivatives manifest antibacterial, antifungal, as well as anticancer activities and are of low toxicity to humans. They are suitable for application to the treatment of infections, cancer, tuberculosis, and other diseases.*

Cellulose acetate - based fibrous materials decorated with nano- and microparticles loaded with 8-hydroxyquinoline derivative were obtained using electrospinning and electrospraying techniques. The morphology of the obtained novel materials was observed by scanning electron microscopy (SEM). The average fiber and particle diameters were determined. Electrospinning of cellulose acetate solutions resulted in preparation of defect-free fibers with mean fiber diameter of 800 nm. The decoration of fibers with the nanoparticles led to hydrophilization of the surface of the fibrous materials and facilitated the release of the incorporated drug. Thus the obtained fibrous materials decorated with nanoparticles loaded with 8-hydroxyquinoline derivative are suitable candidates as antibacterial wound dressing materials, as well as for application in local cancer treatment.

***Acknowledgments:** Financial support from Bulgarian National Science Fund (Grant KP-06-N39/13/2019) is gratefully acknowledged.*

Preparation and anticancer activity of electrospun materials from polylactide and Schiff base derivative of chitosan and 8-hydroxyquinoline-2-carboxaldehyde and their Cu^{2+} and Fe^{3+} complexes

Nikoleta Stoyanova[1,a], Ina Anastasova[1], Milena Ignatova[1], Nevena Manolova[1], Iliya Rashkov[1], Ani Georgieva [2], Reneta Toshkova[2]
[1]Laboratory of Bioactive Polymers, Institute of Polymers, Bulgarian Academy of Sciences,
Acad. G. Bonchev St, Bl. 103A, BG-1113 Sofia, Bulgaria
[2]Institute of Experimental Morphology, Pathology and Anthropology with Museum, Bulgarian Academy of Sciences,
Acad. G. Bonchev St, bl. 25, BG-1113 Sofia, Bulgaria
[a]E-mail: stoyanova_nikoleta@yahoo.com

***Abstract**: Novel fibrous materials were successfully prepared from polylactide (PLA) and Schiff base derivative of chitosan and 8-hydroxyquinoline-2-carboxaldehyde (Ch-8Q) by electrospinning of their blend solution in trifluoroacetic acid. Complexes between the mats and Cu^{2+} and Fe^{3+} ions were obtained. Scanning electron microscopy (SEM), attenuated total reflection Fourier transform infrared spectroscopy (ATR-FTIR) and X-ray photoelectron spectroscopy (XPS) were utilized to study the morphology of the novel materials and their surface chemical composition. In vitro cytotoxicity assay demonstrated that Ch-8Q-containing mats and their complexes displayed high inhibitory activity against human cervical HeLa cells and human breast MCF-7 cells. As evidenced by the performed fluorescence microscopy analyses the anticancer activity of the obtained materials was mainly due to induction of apoptosis. The Ch-8Q/PLA mats possessed no cytotoxicity against non-cancer BALB/c 3T3 mouse fibroblasts. The prepared fibrous materials are promising for use in local treatment of cervical and breast cancer.*

***Acknowledgments:** Financial support from Bulgarian National Science Fund (Grant KP-06-N39/13/2019) is gratefully acknowledged.*